Analysis of liquid-liquid phase separation in *Plasmodium falciparum*

Department of Global Health

Supervisor : TOKUMASU Fuyuki

Applicant : ISHII Ryuta

School of Tropical Medicine and Global Health

Nagasaki University

2024

Abstract of dissertation

Malaria, one of the three major infectious diseases caused by *Plasmodium* parasites, is responsible for 249 million cases and 608 thousand deaths in 2022. Artemisinin-based combination therapy is widely used to treat malaria; however, emerging drug resistance is an urgent problem. Next-generation antimalarials with a novel mechanism of action are desired to address this issue. Liquid-liquid phase separation (LLPS), a recently recognized physical phenomenon regulating several cellular processes, has the potential to provide new insights into parasite biology and a key to drug discoveries toward eradicating malaria.

LLPS is a thermodynamically driven, reversible process that forms two distinct liquid phases from a uniform liquid phase. In many cases, the scaffolds of liquid condensates formed through LLPS are nucleic acids and intrinsically disordered proteins that partly lack a rigid three-dimensional structure. LLPS in cells is driven by the multivalent interactions of biomolecules rather than hydrophobic interactions that facilitate aggregations, and this characteristic allows quick and flexible formation of liquid condensates and immediate cellular response to several events, such as stress or changes in circumstances. Recent studies showed that LLPS in cells had the ability to regulate essential cellular processes such as gene regulation, signal transduction, and immune response. Some diseases, such as cancer, neurodegenerative diseases, and infectious diseases, are deeply related to the LLPS of certain disordered proteins.

This study aimed to clarify the function of LLPS in *Plasmodium falciparum (Pf)* and revealed that many highly disordered *Pf* proteins were classified as nucleotide-binding proteins, consistent with the results of other organisms. Glycolytic body (G-body) is a biomolecular

condensate formed through LLPS of RNA-binding glycolytic enzymes, and I found that G-body-like structures containing phosphofructokinase 9 (PFK9) and phosphoglycerate kinase (PGK) were formed in the parasite cells at low glucose conditions. Metabolome and transcriptome analyses were performed for the G-body-induced *Pf* parasite, and it was clarified that glycolysis activity was maintained without upregulations of these enzymes, suggesting that G-body-like structure formation itself had important functions in overcoming the stress. These structures appeared to be stable, but further microscopic observations and autocorrelation analysis of high signal-to-noise ratio images suggested that they formed transiently first and gradually grew in the cytosol. These results suggested that clustering of glycolytic enzymes formed at low glucose conditions, which may be essential for adapting blood sugar level oscillation in the host and maintaining the parasite's lifecycle.

Table of contents

Acknowledgements

I would like to express my deepest gratitude to my supervisor, Professor Fuyuki Tokumasu, for his unwavering support, invaluable guidance, and scholarly insights throughout my doctoral research. His encouragement, patience, and expertise have been instrumental in shaping this thesis and my academic journey.

I would like to acknowledge the collaborative efforts of Dr. Takaya Sakura for generating transgenic parasites and validation data in Figure 3.4. I would also like to express my gratitude to Dr. Eizo Takashima and Professor Takafumi Tsuboi for providing the antibodies used in Figure 3.4. Their expertise was instrumental in achieving the research goals outlined in this thesis.

I am deeply grateful to Dr. Daniel Ken Inaoka, whose advice, discussions, and shared experiences have been a constant source of inspiration and motivation.

I extend my heartfelt appreciation to the World-leading Innovative and Smart Education (WISE) program, whose financial support enabled me to pursue this research. Their funding was crucial in facilitating data collection, travel for conferences, and access to essential resources for my study.

Special thanks go to Yumika and my family for their unconditional love, encouragement, and understanding throughout this demanding journey. Their unwavering support sustained me through the challenges and highs of doctoral study.

Abbreviations

ABS	Asexual blood stage
ACT	Artemisinin-based combination therapy
ALS	Amyotrophic lateral sclerosis
AMP	Adenosine monophosphate
AMPK	AMP-activated protein kinase
ATP	Adenosine triphosphate
AP2	Apetela2
BRD4	bromodomain containing 4
BSD	blasticidin S deaminase
cGAS	cyclic GMP–AMP synthase
CM	Culture medium
CRISPR	Clustered regularly interspaced short palindromic repeat
DEG	Differentially expressed genes
DFC	dense fibrillar component
DNA	Deoxyribonucleic acid
DTT	Dithiothreitol
EGTA	Ethylene glycol tetraacetic acid
EXP2	exported protein 2
FC	fibrillar center
FDR	False discovery rate
FFT	Fast Fourier transform
FRAP	Fluorescence recovery after photobleaching
FUS	fused in sarcoma
FWHM	Full width at half maximal
GABA	Gamma-aminobutylic acid
GAD	glutamate decarboxylase
GADP	Glyceraldehyde-3-phosphate
GAPDH	glyceraldehyde-3-phosphate dehydrogenase
cGAS	cyclic GMP–AMP synthase
GC	granular component

GFP	Green fluorescent protein
GMP	Guanosine monophosphate
GO	Gene ontology
GOI	Gene of interest
GPI	Glycosylphosphatidylinositol
GST	glutathione S-Ttransferase
IC_{50}	Half maximal (50%) inhibitory concentration
IDP	Intrinsically disordered protein
IDR	Intrinsically disordered region
IFA	Immunofluorescence assay
IFN	Interferon
IPTG	Isopropyl β-D-thiogalactopyranoside
JAK-STAT	Janus kinase/signal transducers and activators of transcription
KEGG	Kyoto Encyclopedia of genes and genomes
LAT	linker for activation of T cell
LB	Luria-Bertani medium
LCD	Low-complexity domain
LLPS	Liquid-liquid phase separation
MAPK	mitogen-activated protein kinase
MAVS	mitochondrial antiviral-signaling
MED1	mediator complex subunit 1
miRISC	miRNA-induced silencing complex
MMV	Medicines for malaria venture
MOPS	3-(N-morpholino)propanesulfonic acid
NADH	Nicotinamide adenine dinucleotide reduced form
Ni-NTA	Nickel-nitrilotriacetic acid
NMR	Nuclear magnetic resonance
OE	Overexpression
PALM	Photoactivation localization microscopy
PBS	Phosphate bufferd saline
PBST	PBS with Tween 20
PCR	Polymerase chain reaction

PFK	phosphofructokinase
PHIST	Poly-helical Interspersed sub-telomeric
PK	pyruvate kinase
PKA	cyclic AMP-dependent protein kinase
PMSF	Phenylmethylsulfonyl fluoride
PROTAC	proteolytic targeting chimera
PVDF	Polyvinylidene difluoride
RAD23	radiation sensitivity proteins-23
RBC	Red blood cell
RESA	Ring-infected erythrocyte surface antigen
RNA	Ribonucleic acid
RPMI	Roswell Park Memorial Institute media
RSA	ring stage survival assay
SARS-CoV-2	severe acute respiratory syndrome coronavirus 2
SDS	Sodium dodecyl sulfate
SDS-PAGE	SDS polyacrylamide gel electrophoresis
SLiCE	Seamless ligation cloning extract
SLI	Selection-linked integration
SNF1	Sucrose nonfermenting 1
SP	Sulfadoxine-pyrimethamine
STING	Stimulator of interferon genes
STORM	Stochastic optical reconstruction microscopy
TCA	Tricarboxylic acid
TCP	Target candidate profile
TCR	T-cell receptor
TDP43	TAR DNA-binding protein 43
TGF-β	Transforming growth factor-β
TIRF	Total internal reflection fluorescence microscopy
TNRC6B	trinucleotide repeat-containing gene 6B
TORC1	Target of rapamycin complex 1
TPP	Target product profile
WHO	World Health Organization

List of figures

List of tables

Chapter 1

Introduction

1.1 Malaria

1.1.1 Epidemiology of malaria

Malaria is a devastating disease caused by *Plasmodium* parasites transmitted to humans when infected female Anopheles mosquitoes bite for a blood meal. Malaria is primarily seen in tropical and sub-tropical areas of Africa, Asia, and Central and South America. According to the World Malaria Report 2023 published by the World Health Organization (WHO), there were 249 million estimated malaria cases and 608 thousand deaths in 2022[1]. Malaria is a significant public health problem that causes economic and development issues, especially in sub-Saharan Africa, where 95% of cases and 96% of deaths occur. Children under five accounted for 80% of malaria deaths in the region.

Five species of *Plasmodium* parasites cause human malaria: *Plasmodium falciparum (Pf), Plasmodium vivax, Plasmodium ovale, Plasmodium malariae,* and *Plasmodium knowlesi.* Among them, *Pf* infection shows the most serious symptoms. It sometimes causes severe malaria, which can develop multiorgan failure, convulsions, and coma in vulnerable populations such as children under five, pregnant women, and travelers. *Pf* accounts for most malaria cases in sub-Saharan Africa, whereas *Plasmodium vivax* is mostly dominant outside Africa.

Plasmodium parasites have two hosts in their lifecycles. The parasite's invasion form, sporozoites, is released from a mosquito's salivary glands during a blood meal, and they first infect human liver cells. Within 10 to 15 days, the parasites multiply with schizogony and release merozoites into the bloodstream to start the asexual blood stage (ABS). Merozoites invade red blood cells and develop through three morphologically distinct stages of the parasite: ring, trophozoite, and schizont, and release merozoites to invade new red blood cells. Some of the ABS parasites differentiate into the sexual stage called gametocyte and are taken by mosquitoes during a blood meal. Male and female gametocytes become gametes in the mosquito's stomach and form zygotes, then develop ookinetes that invade the insect's midgut by penetrating the epithelial cells. Ookinetes develop into oocysts, and the parasite undergoes a division and multiplication process named sporogony, eventually releasing sporozoites that invade the mosquito's salivary glands for the subsequent invasion of the human body.

1.1.2 History of antimalarial drugs

The first antimalarial drug identified was quinine, isolated from the cinchona tree in 1820. The mechanism of action (MoA) of quinine is not fully elucidated, but it is thought to interfere with hemozoin formation[2]. Quinine has been an effective treatment and is used at the present date, although its resistance can be seen occasionally[3]. It is not the first-line malaria treatment drug; however, quinine is still recommended for treating first-trimester pregnant women with uncomplicated *falciparum* malaria[4].

Chloroquine was first discovered in 1934 in research to find a replacement for quinine and used in WHO's malaria eradication campaign from 1940s[5]. Chloroquine causes toxic free hematin accumulation in the parasite cell[6]. Chloroquine was a quite potent drug; however, its resistance

arose in several areas independently in the late 1950s and early 1960s, and *pfcrt* mutations, which account for the chloroquine resistance, can be seen in many parts of the world even today[7,8]. The use of chloroquine is recommended only in areas with chloroquine-susceptible infections, such as the Americas.

Pyrimethamine was discovered after the success of the same class drug, proguanil, in the 1950s[9]. Pyrimethamine inhibits dihydrofolate reductase of the parasite[10], but its monotherapy developed resistance in the short term, and sulfonamides were used as partner drugs to overcome this issue. The sulfadoxine/pyrimethamine (SP) combination was first implemented in 1967; however, the resistance spread quickly in Southeast asia[11]. SP resistance also spread in Africa in the late 1990s[12], but it is still used to protect pregnant women[4]. It is also used as seasonal malaria chemoprevention with a combination of amodiaquine and is thought to be cost-effective[13].

Mefloquine's efficacy in treating and preventing malaria was found in the late 1970s and 1980s[14]. The MoA of mefloquine might inhibit the parasite's 80S ribosome; however, it is not fully understood yet[15]. Despite its psychiatric side effects[16], mefloquine is one of the first-line treatments for uncomplicated *Pf* malaria in combination with artesunate.

Artemisinin was isolated from *Artemisia annua,* also known as sweet wormwood, by Chinese scientists in the early 1970s[17]. Artemisinin is thought to kill the parasite by producing toxic free radicals when interacting with heme-iron, specifically rich in the parasite cell[18]. Several artemisinin derivatives, such as artesunate and artemether, were developed to overcome the instability and low solubility of artemisinin and have been components of first-line drugs for the treatment of uncomplicated malaria since the WHO started the recommendation in 2006.

1.1.3 Artemisinin-based combination therapy and resistance

Artemisinin-based combination therapy (ACT), the combination of artemisinin derivatives and different class partner drugs, has been the first-line treatment of uncomplicated malaria since 2006. Currently, there are 6 ACTs recommended by WHO: artemether-lumefantrine, artesunate-amodiaquine, artesunate-mefloquine, dihydroartemisinin-piperaquine, artesunate plus sulfadoxine-pyrimethamine, and artesunate-pyronaridine. Over 200 million ACT treatment courses are used yearly[1], and the overall treatment success rate is higher than 90%[4]; however, emerging artemisinin partial resistance is confirmed in many countries, including sub-Saharan Africa. Artemisinin partial resistance first emerged in Cambodia[19], where slow parasite clearance and high treatment failure rates had been reported, then spread across the Greater Mekong Subregion[20,21]. The parasite recrudescence or failure of parasite clearance occurs in patients infected with resistant parasites, especially when they are also resistant to partner drugs of ACTs. The artemisinin partial resistance is defined by in vivo patient parasite clearance half-life longer than five hours[22], which differs from the resistance against other drugs defined by the fold changes of IC_{50}s against resistant strains. Tracking the partial resistance with in vivo assessment is quite laborious; therefore, the ring stage survival assay (RSA) was developed to measure artemisinin resistance in vitro[23]. In RSA, the parasite is treated with artemisinin in the early ring stage, the only time when the parasite can be resistant to the drug, and the parasite survival after two cycles of culture is measured. The slow parasite clearance phenotype of the resistance was strongly associated with mutations in Kelch13[22,24], which is required for endocytosis of hemoglobin from the host cell[25]. The Kelch13 mutations were also recently confirmed in Eastern African countries such as Eritrea[26], Rwanda[27-29], and Uganda[30]. Widespread artemisinin resistance will majorly impact health and the economy in African countries.

1.1.4 Recent effort for developing new drugs

One of the strategies to combat emerging resistance is developing a new class of antimalarials that can replace artemisinin derivatives. Medicines for Malaria Venture (MMV), a non-profit organization founded to facilitate the development of effective antimalarials in 1999, set clear goals for new antimalarials as target product profiles (TPPs) and target candidate profiles (TCPs) for efficient drug discovery[31]. Regarding malaria treatment TCP, a single oral dose regimen and rapid parasite clearance are essential to replace artemisinin derivatives and avoid the emergence of a new resistance. Many groups have been working on fulfilling those criteria; however, none of the pipeline drugs have shown the single-dose cure potential at a safe dose in humans. For example, Ganaplacide, the most promising candidate of the first new class antimalarial after artemisinin derivatives, will likely be a once-daily three-day treatment course[32], although it showed rapid parasite clearance and good pharmacokinetics profiles in earlier studies[33]. Continuous drug discovery studies are required to reduce the burden of malaria toward elimination and eradication.

Antimalarial drug discovery has been unsuccessful in the target-based approach. Despite the dedication of many groups for more than a decade, none of the target-based antimalarial candidates have succeeded yet[34], and all the new class pipeline drugs in clinical trials are developed from phenotypic screening[35-41]. Phenotypic screening is a powerful tool for obtaining potent compounds; however, the uncertainty of the mode of action can preclude quick drug development, mainly due to issues in safety profiles and structure-activity relationships[42]. Therefore, there is a shift toward target-based approaches in antimalarial drug discovery, and a consortium named Malaria Drug Accelerator (MalDA) suggested prioritizing molecular targets for antimalarial drug discovery[43]. They argued that these molecules with mammalian orthologs could be attractive drug

targets primarily based on their experience, even though selectivity will always be considered a risk. A new approach specifically targeting conserved proteins in the parasite is required to broaden the range of drug targets and can be a game changer in antimalarial drug discovery.

1.2 Liquid-liquid phase separation (LLPS)

LLPS is a general phenomenon that occurs in cells to regulate multiple biological processes. Instead of targeting particular molecular targets, controlling LLPS has been getting attention in drug discovery as it provides novel strategies to change molecular interactions, trafficking, and other non-gene-based biology. Even though there has been no clear evidence of LLPS in *Plasmodium* parasites, LLPS would provide new insights for antimalarial drug discovery regarding target variation and specificity.

1.2.1 Basics and history of LLPS in cells

LLPS is a thermodynamically driven process first investigated well in polymer science, where a uniform liquid phase is divided into two distinct liquid phases. Emerging evidence demonstrated that biomolecules such as proteins and nucleic acids also undergo LLPS to form distinct liquid phases without the involvement of a lipid membrane[44]. LLPS has been recognized as a key mechanism for organizing intracellular components and plays essential roles in various biological processes, including gene regulation[45], signaling[46], and stress response[47].

LLPS in cells was first reported by Brangwynne *et al.* in 2009. They demonstrated that P granules, membrane-less organelles in *Caenorhabditis elegans* germ cells, behaved like liquid and segregated from the cytosol in a condensed state[48]. Since then, several studies have reported that

other membrane-less organelles are formed through LLPS of proteins and nucleic acids, and they behave like liquid droplets in cells[49]. In 2012, Li *et al.* clearly showed that *in vitro* reconstitution of LLPS was possible, and it formed droplet-like condensates facilitated by multivalent interactions of proteins[50]. In the same year, Kato *et al.* demonstrated that the FUS protein low-complexity domain forms a gel-like structure through LLPS, suggesting cell-free reconstitution of RNA granules *in vitro*[51]. Through these observations, the perspectives of researchers on previously known intracellular processes have changed, and numerous studies have revealed the involvement of LLPS in various phenomena within the cell by both *in vitro* and *in vivo* experiments.

1.2.2 Basic principles of LLPS

The main driving force of LLPS is transient intramolecular and intermolecular interactions of multivalent molecules, which have several motifs to interact[52]. These interactions are promoted by electrostatic interactions and π (pi) electron interactions of cationic and aromatic amino acids[53,54], unlike traditional protein-protein interactions facilitated by hydrophobic interactions. With this characteristic, biomolecular condensates can quickly form and dissociate with slight changes in pH, temperature, salt concentration, and the concentration of proteins[55-57], allowing LLPS to regulate biological processes quicker than existing mechanisms. It is now widely accepted that multivalent sequences are often found in disordered regions of intrinsically disordered proteins (IDPs), which partly lack fixed three-dimensional structures[58]. IDPs are often found in biomolecular condensates and are thought to facilitate biomolecular condensate formation. An in silico analysis presented that 48% of *Plasmodium* proteins have intrinsically disordered regions with 40 or more residues, which is relatively high compared to 30% of other eukaryotic proteins[59].

Although no reports have shown the function of LLPS in *Apicomplexan* parasites, LLPS likely plays some critical roles in *Plasmodium* parasite biology.

1.2.3 Possible functions of LLPS and their examples

LLPS creates a non-membrane-bound organization by forming distinct liquid phases, which allows different molecules to be sequestered into discrete compartments. This characteristic of LLPS leads to several possible functions that are essential to regulate cellular biological processes.

Firstly, sequestered high concentrations of enzymes and substrates can potentially allow higher enzymatic activity within condensates. For example, purine biosynthesis-related enzymes are compartmented in clusters named "purinosomes" in human cells under purine-depleted conditions to accelerate the enzymes' reactions[60,61]. Recent studies demonstrated that purinosomes comprise at least ten enzymes of the purine biosynthesis and salvage pathways, efficiently converting phosphoribosyl pyrophosphate to adenosine monophosphate and guanosine monophosphate[62].

Secondly, the sequestration of certain molecules in condensates leads to enzyme reaction specificity. For example, Argonaute2 (Ago2) and trinucleotide repeat-containing gene 6B protein (TNRC6B), two core proteins of the human miRNA-induced silencing complex (miRISC), form condensates through LLPS in vitro and in vivo[63]. Target mRNAs of miRISC are identified by miRNA bound to Ago2 and specifically sequestered into Ago2-TNRC6B droplets. This mRNA sequestration allows miRISC to deadenylate and degrade target mRNAs efficiently and precisely.

Lastly, the condensation of molecules can lead to concentration buffering when an excess number of molecules exists. For example, cyclic AMP (cAMP)-dependent protein kinase (PKA)

subunit RIα forms condensates enriched with cAMP for buffering to prevent unnecessary signaling[64], which may explain how cAMP signaling is controlled spatiotemporally in cells. The importance of cAMP buffering was illustrated by showing that the DnaJB1-PKA_{cat} fusion oncogene, which can be seen in fibrolamellar hepatocellular carcinoma patients[65], disrupts RIα condensates and induces abnormal cAMP signaling and cell transformation.

1.2.4 LLPS in biological processes

Many studies have suggested that LLPS may play a key role in several biological processes. One of the best-studied roles of LLPS is gene regulation. For example, the nucleolus, a structure within the nucleus involved in synthesizing ribosomal RNA, is formed through several proteins and RNA. Nucleolus has three components named the fibrillar center (FC), the dense fibrillar component (DFC), and the granular component (GC), and it was demonstrated that DFC protein fibrillarin and GC protein nucleophosmin form condensates through LLPS *in vitro*[66]. Furthermore, fibrillarin condensates were formed within nucleophosmin condensates when mixed with ribosomal RNA, which suggested that the LLPS of these proteins organize the complex structure of the nucleolus and regulate ribosomal RNA synthesis. LLPS may also regulate gene expression more broadly. In 2017, chromatin-mediated gene regulation by LLPS of heterochromatin protein 1 was reported from two groups simultaneously[67,68]. Moreover, several transcription factors and cofactors, including BRD4 (bromodomain containing 4) and MED1 (mediator complex subunit 1), form super-enhancer condensates through LLPS, which is required for efficient transcription by facilitating the concentration and compartmentalization of transcription components[45]. LLPS may play pivotal roles in both gene suppression and enhancement.

Another example of LLPS function is signal transduction. Cyclic GMP–AMP synthase (cGAS) is a cytoplasm double-stranded DNA sensor that induces type 1 interferon via the cGAS-stimulator of interferon genes (STING) pathway important for antiviral and antitumor immunity[69,70]. It was reported that cGAS formed droplet-like condensates when mixed with DNA, and longer DNA induced more cGAS LLPS[46]. Interestingly, cGAS enzyme activity was enhanced depending on the efficiency of condensate formation, explaining that LLPS may be a key determinant of innate immune signaling. Moreover, LLPS may also control adaptive immune signaling. Su *et al.* reconstituted the 12-component T-cell receptor (TCR) signal transduction system and found phosphorylated LAT (linker for activation of T cell) protein forms condensate with Grb2 and Sos1 on model membranes[71]. The condensate formation was also confirmed in Jurkat T cells, and MAPK (mitogen-activated protein kinase) signaling was promoted along with the LAT LLPS. They also found that a transmembrane phosphatase CD45, an inhibitor of TCR signaling[72], was excluded from LAT condensates, which suggested the LLPS-specific regulation manner of signal transduction.

LLPS may also be vital for the stress response of the cell. It is widely accepted that stress granules are formed through LLPS of RNA-binding proteins and RNAs dissociated from ribosomes after several kinds of stress, such as starvation, oxidation, and heat shock[73]. Stress granules segregate RNAs and translational machinery from the cytosol to prevent excess translation and damaging molecules required for survival. Different types of stress induce different stress granules concerning their components and physical properties[74,75]; however, it was reported that G3BP1, an RNA-binding protein implicated essentiality in stress granule formation[76], is a molecular switch of RNA-dependent LLPS[77]. G3BP1 has three intrinsically disordered regions (IDR1, 2, and 3), and IDR1 and IDR3 interact in a steady state. However, when amino acid S149

within IDR1 is dephosphorylated, IDR3 dissociates from IDR1 and binds to RNA, which triggers LLPS to facilitate stress granule formation.

Intracellular degradation pathways may also be controlled by LLPS. Autophagy is a conserved degradation pathway where the double membrane structure autophagosome segregates intracellular material for degradation and recycling[78]. It was well known that several Atg genes cooperate to form pre-autophagosomal structure (PAS) to start autophagy[79], and a recent study demonstrated that PAS was a liquid condensate of Atg proteins[80]. Multivalent interactions of Atg13 and Atg17 promoted the phase separation, and phosphorylation of Atg13 inhibited the PAS droplet formation[80], which was consistent with the fact that a nutrient sensor target of rapamycin complex 1 (TORC1) phosphorylates Atg13 to inhibit autophagy in a nutrient-rich condition[81]. The ubiquitin-proteasome system is another major protein degradation system required for a number of cellular processes[82]. In this system, substrate proteins are ubiquitinated by several ubiquitin ligases, pulled out from the membrane by p97, and then transported to the proteasome by shuttle proteins such as radiation sensitivity proteins-23 (RAD23). The proteasome droplet formation through LLPS was recently discovered when cells were under hyperosmotic stress[83]. Hyperosmotic stress causes nucleolus stress and inhibition of rRNA transcription, which leads to a high ubiquitination rate of orphan ribosomal proteins and the formation of proteasome droplets within seconds. It was also demonstrated that a shuttle protein RAD23B and ubiquitinated substrates form the scaffold of proteasome droplets. LLPS may allow cells to have several survival strategies by regulating complex biological processes quickly and precisely.

1.2.5 LLPS-related diseases and therapeutic applications

Some LLPS functions are suggested to have relationships with diseases and pathological functions. For example, LLPS disruption and following aggregation of certain proteins cause several neurodegenerative diseases, such as amyotrophic lateral sclerosis (ALS)[84], Alzheimer's disease[85], Parkinson's disease[86], and frontotemporal dementia (FTD)[87]. This section reviews details of LLPS functions in diseases and their possible therapeutic applications.

TAR DNA-binding protein 43 (TDP-43), an RNA/DNA-binding protein involved in RNA metabolism, mRNA transport, and stress granule formation[88], forms insoluble ubiquitinated inclusions identified as a key pathological feature of ALS and FTD[89,90]. It was reported that mutations in the *TARDBP* gene, which encodes the TDP-43 protein, were observed in 4% of familial ALS and 1.5% of sporadic ALS[91]. The TDP-43 protein has both nuclear localization signal and nuclear export sequence, two RNA-binding motifs, and the glycine-rich low-complexity domain (LCD), and most of the *TARDBP* gene mutations were found in the LCD[92], which suggested the relation of LLPS and the diseases. LLPS of TDP-43 facilitated by the LCD was reported from several groups since 2015[47,93], and it was also demonstrated that altered localization to the cytosol led to reduced interaction with RNA, which impeded the LLPS of TDP-43, resulting in the aggregation of TDP-43[94]. LLPS-based drug discovery for ALS/FTD should be underway, but not many of them have been disclosed yet. High-content screening based on stress granule properties identified small molecules that prevent TDP-43 recruitment into stress granules, which could be a good starting point for an LLPS-modulating ALS/FTD drug. Other than TDP-43, there are at least 25 proteins related to ALS/FTD, and more than half are confirmed to undergo LLPS[95]. It is important to understand how these proteins are kept soluble in a steady state and what the

triggers of LLPS or aggregation can be for elucidating the mechanism of neurodegenerative diseases and their new treatments.

Aberrant LLPS is thought to cause tumorigenesis due to abnormal chromatin organization, oncogenic transcription, and disturbed antitumor signaling pathways. As described above, super-enhancers are formed through LLPS and their modification of gene transcription results in the expression of key tumor pathogenesis genes[96]. It was reported that signaling factors for the Wnt, TGF-β, and JAK/STAT pathways are incorporated into the super-enhancer liquid condensate in an IDR-dependent manner, and the Wnt coactivator β-catenin was required for the liquid condensate formation through LLPS[97]. The link between the hyperactivation of Wnt/β-catenin has been demonstrated in several types of cancers[98]. There are several possible strategies to treat cancers by targeting LLPS, but the most promising one could be the proteolytic targeting chimera (PROTAC) technology for downregulating the target protein expression[99]. PROTACs are molecules having two ligands; one is for binding to the protein of interest, and the other is for binding to the E3 ubiquitin ligase. They can reduce the amount of the protein of interest by proteasomal degradation, and more than 20 PROTACs are under clinical trials to treat several diseases, mainly cancers[100]. ARV-825, a PROTAC that targets BRD4 and super-enhancer formation, showed anticancer activity and could be the first LLPS-modulating PROTAC drug in the future[101,102].

Another example of disease-related LLPS is found in viral infection. Many reports have demonstrated the functions of LLPS in the lifecycle of viruses, but they seem to be different depending on the virus species[103]. In the case of severe acute respiratory syndrome coronavirus 2 (SARS-CoV-2), many reports showed that its nucleocapsid protein (NP) undergoes LLPS *in vitro* and in cells, and it is essential for viral replication, genome packaging, and host immune evasion[104-

[111]. An interesting observation of NP LLPS was reported by Wang *et al.*, where NP liquid condensates disrupted the formation of the mitochondrial antiviral-signaling (MAVS) protein condensates[108]. MAVS is a mitochondrial protein mediating innate immunity against RNA viruses and is thought to undergo LLPS for facilitating antiviral signaling[112]; therefore, the disruption of MAVS condensates by NP led to a reduction of IFN expression, which can be a novel mechanism of enhancing the pathogenicity by LLPS. They also demonstrated the *in vitro* and *in vivo* efficacy of an NP-targeting interfering peptide, which could disrupt the NP droplet formation in cells. This result suggested the possibility of novel antivirals targeting the virus-specific LLPS.

1.3 G-body

Studies have shown that several metabolic enzymes are organized into membrane-less, droplet-like cell structures through LLPS in the same way as purinosomes described above[113]. The glycolytic body (G-body) is one of those structures containing glycolytic enzymes. Abundant evidence has shown co-localization and clustering of glucose metabolism enzymes in several species and cell types, including *Arabidopsis* cells, *Drosophila* flight muscles, *Saccharomyces cerevisiae*, human cancer cells, erythrocytes, and cardiomyocytes[114-118]. However, these observations were mainly based on an association of enzymes in a steady state, and the principal or trigger of the enzyme clustering was not explained very well.

The assembly of glycolytic enzymes in response to hypoxia was first observed in 2011, where they demonstrated that glyceraldehyde-3-phosphate dehydrogenase (GAPDH), the glycolytic enzyme catalyzing the sixth step, formed foci in HeLa cells under hypoxia[119]. Subsequently, Miura *et al.* reported that several glycolytic enzymes were condensed in foci, later

called ‘G-body’, under hypoxia in *Saccharomyces cerevisiae*[120]. They also demonstrated that mitochondrial reactive oxygen species and Sucrose nonfermenting 1/ AMP-activated protein kinase (SNF1/AMPK) were required for the foci formation, which changed the metabolic carbon pathway and increased the flux of pyruvate and oxaloacetate synthesis. The components of G-body were identified by G-body isolation and proteome analysis from yeast cells performed by Jin *et al.* in 2017[121]. G-body contained not only glycolytic enzymes but also chaperones, proteasomal subunits, and fatty acid synthesis-related proteins, which suggested that G-body formation is associated with other metabolic pathways and ATP-required cellular processes. Consistent with this result, glycolysis was facilitated by G-body formation to produce ATP efficiently for increasing cell survival. They also demonstrated the G-body formation of PFKL in HepG2 cells in hypoxia, which implied that G-body was a conserved phenomenon to overcome stress. The same group demonstrated g-body formation through LLPS by using fluorescence recovery after photobleaching (FRAP) analysis and observing the fusion of G-bodies of mated yeast cells[122]. They argued that slow and partial fluorescence recovery after bleaching suggested that the G-body behaves as gel-like droplets. RNAs were an important scaffold of G-body since Pfk2-tethered RNase expression disrupted G-body formation, which is consistent with the former study that demonstrated glycolytic enzymes are RNA-binding proteins without RNA-binding motifs[123]. Another example of G-body was observed in neurons of *Caenorhabditis elegans*. The PFK-1.1 puncta were formed near presynaptic release sites in hypoxia, which was required for maintaining synaptic vesicles under stress[124]. Aldolase was also incorporated into the puncta and required for its formation, suggesting that the G-body of *Caenorhabditis elegans* is also a multi-enzyme structure. The puncta was formed within 10 min in hypoxia and dispersed quickly after 5 min of normoxia[125], which was different from the result of G-body in yeast cells as it required at least 6

hours of hypoxic culture in yeast[120]. On the other hand, they also demonstrated that longer hypoxia formed more rigid G-bodies, consistent with the gel-like G-bodies in yeast. An interesting observation was that the local high concentration of PFK-1.1 was the trigger of G-body formation. PFK-1.1 was distributed unevenly in neurons to meet the local energy demand in normoxia, and G-bodies were thought to be required for narrowing down the target area to sustain synaptic function under stress.

It is well known that kinetoplastids and diplonemids, such as *Trypanosoma cruzi*, have a membrane-bound organelle named glycosome[126]. This structure contains most of the glycolytic enzymes; however, there have not been any reports on membrane-bound or membrane-less glycolytic organelle formation in Apicomplexan parasites, including *Pf*, though it highly depends on glycolysis as a major energy source.

1.4 Glycolysis of Plasmodium parasite

Glycolysis is a well-conserved metabolic pathway in the cytoplasm for energy production. It is a ten-step reaction that converts glucose into pyruvate and can be separated into two phases: the energy investment phase and the energy-yielding phase. In the energy investment phase, glucose is phosphorylated to generate fructose-1,6-biphosphate by two enzymatic reactions using two ATP molecules. The subsequent reactions cleave the six-carbon sugar into two three-carbon molecules, and then interconversion allows the extraction of two glyceraldehyde-3-phosphate (GADP) molecules. The energy yield phase begins with the oxidation of GADP, accompanied by the production of NADH. Each GADP molecule is converted into pyruvate through four enzymatic

reactions, yielding two ATP molecules. Overall, four ATP molecules and two NADH molecules are generated in glycolysis by using two ATP molecules.

Glycolytic enzymes are conserved in Plasmodium species, and glycolysis is the primary source of energy production in the asexual blood stage of the parasites, consistent with the fact that several TCA cycle enzymes and the β subunit of ATP synthase are dispensable[127-129]. Therefore, some studies have tried to target the hexose transporter for antimalarial drug development[130,131]. Although glycolysis is essential for the blood stage parasite, its reaction rates change drastically during intraerythrocytic development[132], which may be difficult to explain with the simple regulation of enzyme expression levels. Considering these facts and the studies in other organisms, we hypothesized that the G-body is also formed in the parasite cell and plays a critical role in metabolic regulation. Several glycolytic enzymes of *Pf* are disordered proteins, and PfPFK9 is the orthologue of yeast Pfk2 with one or more disordered regions, which implies its contribution to G-body formation in the parasite cell.

Chapter 2

Methodology

2.1 Parasite culture

2.1.1 Culture of *Plasmodium falciparum*

Pf 3D7 parasites[133] were maintained in complete medium (CM, Roswell Park Memorial Institute media (RPMI) 1640 medium with 25 mM HEPES (Thermo Fisher Scientific, Waltham, MA, USA) supplemented with 25 mg/L gentamicin (Thermo Fisher Scientific, USA), 50 mg/L hypoxanthine (MilliporeSigma, Burlington, MA, USA), 23.8 mM sodium bicarbonate (FUJIFILM Wako, Osaka, Japan), and 0.5% Albumax II (Thermo Fisher Scientific, USA)) at 2% hematocrit of O^+ human erythrocytes (The Japanese Red Cross Society, Tokyo, Japan) at 37 °C with the mixed gas (5% O_2, 5% CO_2, and 90% N_2). The parasite culture was diluted every two or three days to maintain the parasitemia between 0.1% and 5%, typically.

2.1.2 Counting parasites

For daily culture maintenance, parasitemia was measured by an automated hematology analyzer XN-30[134] (Sysmex, Kobe, Japan). For checking the parasitemia and parasite re-emergence during the drug selection, thin blood smears of the culture were fixed with methanol

and stained with Giemsa's staining solution (MilliporeSigma, USA), then observed with inverted microscopy.

2.1.3 Making parasite cell stocks

The parasite culture was pelleted by centrifuge and then added 0.33 times the pellet volume of SF-60 glycerolyte (Fuso Pharmaceutical Industries, Osaka, Japan) dropwise through gentle mixing. After 5 min incubation at room temperature, the aliquot was added 1.33 times the pellet volume of SF-60 dropwise with a gentle mix, then distributed to cryovials and stored at -80 °C.

2.1.4 Thawing cell stocks

Cryostocks of the parasite were thawed in a 37 °C water bath. Aliquot was transferred to a centrifuge tube and added 0.2 times the volume of 12% NaCl dropwise, incubated for 5 min at room temperature. Then, 10 times the volume of 1.6% NaCl was added dropwise with a gentle mix and incubated for 5 min at room temperature. The aliquot was centrifuged and removed supernatant, added 10 times the volume of 0.9% NaCl/0.2% dextrose, and centrifuged again. The supernatant was removed, and the pellet was suspended in an appropriate volume of CM and transferred to cell culture flasks.

2.1.5 Parasite purification

Parasites were purified by magnetic separation[135]. Briefly, an LS column (Miltenyi Biotech, Bergisch Gladbach, Germany), a three-way stop cock (Terumo, Tokyo, Japan), and a 21G blunt-tip needle (Terumo, Japan) were connected and set on QuadroMACS Separator (Miltenyi Biotech, Germany). The column was filled with CM using a 2.5 mL syringe connected to the three-way

stop cock. The parasite culture was poured onto the column and let through the blunt-tip needle dropwise with gravity flow. Two mL of CM was used for the column wash, and another 2 mL of CM was applied to elute purified parasites. Typically, a trophozoite and schizont-rich aliquot with 80~95% parasitemia was obtained.

2.1.6 Sorbitol synchronization

The parasite culture was centrifuged, removed supernatant, and suspended in 10 times erythrocyte volume of 5% D(-)-sorbitol[136] (Nacalai, Kyoto, Japan). After 10 min of incubation at room temperature, the parasite was centrifuged, washed with CM, centrifuged again, and suspended in CM.

2.2 Generation of transgenic parasites

2.2.1 Plasmid construction

For fluorescent tagging of glycolytic enzymes, selection-linked integration[137] (SLI) was induced by transfection of pKIC-ter plasmid derived from pD3 plasmid[138,139], which has human dihydrofolate reductase and bacterial Neomycin-kanamycin phosphotransferase II (NPTII) and as selection markers against WR99210 and G418, respectively. Myc tag, a green fluorescent protein mNeonGreen[140] (mNG), skip peptides P2A and T2A[141] tandem sequence was synthesized and cloned into pD3 by Seamless ligation cloning extract (SLiCE) reaction[142], resulting in the plasmid pKIC-ter. The pKIC-ter plasmid was restricted with NotI, and the C-terminal sequence of GOIs amplified from the 3D7 genomic DNA (gDNA) or synthesized DNAs (Twist Biosciences, South

San Francisco, CA, USA, summarized in Table A.1) was inserted by SLiCE. The primers (FASMAC, Kanagawa, Japan) used for the amplification are summarized in Table 2.1.

2.2.2 Transfection and drug selection of *Plasmodium falciparum*

Erythrocytes were suspended in cytomix[143] (120 mM KCl, 0.15 mM $CaCl_2$, 10 mM K_2HPO_4/KH_2PO_4 (pH 7.6), 25 mM HEPES-KOH (pH 7.6), 2 mM EGTA (pH 7.6), 5 mM $MgCl_2$, adjusted to pH 7.6 with KOH), centrifuged, and the supernatant was removed. Fifty μg of plasmid DNA and 150 μL packed RBCs were mixed and completed to 400 μL with cytomix in 0.2 cm electroporation cuvette (Bio-Rad Laboratories, Inc., Hercules, CA, USA). Electroporation was performed with GenePulser (Bio-Rad Laboratories, USA) on the conditions below: Voltage = 310 V, Capacitance = 975 μF, Resistance = ∞, Cuvette = 2 mm. Erythrocytes were washed with cold RPMI twice and then suspended in CM. The 3D7 parasite was inoculated to the electroporated RBCs at 0.1-0.3% parasitemia and cultured in a flask as described above. When parasitemia reached ≈5%, drug selection was initiated by adding the final 1 nM WR99210 (MilliporeSigma, USA) to the culture and continued for 10 days. After the parasite re-emergence, 400 μg/mL G418 (FUJIFILM Wako, Japan) was added to the culture for 10 days to select the parasite with genome insertion of the plasmid sequence.

2.2.3 Diagnostic PCR

The gDNA of the parasite was purified with DNeasy Blood & Tissue kits (QIAGEN, Venlo, Netherlands). Insertion of the plasmid sequences was confirmed by PCR using gDNA as templates. Primers p1 to p4 (Table 2.1, synthesized by FASMAC, Japan or Hokkaido System Sciences, Hokkaido, Japan) were used for genotyping. PCR reaction and program are outlined below.

- 2x Quick Taq HS DyeMix (Toyobo, Osaka, Japan) – 5 µL
- Forward primer (2 µM) – 1 µL
- Reverse primer (2 µM) – 1 µL
- DNA template – varied depending on sample concentration
- H_2O – up to 10 µL

Step	Temperature	Time
Pre-denature	94 °C	2 min
Amplification 30 cycles	94 °C 55 °C 68 °C	30 sec 30 sec 1.5 min
Hold	12 °C	∞

Primer name	Sequence
PFK9_F1	acgtaacagacttaggaggGAGTTTAGCATTATTAAAGAC
PFK9_R1	taattcccggggtgttcatGTTCATTCTTTTTCTCTGGTT
HK_F1	ACGTAACAGACTTAGGAGGGTGCATATCAAAAAGGTAGAGGTAC
HK_R1	TAATTCCCGGGGTGTTCATTGGTAATTGTGGAATGTCC
PGM1_F2	acgtaacagactTAGgaggAGAATTTCAAATTCGACGTTG
PGM1_R2	CTTCTCCCTTACTCACCATTTTTGCTTTTCCTTGGTTG
p2	CGGTACCTTGACCTACCATATC
p3	caggaaacagctatgaccatg
PFK9_p1	GCTGATGTTGGAAAAAATTATG
PFK9_p4	GAAATATACACACATGGATAAATAC
HK_p1	TTCCCTTGTACATCACCTTCAAT
HK_p4	TCTTCACACACTCACATACAGACAA
PGM1_p1	GTGAAAGTACATGGAACAAGG
PGM1_p4	TATCCACAAATGGGAAACCTCG
PyrK_p1	ACCGCATCAGCTATTAGTTCC
PyrK_p4	ATACATTAAAGAAAGGCAAAGG
PGK_p1	TATTGAAGAAGAAGGTAAAGGTGTTG
PGK_p4	CATACATACACACATACAATAAG
TIM_p1	AGCAAACTGGAAATGTAATGGAAC
TIM_p4	ATATAGAATACGTTCACCTC
GPI_p1	TTTGGGATTGGGTAGGAGGTC
GPI_p4	AACCCATATTTGCACTTTCACAC

Table 2.1 Primers used for the plasmid construction and diagnostic PCR.

2.2.4 Cloning of the parasite

Limiting dilution was performed for the parasite cloning. The parasite culture was diluted to 2.5 parasites/mL or 1.25 parasites/mL with 2% hematocrit CM and dispensed to 96-well plates at 200 µL/well (0.5 parasites/well or 0.25 parasites/well). The plates were maintained at 37 °C with the mixed gas in a humid chamber. On day 7 and day 14, 100 µL supernatant was removed, and 100 µL 2% hematocrit CM was added to the wells. On day 21, 100 µL/well of the culture was transferred to a 96-well black plate and added 50 µL Sybr mix (20 mM Tris-HCl, pH 8.0, 5 mM EDTA, 0.1% Triton X-100, 0.15% KM-70 (Shinetsu Chemical, Nagano, Japan), 3X SYBR Green I (Invitrogen, Waltham, MA, USA)). The fluorescence intensity was measured at 485/20 nm excitation and 535/25 nm emission with SpectraMax Paradigm (Molecular Devices, San Jose, CA, USA) to identify positive wells.

2.2.5 Western blot

The parasite culture was pelleted and suspended in PBS containing 1× cOmplete protease inhibitor cocktail (Roche, Basel, Switzerland). The final 0.15% saponin was added to the solution and incubated on ice for 8 min. The parasite was pelleted by centrifuge at 16,900 × g and washed twice with PBS containing 1× cOmplete protease inhibitor cocktail. NuPAGE LDS Sample Buffer containing NuPAGE sample reducing agent (Invitrogen, USA) was added to the pellet to obtain 10^6 parasites/µL and heated at 70 °C for 10 min. Ten to 25 µL of the prepared solution was applied to a NuPAGE 4 to 12% Bis-Tris mini protein gradient gel (Invitrogen, USA), and SDS-PAGE was performed in MOPS SDS Running Buffer (Invitrogen, USA) at 200 V for 40 min. Membrane transfer to Polyvinylidene difluoride (PVDF) membrane (FUJIFILM Wako, Japan) was done using the XCell II blot module and NuPAGE transfer buffer (Invitrogen, USA) at 30 V for an hour. The

membrane blocking was performed with Bullet Blocking One (Nacalai, Japan) for 5 min at room temperature. PBS containing with 5% Bullet Blocking One was used for antibody dilution. Antibodies and reaction conditions used in this study are summarized in Table 2.2. SuperSignal West Pico PLUS Chemiluminescent Substrate (Invitrogen, USA) was used to generate chemiluminescent signals, and images were taken by Luminograph II (Atto, Tokyo, Japan) or FUSION-FX6.EDGE (Vilber, Collégien, France).

Antibody name	Supplier	Dilution factor	Incubation time and temperature
Myc-Tag (9B11) Mouse mAb #2276	Cell Signaling Technology, Danvaese, MA, USA	500	1 hour, room temperature
Neomycin phosphotransferase II Antibody (4B4D1)	Novus Biologicals, Centennial, West Grove, CO, USA	500 or 1000	1 hour, room temperature
Anti-EXP2 Rabbit polyclonal antibody	Ehime University, Ehime, Japan	2500	1 hour, room temperature
Peroxidase AffiniPure Goat Anti-Mouse IgG (H+L)	Jackson ImmunoResearch, PA, USA	5000 or 10000	30 min, room temperature
Peroxidase AffiniPure Goat Anti-Rabbit IgG (H+L)	Jackson ImmunoResearch, USA	5000 or 10000	30 min, room temperature

Table 2.2 Antibodies and reaction conditions for Western blot.

2.3 Microscopic analysis of parasites and G-body

2.3.1 G-body induction

Low glucose CM (glucose-free RPMI 1640 (Thermo Fisher Scientific, USA) medium supplemented with 25 mg/L gentamicin, 50 mg/L hypoxanthine, 25 mM HEPES, 23.8 mM sodium bicarbonate, 0.5% Albumax II, and 5 mM glucose (FUJIFILM Wako, Japan) was used for induction of G-body formation. The parasite cultured in the same CM but supplemented with 10 mM glucose was used as a negative control. The 3D7 parasite expressing mNG tagged PFK9 (3D7-

PFK9-mNG) was diluted in 2% hematocrit low glucose CM at 0.1-0.3% parasitemia and maintained for 2 to 4 days until G-body was observed by microscopy.

2.3.2 Live imaging of the parasite

Hoechst 33258 (Dojindo, Kumamoto, Japan) was added to the parasite culture at 2 μg/mL for nuclear stain. After 30 min of incubation at 37 °C, the parasite culture was washed with CM, centrifuged, applied on a microscope slide, and sealed with a coverslip. Images were taken by LSM780 (Zeiss, Oberkochen, Baden-Württemberg, Germany) or DMi8 (Leica, Wetzlar, Hesse, Germany) on the settings summarized in Table 2.3.

LSM780 settings	
Scan Mode	plane
Objective	alpha Plan-Apochromat 100X/1.46 Oil DIC M27 Elyra
Pixel dwell	3.15 μsec
Average	line 4
Track setting (Hoechst)	405 nm Laser, Detector range: 406-490 nm
Track setting (mNG)	488 nm Laser, Detector range: 489-569 nm

DMi8 settings	
Objective	HC PL FLUOTAR 100X/1.32 OIL
Filter (Hoechst)	EX: 325-375 nm, DC: 400 nm, EM: 435-485 nm
Fileter (mNG)	EX: 460-500 nm, DC: 505 nm, EM: 512-542 nm
Exposure time	Hoechst: 50 msec, mNG: 300 msec

Table 2.3 Settings of LSM780 and DMi8.

2.3.3 Calculation of G-body-like structure area

The image analysis was performed using ImageJ Fiji[144]. For calculating G-body-like structure area and intensity, background subtraction was first performed, and parasite cells were cropped manually. Enhance contrast was performed for each cropped image, and then the areas and integrated density of G-body-like structures were calculated after thresholding at an intensity of 40. For calculating Clustering %, parasite cell images were automatically cropped after performing Subtract background, Thresholding by Huang's fuzzy thresholding method, Analyze particle, and Enhance contrast. Clustering % was calculated by areas measured after thresholding at an intensity of 90 divided by areas measured without thresholding. Graphs were prepared using GraphPad Prism (GraphPad Software, La Jolla, MA, USA), and statistical analyses were performed with EZR (Saitama Medical Center, Jichi Medical University, Saitama, Japan)[145].

2.3.4 Di-4 staining

The tagged PFK9-expressing parasite was cultured in 10 mM or 5 mM glucose-containing CM for 4 days. The parasite was centrifuged, and the supernatant was replaced with 5 mM glucose-containing RPMI 1640 with Di-4-ANEPPDHQ (Thermo Fisher Scientific, USA) at 2 μg/mL, incubated at 37 °C for 30 min. The parasite was washed with 10 mM or 5 mM glucose-containing CM, centrifuged again, applied on a microscope slide, and sealed with a coverslip. Images were taken by LSM780 on the settings summarized in Table 2.4.

LSM780 settings for Di-4	
Scan Mode	plane
Objective	alpha Plan-Apochromat 100X/1.46 Oil DIC M27 Elyra
Pixel dwell	3.15 µsec
Average	line 4
Track setting (Hoechst)	405 nm Laser, Detector range: 406-490 nm
Track setting (mNG)	488 nm Laser, Detector range: 489-516 nm
Track setting (Di-4)	488 nm Laser, Detector range: 604-759 nm

Table 2.4 Settings of LSM780 for observing Di-4-stained parasites.

2.3.5 Osmotic stress induction

The tagged PFK9-expressing parasite cultured in the standard CM was centrifuged and suspended in a medium containing 50 mM or 100 mM sodium chloride. After 5 min of incubation at 37 °C, the parasite was centrifuged, applied on a microscope slide, and sealed with a coverslip. Images were taken by LSM780 on the settings summarized in Table 2.3. Graphs were prepared using GraphPad Prism, and statistical analyses were performed with EZR.

2.3.6 Total internal reflection fluorescence microscope (TIRF) imaging

The tagged PFK9-expressing parasite was cultured in 10 mM or 5 mM glucose-containing CM for 72 hours and purified by magnetic separation. The parasite cells were applied on coverslips coated with Poly-d-Lysine (4-15 kDa) (MP Biomedicals, Santa Ana, CA, USA) at 10 µg/cm^2 and incubated at 37 °C for 20 min, then the coverslips were washed with PBS twice. Five µL of spent medium was applied on a microscope slide and sealed with the coverslip. Images were taken by LSM780 on the settings summarized in Table 2.5.

LDM780 TIRF settings	
Illumination Mode	TIRF
Objective	alpha Plan-Apochromat 100X/1.46 Oil DIC M27 Elyra
Pixel time	1.58 µsec
Averaging	4
Lasers	488 nm : 5.0%
TIRF angle	66.52°
Collimator Camera ELYRA	1739
Exposure time	32.5 msec

Table 2.5 Settings of LSM780 for TIRF imaging.

2.3.7 Power spectrum and autocorrelation analyses of TIRF images

The image analysis was performed with ImageJ Fiji and OriginPro 2023b (Lightstone, Park Avenue, NY, USA). For power spectrum analysis, background subtraction was performed and at least 3 segmented lines in the parasite cytosol longer than 5 µm were drawn and measured intensity along with the lines using Fiji. The 8-bit intensity data with distance was transferred to OriginPro, and a fast Fourier transform (FFT) was performed to obtain the power spectrum. The power spectrum was normalized by its highest value, then plotted on a double logarithmic scale, and linear regression analysis was done with OriginPro. The parasite cytosol's 25 × 25 pixel intensity was exported for autocorrelation analysis using Fiji. The data was transferred to OriginPro, and a two-dimensional FFT was performed to obtain the power, followed by a two-dimensional inverse FFT to obtain the real number matrix, corresponding to the two-dimensional spatial autocorrelation function[146]. The autocorrelation function was normalized over all angles and fitted with a single Gaussian function with OriginPro. PFK9 cluster sizes were estimated from the full width at half maximum (FWHM) of the fitting.

2.4 Omics analysis for G-body-induced parasites

2.4.1 Metabolome analysis

The tagged PFK9-expressing parasitized erythrocytes were purified by magnetic separation by MACS separator with LS columns (Miltenyi Biotech, Germany) and inoculated to CM containing erythrocytes at 2.5% hematocrit. After 6 hours of incubation at 37 °C, sorbitol synchronization was performed to obtain the ring stage parasites (6-hour synchronization window), suspended in 10 mM or 5 mM glucose-containing CM, and incubated at 37 °C for 78-80 hours. The parasite was purified by magnet separation, centrifuged, and suspended in methanol, followed by freezing in liquid nitrogen. The quantification of 116 metabolites and statistical analysis was done by Human Metabolome Technologies (Yagamagata, Japan).

2.4.2 Transcriptome analysis

The tagged PFK9-expressing parasite was purified by magnet separation and inoculated to CM containing erythrocytes at 2.5% hematocrit. After 3 hours of incubation at 37 °C, sorbitol synchronization was performed to obtain the ring stage parasites (3-hour synchronization window), suspended in 20 mM, 10 mM, or 5 mM glucose-containing CM, and incubated at 37 °C for 78 hours. The total RNA was purified with PureLink RNA Mini kit (Thermo Fisher Scientific, USA) and sent to Novogene (Chaoyang District, Beijing, China). Novogene did reverse transcription, sequencing, and mapping to the Pf 3D7 genome, and statistical analysis was performed using a graphical user interface for TCC (TCC-GUI)[147].

2.5 Whole genome prediction of disordered regions in *Pf*

2.5.1 Prediction of disordered regions of proteins

IUPred2A was used for the prediction of disordered regions of a protein[148]. Accession and protein sequences were downloaded from UniProt[149], and IUPred2A analysis and calculation of the disordered fraction of proteins were performed automatically on Anaconda (*Anaconda Software Distribution.* Computer software. Vers. 2-2.4.0. Anaconda, Nov. 2016. Web.). Python code is summarized in the Appendix.

2.5.2 Gene ontology (GO) enrichment analysis

GO enrichment analysis of highly disordered genes was performed with PANTHER Classification System[150]. The Benjamini-Hochberg false discovery rate[151] (FDR) below 0.05 was considered significant and listed in the result section.

Chapter 3

Results

3.1 Disordered proteins bind to nucleic acid in *Pf*

Although many reports demonstrated several functions of LLPS in other organisms, there has been no clear evidence of LLPS or membrane-less organelles in the *Pf* lifecycle. To shed light on how LLPS works in *Pf*, whole-genome prediction of disordered protein was performed. By using IUPred2A, an energy estimation-based predictor of intrinsically disordered protein residues[148], all the 5,311 genes of *Pf* 3D7 on the database were analyzed. Four hundred seventeen genes were determined to be highly disordered proteins, defined as those whose 50% or more residues are predicted to be disordered intrinsically. The GO enrichment analysis revealed that highly disordered proteins may be associated with nucleic acid binding, transcription, and translation regulation (Table 3.1), which was partly similar to the previous result of pan-organism analysis[152]. This result suggested nucleic acid binding may influence the induction of LLPS in the *Pf* lifecycle.

It was reported that not only conventional nucleic acid binding proteins such as transcription factors and polymerases but also some classic metabolic enzymes were RNA binding proteins, and this tendency was conserved from yeast to human[123]. Among them, glycolytic enzymes were attractive targets for studying LLPS in *Pf* because they were perfectly conserved

and should have specific enzyme activity regulation to manage the parasite's complex lifecycle, which highly relies on glycolysis as an energy source.

GO ID	GO Term	*p*-value	FDR
GO:0036002	pre-mRNA binding	4.1×10^{-4}	2.1×10^{-2}
GO:0003700	DNA-binding transcription factor activity	6.5×10^{-11}	3.1×10^{-8}
GO:0140110	transcription regulator activity	6.8×10^{-12}	5.0×10^{-9}
GO:0043565	sequence-specific DNA binding	1.5×10^{-7}	3.6×10^{-5}
GO:0003729	mRNA binding	4.8×10^{-10}	1.8×10^{-7}
GO:0003676	nucleic acid binding	8.9×10^{-5}	5.9×10^{-3}

Table 3.1 GO enrichment analysis of highly disordered genes. Highly disordered genes were analyzed with the GO enrichment analysis tool from the PANTHER classification system. GO terms with positive enrichment and FDR < 0.05 were listed above.

3.2 G-body-like structures formed in *Pf* parasite in low glucose condition

To start with the analysis of LLPS in *Pf* facilitated by glycolytic enzymes, genes with KEGG pathway ec00010 (Glycolysis/Gluconeogenesis) were extracted from PlasmoDB (Table 3.2). Of the selected 29 genes, nine proteins had IDRs according to the IUPred2A analysis, and two of them were conserved 6-phosphofructokinase (PFK), which was investigated the most as a G-body component in other organisms. The result of transcriptome analysis of seven sexual and asexual life stages clearly showed that PFK9 (PF3D7_0915400) was highly expressed in the asexual blood stage, whereas PFK11 (PF3D7_1128300) was only expressed in the sexual stage[153]; therefore, further analyses were done for PFK9 in this study.

Gene ID	Product Description
PF3D7_0310300	phosphoglycerate mutase, putative
PF3D7_0318800	triosephosphate isomerase, putative
PF3D7_0413500	phosphoglucomutase-2
PF3D7_0618500	malate dehydrogenase
PF3D7_0624000	hexokinase
PF3D7_0626800	pyruvate kinase
PF3D7_0627800	acetyl-CoA synthetase, putative
PF3D7_0815900	dihydrolipoyl dehydrogenase, apicoplast
PF3D7_0915400	ATP-dependent 6-phosphofructokinase
PF3D7_0922500	phosphoglycerate kinase
PF3D7_1012500	phosphoglucomutase, putative
PF3D7_1015900	enolase
PF3D7_1020800	dihydrolipoamide acyltransferase component E2
PF3D7_1037100	pyruvate kinase 2
PF3D7_1120100	phosphoglycerate mutase, putative
PF3D7_1124500	pyruvate dehydrogenase E1 component subunit alpha
PF3D7_1128300	ATP-dependent 6-phosphofructokinase
PF3D7_1232200	dihydrolipoyl dehydrogenase, mitochondrial
PF3D7_1238900	protein kinase 2
PF3D7_1324900	L-lactate dehydrogenase
PF3D7_1325200	lactate dehydrogenase, putative
PF3D7_1337800	calcium-dependent protein kinase 5
PF3D7_1342800	phosphoenolpyruvate carboxykinase
PF3D7_1412400	conserved Plasmodium protein, unknown function
PF3D7_1436000	glucose-6-phosphate isomerase
PF3D7_1439900	triosephosphate isomerase
PF3D7_1444800	fructose-bisphosphate aldolase
PF3D7_1446400	pyruvate dehydrogenase E1 component subunit beta
PF3D7_1462800	glyceraldehyde-3-phosphate dehydrogenase

Table 3.2 *Pf* genes predicted to be involved in glycolysis. Twenty nine genes of *Pf* 3D7 were thought to involve in glycolysis/gluconeogenesis according to the KEGG pathway analysis. Proteins with IDRs were highlighted.

To see the formation of G-body in the parasite cell, transgenic parasites expressing fluorescently tagged PFK9 were generated using pKIC-ter plasmid based on a technique named SLI[137]. The advantage of SLI is that a target protein is expressed under an endogenous promoter, which is quite important for LLPS studies affected by the expression level of the target protein. The plasmid had a homologous PFK9 C-terminal sequence followed by Myc tag, mNG[140], skip peptides P2A and T2A[141] tandem sequence, and Neo selection marker. Skip peptides allow separate expression of a tagged target protein and Neo (Figure 3.1a). After transfection, drug selection with WR99210 and G418 was followed by cloning. Diagnostic PCR suggested successfully inserting the plasmid into the parasite genome (Figure 3.1.b). The expression tagged PFK9 was confirmed by Western blotting (Figure 3.1c). However, G-body-like biomolecular condensates were not observed by live imaging of these strains (Figure 3.2), unlike the previous report showing PFK9 droplet-like structures in trophozoite by IFA[154]. Therefore, several stimulations for facilitating G-body formation were tried, such as heat shock, culturing at high parasitemia, and treatment with respiratory chain inhibitors, but none of these conditions could induce G-body-like structure formation. G-body-like structures were only observed when the parasites were cultured for more than 48 hours in a medium with 5 mM glucose (Figure 3.3a,b), corresponding to a fasting blood glucose concentration and half the concentration of the standard culture medium. The area and intensity of G-body-like structures in parasite cells changed in a glucose concentration-dependent manner (Figure 3.3c). In addition, the clustering %, which shows percentage of pixels with a normalized intensity below a threshold, changed when the parasite was cultured in 5 mM glucose containing medium, suggested more clustered PFK9 at low glucose concentration (Figure 3.3d). The G-body-like structure was not observed at even lower glucose concentrations because it led to early cell death possibly due to malfunction of host erythrocytes.

These observations suggested that G-body-like structures were formed through slight but continuous low glucose stress, not acute glucose depletion which does not occur in human body.

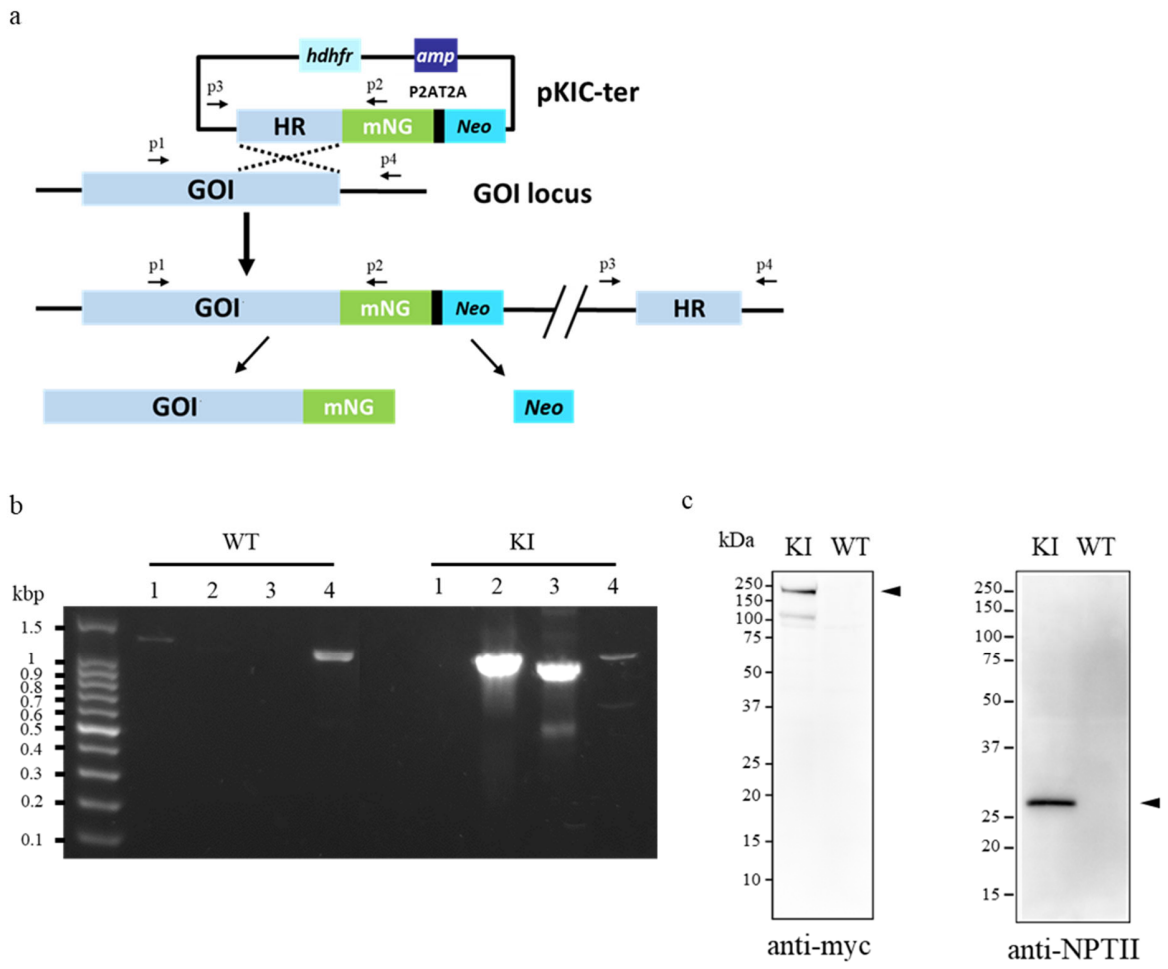

Figure 3.1 Generation of tagged PFK9 expressing parasite. a, Schematics of pKIC-ter plasmid and SLI. The plasmid has a homologous region (HR) of a gene of interest (GOI), following mNeonGreen (mNG), tandem skip peptides P2A-T2A, and Neomycin-kanamycin phosphotransferase II (Neo), which shows G418 resistant only when inserted into the parasite genome. The skip peptides induce ribosomal skipping during translation, which allows separate expression of mNG-tagged GOI and Neo proteins. **b,** The result of diagnostic PCR for wild type (WT) and knock-in (KI) with different primer sets. Lane 1: p1 + p2, Lane 2: p3 + p4, Lane 3: p2 + p3, Lane 4: p1 + p4. **c,** C-terminal tagging of PFK9 in *Pf* 3D7 parasite was confirmed by anti-Myc and anti-NPTII Western blotting. The 2.5 X 10^7 parasite /lane lysate was applied each for WT and KI strains. The PFK9-Myc-mNG 190 kDa band and NPTII 29.1 kDa band were only seen in KI samples, showing successful C-terminal tagging of PFK9.

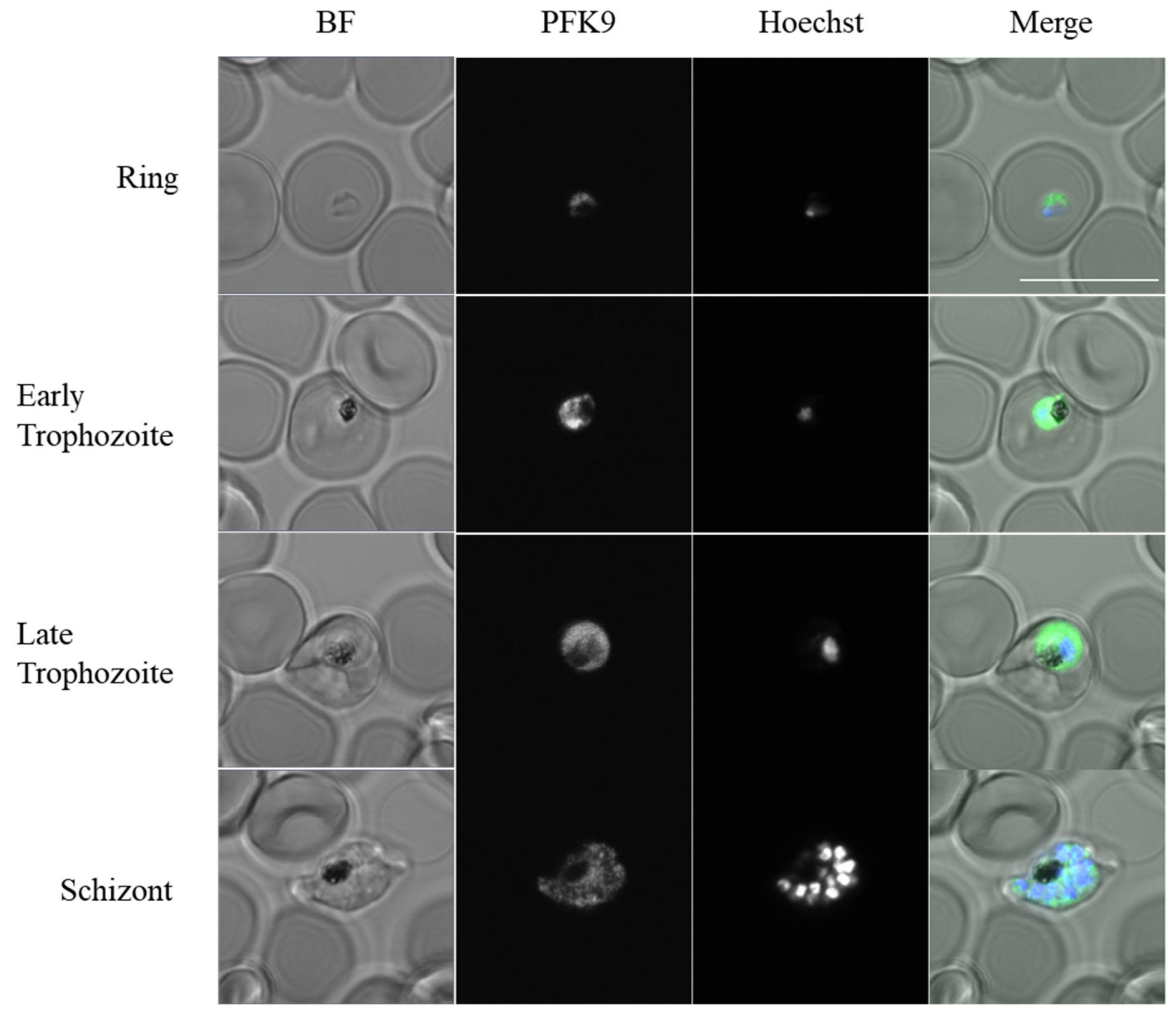

Figure 3.2 Live imaging of the tagged PFK9 expressing parasite. PFK9 was uniformly expressed in cytoplasm of the parasite throughout the asexual blood stage. G-body-like structure was not observed in the steady state. Scale bar represents 10 µm.

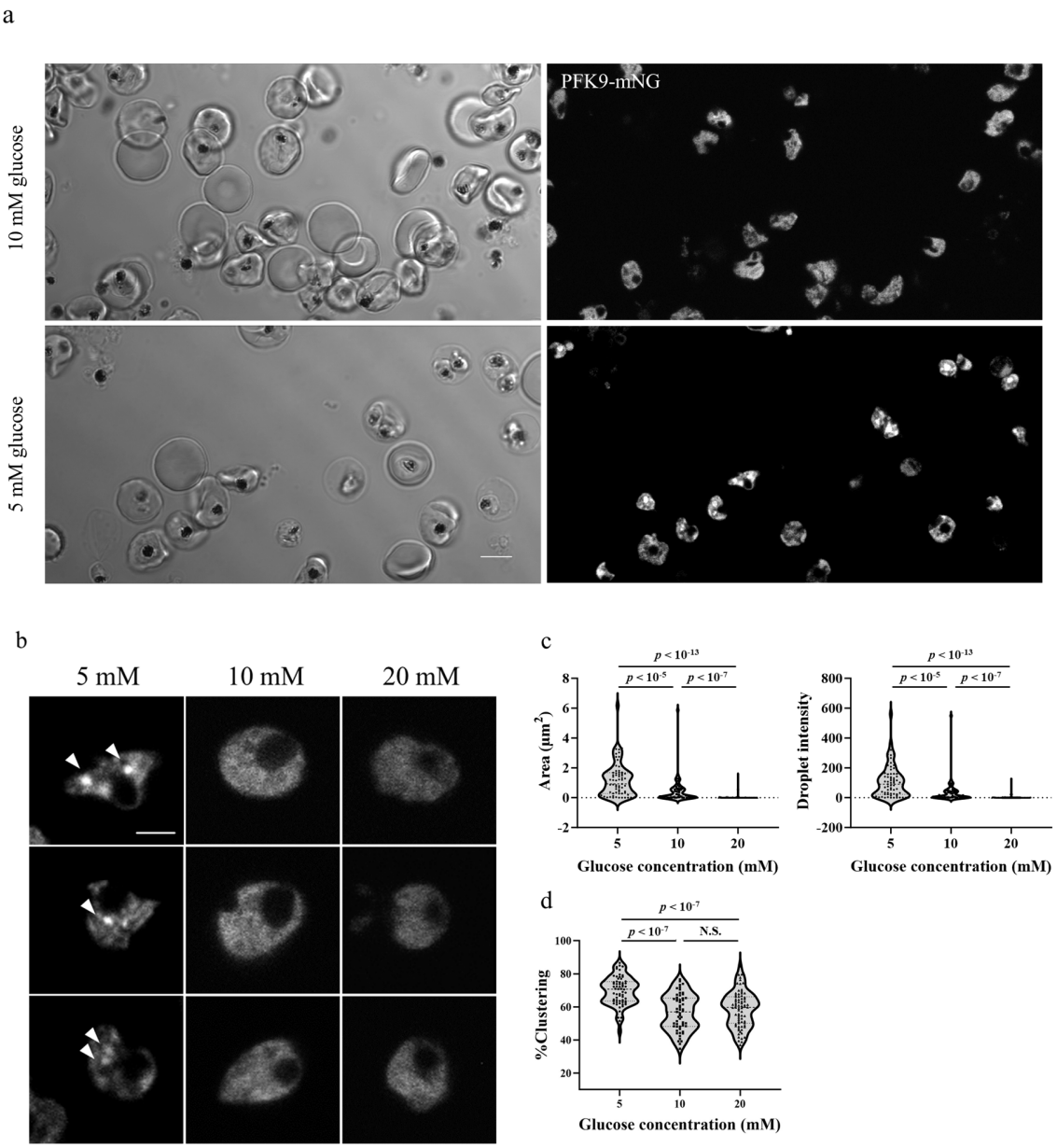

Figure 3.3 G-body-like structures formed in the *Pf* parasite on low glucose condition. a, Live imaging of the tagged PFK9 expressing parasite in culture medium containing glucose at indicated concentration. Scale bar represents 5 μm. **b,** Magnified version of the tagged PFK9 expressing parasite cultured in different glucose condition. G-body-like structures with condensed PFK9 were seen in 5 mM glucose culture, as arrowheads indicate. Scale bar represents 2 μm. **c, d,** Area, Droplet intensity, and Clustering % of PFK9-mNG fluorescence at different glucose concentration indicated the clustering of PFK9 in a glucose concentration dependent manner. n = 67 (5 mM), 53 (10 mM), and 59 (20 mM). *p* values were calculated by Kruskal-Wallis and Steel-Dwass post hoc test.

3.3 Phosphoglycerate kinase (PGK) also formed G-body-like structures in low glucose conditions

To see if the G-body-like structure formation also occurs for other glycolytic enzymes, several transgenic parasites expressing mNG-tagged glycolytic enzymes were generated using the SLI. Of the nine glycolytic enzymes except PFK9, six enzymes were successfully tagged and confirmed the expression of tagged proteins (Figure 3.4a, b). However, fructose-bisphosphate aldolase (FBPA, PF3D7_1444800), glyceraldehyde-3-phosphate dehydrogenase (GAPDH, PF3D7_1462800), and enolase (ENO, PF3D7_1015900) did not come back after drug selection, due to possible toxic effects against parasites by C-terminus tagging of these genes. Obtained transgenic parasites were cultured in low glucose conditions for 80h, and only PGK (PF3D7_0922500) formed similar G-body-like structures (Figure 3.5a). This result suggested the possibility of multi-enzymatic G-body-like structure formation under low glucose conditions to overcome the low glucose stress. In addition, it indicated that these structures were formed by specific enzymes rather than stress-induced non-specific aggregation of the parasite cytosol.

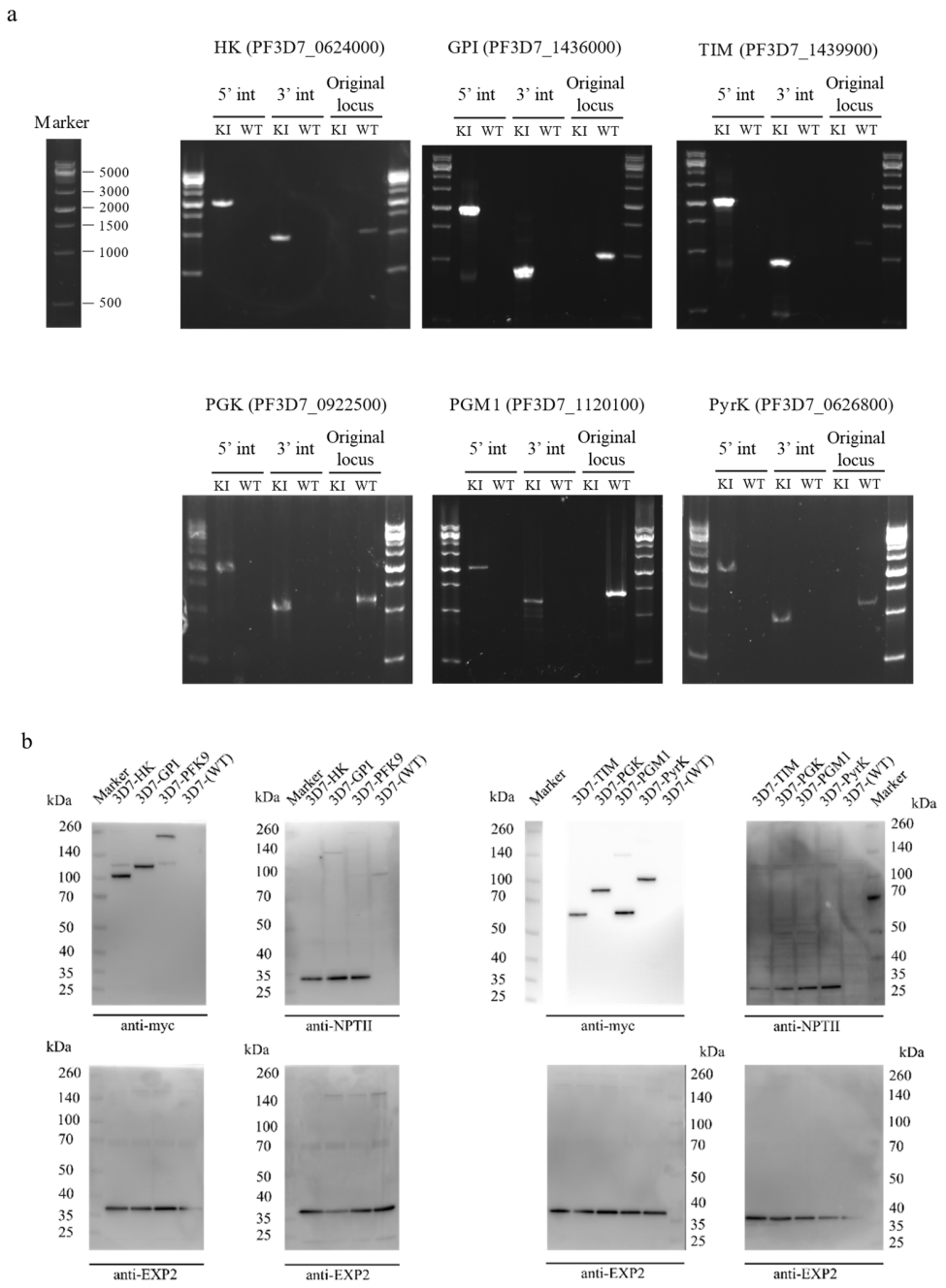

Figure 3.4 Generation of tagged glycolytic enzymes expressing parasites. a, The result of diagnostic PCR for wild type (WT) and knock-in (KI) with different primer sets. **b,** C-terminal tagging of glycolytic enzymes in *Pf* 3D7 parasite was confirmed by anti-Myc and anti-NPTII Western blotting. The 5 X 10^6 parasite /lane lysate was applied. Estimated protein size; HK-mNG-myc:89.4 kDa, GPI-mNG-myc:101.5 kDa, PFK9-mNG-myc:193.6 kDa, TIM-mNG-myc:62.0 kDa, PGK-mNG-myc:79.5 kDa, PGM1-mNG-myc:62.9 kDa, PyrK-mNG-myc:89.8 kDa, NPTII:29 kDa, EXP2:33.4 kDa.

a

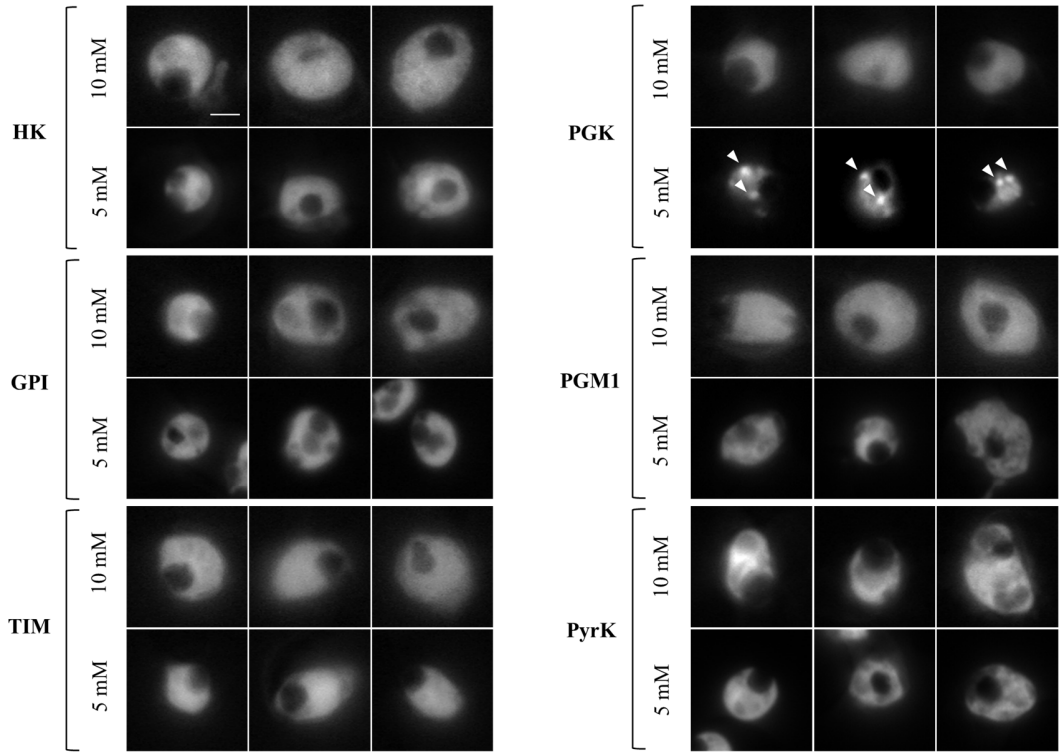

b

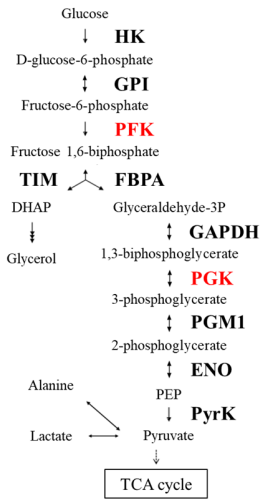

Figure 3.5 G-body-like structures formed in the *Pf* parasite on low glucose condition.

a, Representative live images of the parasites expressing tagged glycolytic enzymes cultured in different glucose concentrations for 80h. Only PGK formed condensates in 5 mM glucose culture, as arrowheads indicate. Scale bar represents 2 μm. **b,** Schematics of glycolysis of *Pf* parasite. PFK and PGK were the only proteins confirmed to form condesates in low glucose conditions.

3.4 Omics analyses revealed possible G-body-related genes

Previous studies suggested that the G-body formation influenced metabolic conditions since it accelerated glycolysis and acted like a hub of cellular processes that contained proteins with several functions[155]. In addition, it was demonstrated that the Snf1 signaling pathway was necessary for G-body formation in yeast[155]. Therefore, it was hypothesized that G-body-like structure formation might also influence other cellular processes in the parasite, and omics analyses could clarify these processes and mechanisms of G-body-like structure formation. Firstly, metabolome analysis was conducted to compare metabolic changes of the parasite cultured in 5 mM or 10 mM glucose-containing medium for 78-80 h. As a result, fumarate and ɤ-aminobutyric acid (GABA) were decreased, and citrulline was increased significantly in the parasite cultured in the low-glucose medium (Figure 3.6, Table A.2). However, any metabolites related to glycolysis or other energy metabolisms did not change, suggesting that the parasite has some measures to compensate for the limited access to glucose and maintain the level of glycolysis. Subsequently, transcriptome analysis was performed similarly for the parasite cultured in 5 mM, 10 mM, or 20 mM glucose-containing media for 78 h. The parasite cultured in the low-glucose medium showed quite different transcriptome patterns from others, and 1,706 genes were identified as differentially expressed genes (DEGs) (Figure 3.7). Interestingly, the expression level of PFK9 in the low glucose condition was indistinguishable between the standard and low glucose conditions, suggesting that the glycolysis level under the low glucose condition can be maintained by G-body-like structure formation rather than the increase of glycolytic enzymes.

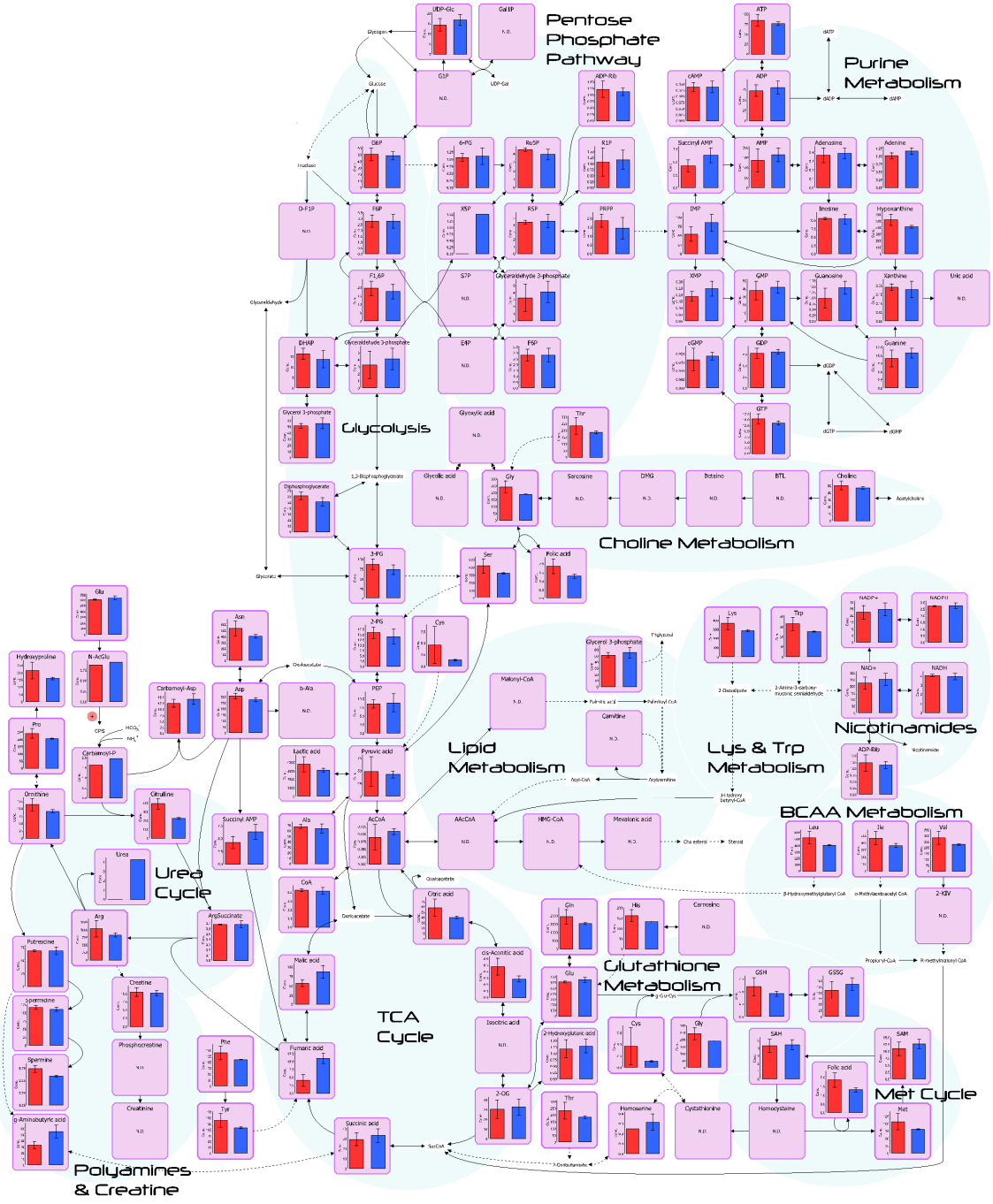

Figure 3.6 Formation of G-body-like structures did not change metabolic profiles of the parasite. The tagged PFK9 expressing parasite was cultured in 5 mM (red) or 10 mM (blue) glucose for 78-80 hours, and 116 metabolites were measured in triplicate. The absolute values and comparative analysis of the metabolites are summarized in Table A.2.

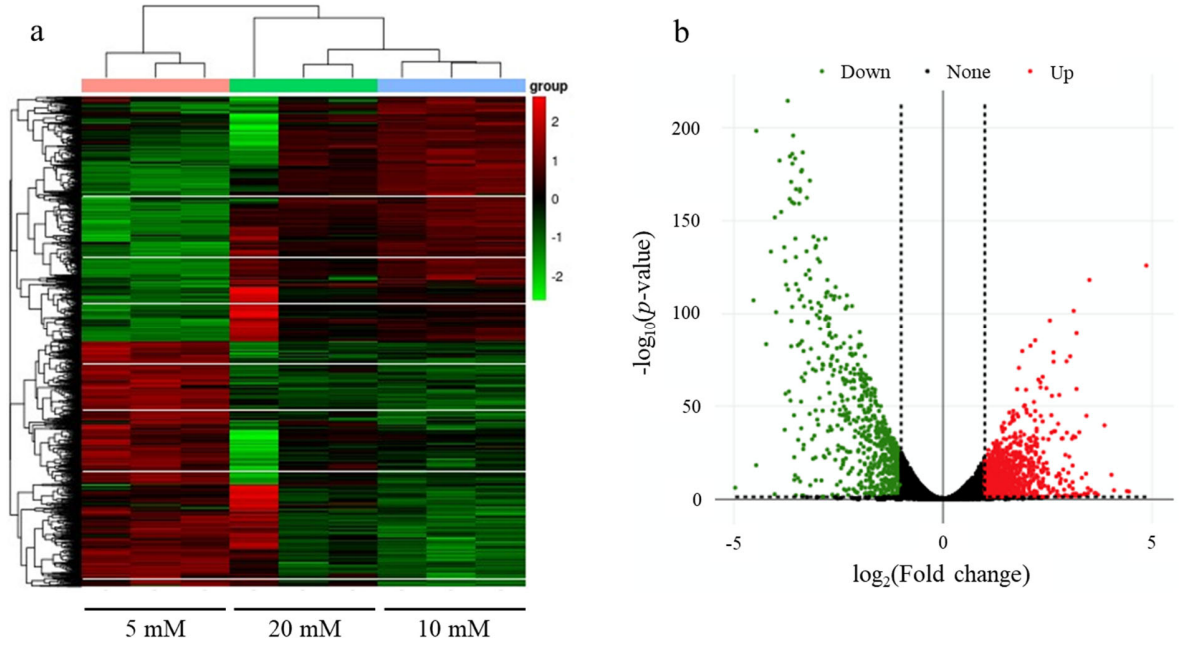

Figure 3.7 Transcriptome analysis of the parasite culture in different glucose concentration.
a, Heatmap comparison of the tagged PFK9 expressing parasite cultured in the medium with different glucose concentrations. The parasite cultured in 5 mM glucose showed different expression patterns. **b,** Volcano plot showing differential expression of the parasite genes between 5 mM glucose and 10 mM glucose culture condition.

3.5 Lipid membrane staining suggested the membrane-less formation of G-body-like structures

FRAP analysis was performed first to understand the physical properties of G-body-like structures in the parasite cell. However, it did not result in consistent fluorescence recovery of PFK9, possibly due to the size or low fluidity of G-body-like structures (data not shown). Furthermore, large G-body-like structures were stable and not fused with other PFK9 condensates for at least 30 min (Figure 3.8a). These observations suggested that G-body-like structures were membranous; therefore, membrane staining was conducted instead using Di-4-ANEPPDHQ, a dye that shows fluorescence only when bound to the phospholipid membrane[156]. The result showed that G-body-like structures were not stained with Di-4-ANEPPDHQ, whereas the parasite membranes showed fluorescence, demonstrating the possibility that G-body-like structures are likely membrane-less organizations formed through LLPS (Figure 3.8b).

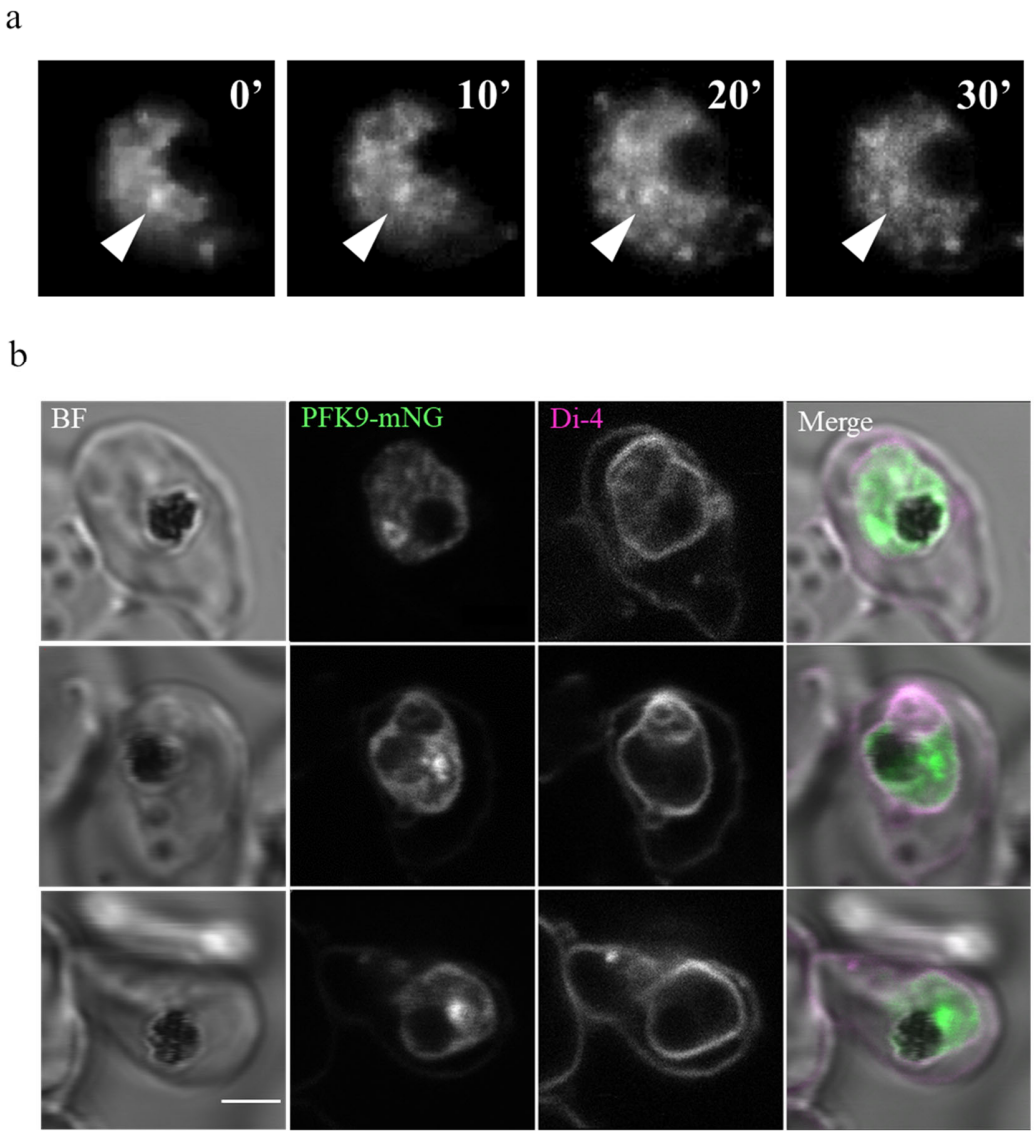

Figure 3.8 G-body-like structures were not stained with a membrane dye. a, Time-lapse images of the tagged PFK9 expressing parasite for 30 min. Arrow heads show a representative stable G-body-like structure. **b,** The tagged PFK9 expressing parasite was cultured in low glucose medium and stained with a membrane probe Di-4-ANEPPDHQ for 30 min. The parasite plasma membrane and some of inner membranes showed fluorescence, whereas G-body-like structures were not stained with the dye. Scale bar represents 2 μm.

3.6 Osmotic stress formed transient G-body-like structures

Recent studies have shown that hyperosmotic stress can cause LLPS to several proteins because it compresses cell volume and increases protein concentration and macromolecular crowding[157]. In addition, it was demonstrated that local concentration of PFK was the key determinant of G-body formation in *Caenorhabditis elegans*[125]. To see if higher PFK9 concentration leads to the formation of G-body-like structures in the parasite, hyperosmotic stress was induced to the tagged PFK9 expressing *Pf* by adding sodium chloride to the medium. The stress should have caused the shrinkage of the parasite cells, but there was no significant difference in the measured cell area. However, the non-homogeneous formation of G-body-like structures was observed rapidly within five min (Figure 3.9a). Furthermore, unlike the stable G-body-like structures formed through low glucose culture, these structures dissolved right after the hyperosmotic stress was removed (Figure 3.9b). Hyperosmotic stress also causes several cellular responses, such as DNA damage, mitochondrial depolarization, and stress granule formation; however, they are usually seen after longer exposure to the stress. These observations suggested that an increase of local PFK9 concentration and macromolecular crowding could induce G-body-like structure formation in the parasite, and post-translational modification, such as phosphorylation seen in yeast PFK, may not be necessary for the condensation of PFK9 in *Pf*.

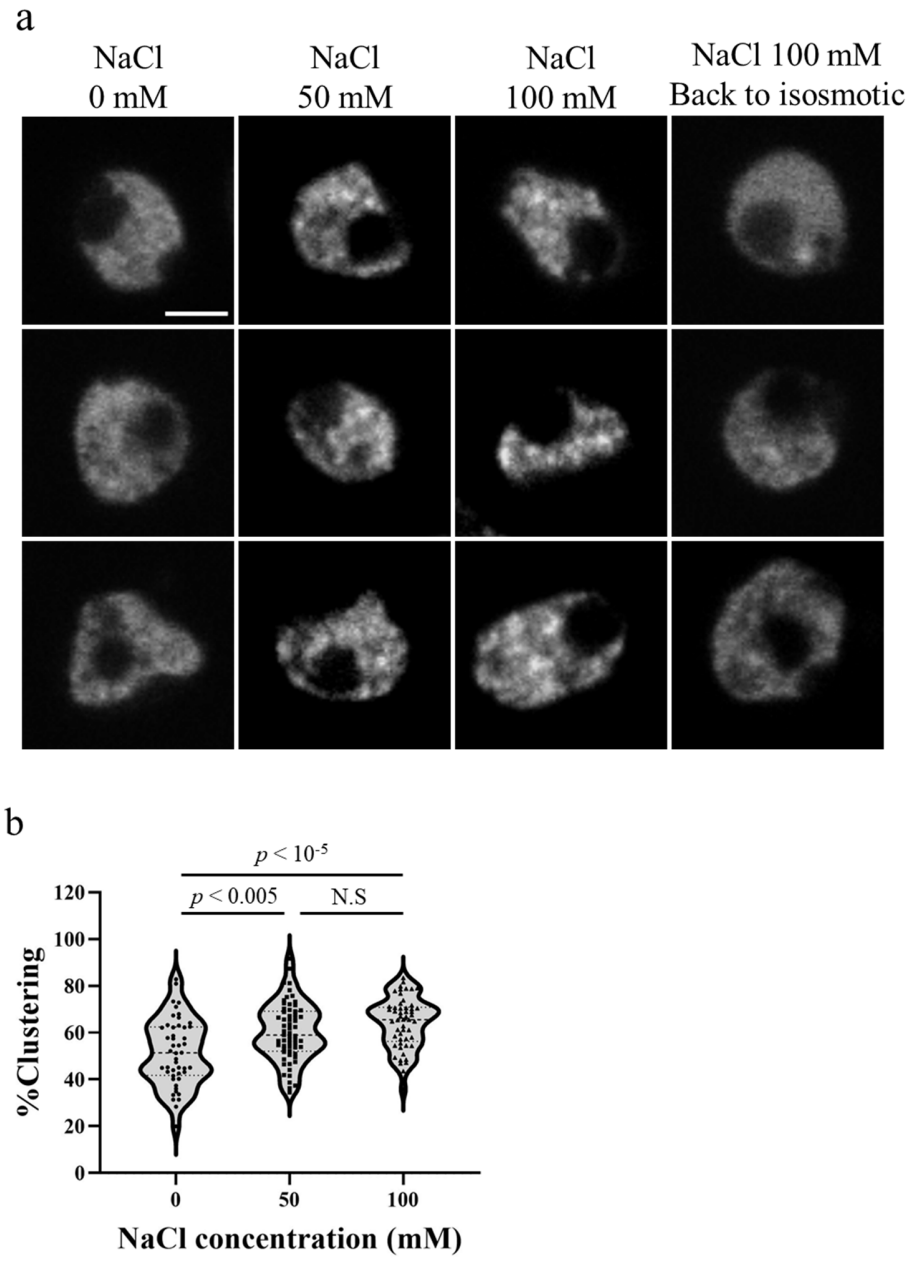

Figure 3.9 Osmotic stress induced transient G-body-like structure formation. a, Live imaging of tagged PFK9 expressing parasite suspended in CM with indicated NaCl concentration. PFK9 clusters were seen in the parasite cytosol and disappeared when it was back to isosmotic. Scale bar represents 2 µm. **b,** Clustering % of tagged PFK9 expressing parasite in CM with different NaCl concentration indicated the clustering of PFK9 under osmotic stress. n = 48 (0 mM), 63 (50 mM), and 53 (100 mM). *p* values were calculated by Kruskal-Wallis and Steel-Dwass post hoc test.

3.7 TIRF imaging revealed small PFK9 cluster formation in low glucose condition

Although we could successfully observe G-body-like structures in low glucose culture, the formation of tagged PFK9 condensates did not always occur on a fixed condition, possibly due to differences in conditions of host cells caused by daily maintenance of cell culture. In addition, G-body-like structures were quite stable and irreversible under isotonic conditions, as shown in Figure 3.8a, indicating more rigid physical properties compared to G-bodies in other organisms. It was demonstrated that G-bodies hardened along with time[125], but no growing or maturing G-body-like structures were observed in the parasite. These observations suggested a hypothesis that smaller clusters of PFK9, invisible in the standard microscopic observation, were formed after low glucose stress, and the tagged PFK9 condensates observed were the final ripen form of G-bodies, probably just before severe cellular damage. Since PFK9 is highly expressed throughout the asexual blood stage of the parasite, the fluorescence of tagged PFK9 from outside the focal plane was thought to affect and give indistinct images even when using confocal microscopy. To obtain images with a higher signal-to-noise ratio, TIRF imaging was performed for the parasite without G-body-like structures after a 72-hour low glucose culture. TIRF is a technique that could detect fluorescence of tagged PFK9 existing within 128.4 nm from the coverslip in our setting. TIRF provided images with uneven distribution of PFK9, especially in a low glucose condition (Figure 3.10a). To see if the low glucose culture induces PFK9 cluster formation, the intensity profile of line plots was analyzed by fluorescence fluctuation frequency analysis. To clarify the difference in cluster formation, a power spectrum plot of low glucose cultured *Pf* was compared to that of standard cultured parasites[158] (Figure 3.10b). Low glucose cultured parasite showed a steeper slope

of the plot due to higher power values at lower frequencies, implying the existence of bigger PFK9 clusters at least after 6h of low glucose culture (Figure 3.10c). Furthermore, autocorrelation analysis was applied to TIRF images to elucidate the size of PFK9 clusters. It was demonstrated by Hwang *et al.* that two-dimensional spatial autocorrelation analysis could deduce the sizes of protein domains[146], and we expanded to estimate the protein cluster sizes of *Pf*-infected erythrocytes[158]. For the angle-averaged autocorrelation, the functions for both standard cultured and low glucose cultured parasites were fit for a single peak Gaussian, and cluster sizes were estimated from FWHM (Figure 3.10d and Table 3.3). The result implied that larger PFK9 clusters existed in low glucose culture parasites, even though the estimated sizes were bigger than expected, possibly due to the pixel size of the images (100 nm/pixel).

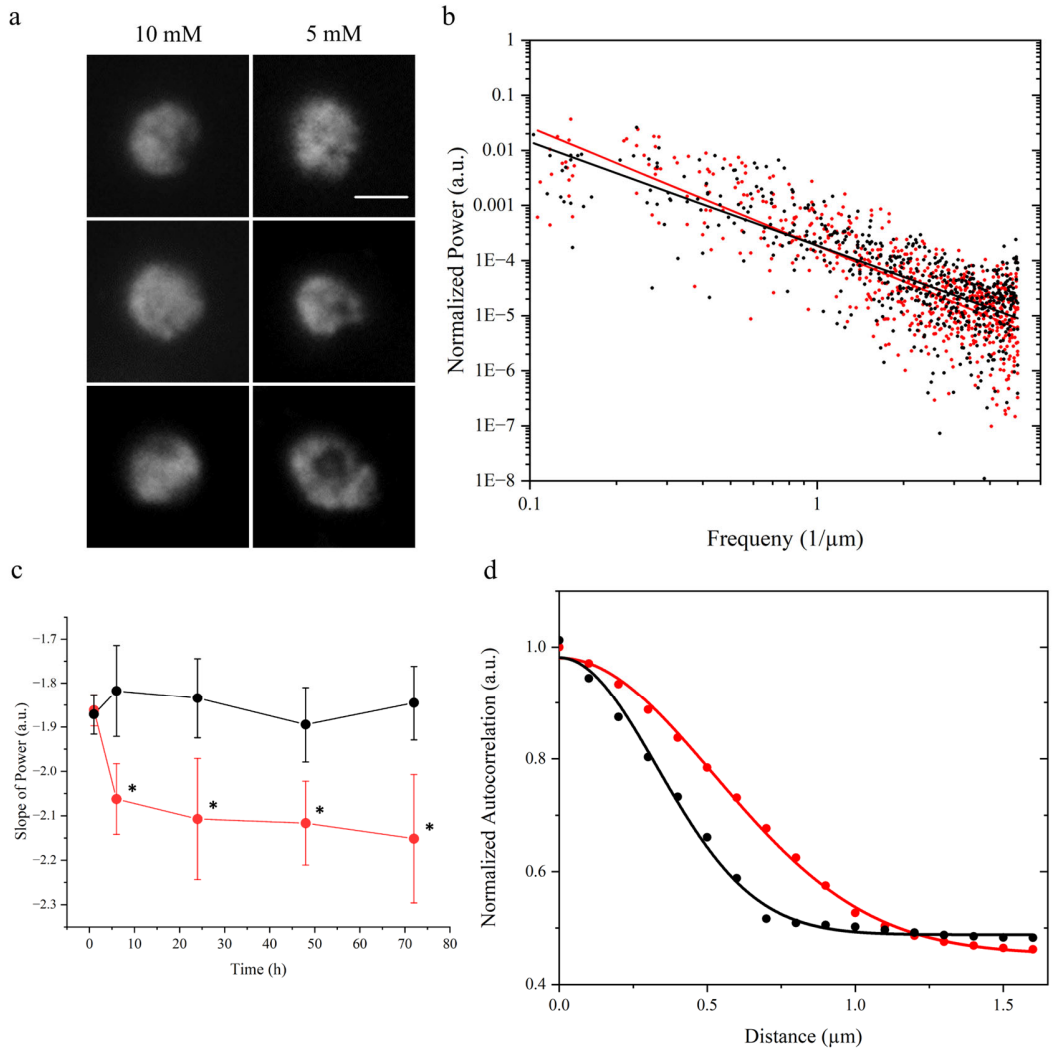

Figure 3.10 TIRF image analysis suggested the existence of larger PFK9 clusters in low glucose conditions. a, Representative TIRF images of *Pf* cultured in 10 mM or 5 mM glucose containing medium for 72 hours. Tagged PFK9 distributed more non-homogeneously than confocal images. Scale bar represents 2 μm. **b,** Double logarithmic plots of power spectra from line plots of tagged PFK9 expressing parasite cultured in 10 mM (black) and 5 mM (red) glucose containing medium for 72h. The graph shows cumulative data from three different experiments, which analyzed six cells each and more than three line plots per cell. **c,** The slope values of power spectra regression lines from three different experiments suggested larger PFK9 cluster existences after 6h of low glucose culture. The *p*-value was calculated using a Student's t-test. Error bars represent the standard deviation of the mean. **p*<0.05. **d,** 2D-autocorrelation analysis of representative PFK9 fluorescence of the parasite cultured in 10 mM (black) and 5 mM (red) glucose containing medium for 72h also suggested larger PFK9 clusters in low glucose conditions.

Glucose concentration	Cluster size (nm)	R^2
10 mM	$773 \pm 100^*$	0.993
5 mM	$1226 \pm 100^*$	0.998

Table 3.3 Analytical results of autocorrelation analysis. The autocorrelation function of representative PFK9 fluorescence showed good fit in single Gaussian, and estimated cluster sizes of low glucose cultured parasite were larger than that of the parasite cultured in normal glucose conditions. *The fitting errors were smaller than the pixel size of 100 nm.

Chapter 4

Discussion

4.1 Protein disorder prediction and possible LLPS functions in *Pf*

It has been almost 15 years since the function of biomolecular condensates in cells was first reported, and mechanisms of several known cellular processes and novel phenomena have been explained well by understanding the LLPS of biomolecules. However, LLPS of *Plasmodium* parasites have not been reported, probably because of the small cell sizes and difficulties in genetic modifications. This study started to elucidate LLPS functions in the *Pf* lifecycle, which should be regulated by LLPS considering its requirements for fast and accurate gene expression and metabolic changes in a short period.

To hypothesize how LLPS works in *Pf*, the GO term analysis of disordered *Pf* proteins was first performed. The result suggested that nucleic acid binding proteins were highly disordered and possible facilitators of LLPS in *Pf*, the same as reported in other organisms. Regarding the GO terms of cellular components, chromatin and heterochromatin were significantly enriched in highly disordered proteins, suggesting that LLPS may control gene expression in the parasite. Given that several Apetela2 (AP2) family transcription factors had heterochromatin as their GO terms and many of them were disordered proteins, the parasite may utilize LLPS for controlling AP2 protein-based transcription regulation, which is essential for the parasite lifecycle[159].

Even though there was an argument that disordered regions were not diagnostic of LLPS of a protein but were multivalency of protein regions[160], enrichment of disordered regions in biomolecular condensates suggested that the result of this study could be a good predictor of LLPS functions in *Pf* as a starting point.

4.2 Possible components of G-body-like structures

Among nucleic acid binding proteins, PFK9 became the primary target of this study since 1) glycolysis is one of the most important processes of the *Pf* lifecycle, 2) it was the most investigated protein of G-body components, 3) PfPFK9 also has disordered regions which were required for G-body formation in yeast. It was unexpected that fluorescently tagged PFK9 did not form G-bodies, probably because the parasite was already in a hypoxic condition in a steady state[161], and the function of G-bodies in *Pf* differed from that of other organisms. In addition, it should be noted that RPMI 1640-based standard culture medium provides a higher growth rate than human serum due to supraphysiological nutrient levels[162,163], and the metabolic condition of the cultured parasite and the need for G-bodies might differ from that of the *in vivo* parasite. This perspective led to the successful observation of G-body-like structures in fasted blood sugar level conditions.

To clarify the components of G-body-like structures, plasmids were constructed and transfected to the parasite to fluorescently tag all the rest of the nine glycolytic enzymes, the same as PFK9. Plasmid-positive parasites were obtained for all nine strains; however, FBPA, GAPDH, and ENO-tagged parasites did not return after drug selection for the parasites with integrated plasmid sequence. The crystal structure analyses of the parasite's FBPA and GAPDH suggested

that their working unit were homodimer and homotetramer, respectively[164,165]. In addition, the result of recombinant PfENO purification indicated that it formed a homodimer[166]; therefore, the C-terminal tagging of these proteins may have disrupted the multimer formations and resulted in the parasite's cell death. The N-terminal tagging of the three genes using the CRISPR-Cas9 system may lead to successful results.

Long-term low glucose culture results for the seven glycolytic enzyme-tagged parasites suggested that PGK and PFK9 were the only components of the G-body-like structures. Moreover, this experiment clarified that G-body-like structures consisted of specific proteins and were not formed through non-specific aggregations of cytosolic proteins. Crystal structure analysis of PGK demonstrated that it did not have a disordered region[167], suggesting that PFK9 may be the scaffold of G-body-like structures. Consistent with this, purified disorder regions of PFK9 with or without GFP tag aggregated even at low concentrations (< 2 μM), suggesting strong intermolecular or intramolecular interactions of PFK9 protein (Figure A.1). From the functional aspect, PFK9 and PGK both utilize ATP and ADP for their reactions. Considering that ATP can act as a hydrotrope in cells[168], PFK9 and PGK interactions and formation of G-body-like structure are regulated by ATP levels of the parasite cell, which is reasonable for the feedback process of primary ATP source.

4.3 Interpretation of omics analyses results

The result of the metabolome analysis suggested no significant changes in glycolysis after the long duration of low glucose culture; however, a decrease in GABA and fumarate indicated metabolic changes in the parasite. It was demonstrated that the parasite could produce GABA directly from glutamate catalyzed by glutamate decarboxylase (GAD) in the cytosol[169]. In addition,

GABA may also be a product of GABA transaminase (GABA-T), which catalyzes the conversion of glutamate to α-ketoglutarate incorporated into the TCA cycle[169]. However, inconsistent with the result of the metabolome analysis, the expression levels of GAD and GABA-T were increased after a low glucose culture in the transcriptome analysis. Considering that glutamate did not decrease after a low glucose culture, these results may suggest that the GABA-T reaction was inhibited due to impairment of the TCA cycle. Consistent with this, it was reported that isolated *Pf* mitochondria could utilize fumarate via reverse reaction of respiratory chain complex II, which was required for mitochondrial respiration initiated by dihydroorotate[170]. With these facts, it was hypothesized that low glucose stress facilitated mitochondrial respiration and ATP production through a reverse reaction of complex II consuming fumarate, resulting in impairment of the TCA cycle and decreased GABA production. The change in metabolic fluxes needs to be elucidated by analysis using isotope-labeled glutamine.

The result of transcriptome analysis indicated that most DEGs were derived from developmental stage differences of the low glucose cultured parasite. However, transcriptome data from previous literature[171,172] allowed the identification of five G-body-related genes that were clearly upregulated by low glucose culture (Table A.4). Overexpression experiments of the five G-body-related genes were designed to understand how the candidate genes work in G-body formation (Figure A.2a). However, gene 1 and gene 4 experienced difficulties in amplifying the whole length from the parasite genome, possibly due to their genomic lengths (> 8 kb) and AT-rich sequences (79% and 81%, respectively). Therefore, gene 2, gene 3, and gene 5 were amplified from the genome and cloned into the pUF-OE vector. After transfection and drug selection, the expression of GOI in the re-emerged parasite was confirmed by Western blotting and IFA (Figure A.2b-e). There was no clear upregulation in G-body-like structure formation in the three

overexpression strains in 10 mM and 5 mM glucose conditions, suggesting that these genes were not the sole inducers of PFK9 cluster formation. However, the possible toxicity of gene 3 expression made the analysis difficult, and further investigation using a moderate expression system would be required to conclude its contribution to G-body formation.

CRISPR-Cas9-based gene knockout of the tagged PFK9-expressing parasite was also performed to clarify the functions of candidate genes in G-body formation. As shown in Figure A.4, plasmids for Cas9 and sgRNA expression with or without linear donor DNA were transfected to the parasite to knock out the genes of interest. As a result, gene 2, 3, and 5 were successfully knocked out, and the following limiting dilution allowed obtaining two transgenic parasite clones each (Figure A.3b, d). The knockout strains showed comparable growth rates to the parental strain, even in 5 mM glucose conditions. Moreover, the formation of G-body-like structures was observed in the low glucose condition (Figure A.4), suggesting that they were not essential components of the G-body-like structure.

While the result of osmotic stress suggested that the local high concentration of PFK9 could induce G-body-like structure formation, the transcriptome analysis showed no increase in PFK9 expression after a low glucose culture. Of the ten glycolytic enzymes, glucose-6-phosphate isomerase (GPI) and pyruvate kinase (PK) expression levels increased about twice, and others showed almost the same expression levels. Overexpression of GPI and PK may contributed to the formation of G-body-like structures.

4.4 Models and possible functions of G-body-like structures

The results of membrane staining and osmotic stress suggested membrane-less condensation of PFK9 into G-body-like structures. Interestingly, unlike those formed after long-term low glucose culture, osmotic stress-induced G-body-like structures were reversible. This result indicated two key features: 1) G-body-like structures are reversible first, and crossing over the 'critical local concentration' induce irreversible form of G-body-like structures. Since LLPS is essentially dependent on concentration, the existence of critical local concentration strongly supports the idea that G-body-like structures were formed through LLPS of PFK9. The trigger of G-body-like structure formation was not clarified in this study. However, considering that the PFK9 expression level did not change even after long-term low glucose culture, there should be some machinery for increasing local PFK9 interaction and concentration, such as post-translational modifications or an increase of other cluster-facilitating proteins (Figure 4.1a). Another possibility of PFK9 clustering facilitator is non-protein scaffold molecules such as RNA. It was reported that long noncoding RNA could assemble a metabolon of several glycolytic enzymes to overcome metabolic stress[173], and a similar phenomenon may occur in the parasite cytosol. Fusing RNase to the C-terminus of PFK9 may be able to show the importance of RNA in G-body-like structure formation, the same as performed in yeast[122].

Another limitation of this study was the lack of direct observations of liquid-like behaviors in PFK9 condensates due to technical difficulties in FRAP analysis and observing the fusion of G-body-like structures. Further investigations should be required to confirm the LLPS of PFK9 using other methods, such as observation using photoactivation localization microscopy (PALM) or lattice light sheet microscopy for confirming the fusion of PFK9 clusters[174].

Although the existence of small reversible G-body structures was hypothesized, it was unable to see those structures using standard microscopy. TIRF imaging provided images with a heterogeneous distribution of PFK9 even when the G-body-like structure was not seen in conventional confocal microscopy, and it also showed a fast movement of PFK9 within the parasite cytosol. The fast mixing (<130 msec) of PFK9 clusters may be one of the reasons why conventional confocal microscopy showed homogeneous PFK9 distribution since slow scanning speed and image averaging made its acquisition time longer than 10 seconds. Since confocal and epi-fluorescence microscopy have limitations for their optical resolution and structures less than 300-500 nm in diameter cannot be distinguished, the autocorrelation analysis helped to recognize the existence of larger PFK9 clusters in the parasite after low glucose culture. Time course TIRF analysis of low glucose cultured parasite suggested that small G-body-like structures were formed within 6h. Considering that 5 mM glucose corresponds to fasting blood sugar level, this result indicated that parasites utilize G-body-like structures for adapting blood sugar level oscillation in the human body (Figure 4.1b). The activity of the primary energy source may be finely regulated by LLPS of glycolytic enzymes to adjust the nutritional condition of the host, which may differ significantly after an increase in the parasite load[175].

The absence of functional analysis of G-body-like structures is a major limitation of this study, mainly due to no parasite growth inhibition in a medium containing 5 mM glucose. More studies will be needed to clarify the significance and essentiality of PFK9 clustering by measuring glycolytic activities and growth rates in physiological conditions. In addition, components of G-body-like structures need to be elucidated to show why the enzyme clusters benefit the parasite. Pull down of G-body-like structures or tagging of proteins in the proximity of PFK9, following mass spectrometry analysis will be needed.

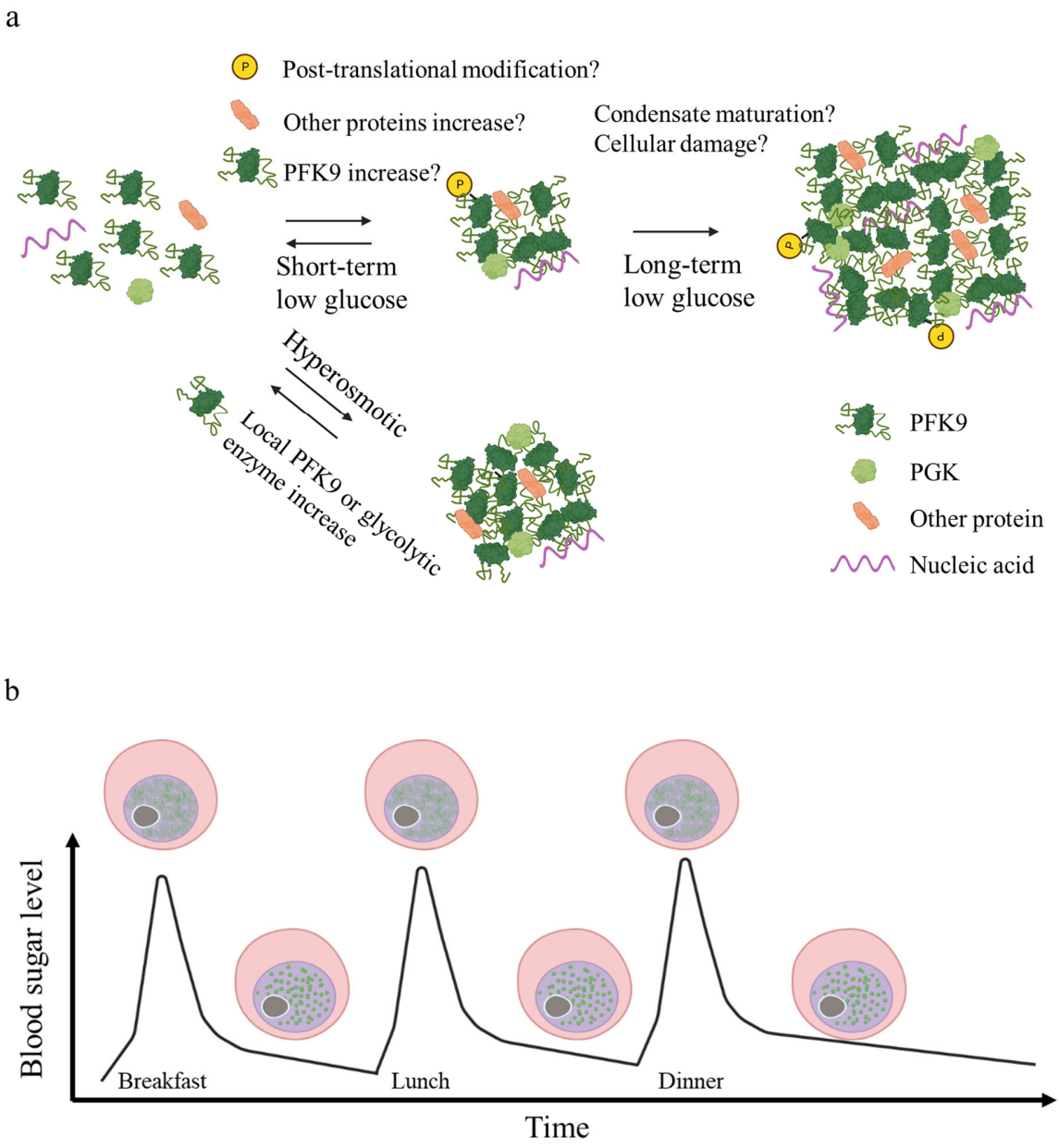

Figure 4.1 Possible models for G-body-like structure formation. a, Reversible small G-body-like structures are formed after short-term low glucose culture and mature into irreversible large structures after long-term culture. Triggers of these clustering need to be elucidateed. Hyperosmotic stress results in reversible medium size G-body-like structure formation, possibly due to rapid increase of the local PFK9 concentration. **b,** Schematics of the G-body-like structure formation along with oscillation of human blood sugar level. The parasite may change glycolytic activity by formation of the structures to adapt the environmental differences.

Disclaimers:

The authors have no financial conflicts of interest to disclose concerning the study.

Disclaimer by Dr. Jeeseong Hwang: “My supervision of Dr. Ishii towards his thesis is based on my personal evaluation, not to be interpreted in any way as an endorsement by the National Institute of Standards and Technology.”

References

1 World Health Organization. *World malaria report 2023*. (2023).

2 Bohórquez, E. B., Chua, M. & Meshnick, S. R. Quinine localizes to a non-acidic compartment within the food vacuole of the malaria parasite Plasmodium falciparum. *Malaria Journal* **11**, 350 (2012).

3 Legrand, E., Volney, B., Meynard, J.-B., Mercereau-Puijalon, O. & Esterre, P. In Vitro Monitoring of *Plasmodium falciparum* Drug Resistance in French Guiana: a Synopsis of Continuous Assessment from 1994 to 2005. *Antimicrobial Agents and Chemotherapy* **52**, 288-298 (2008).

4 World Health Organization. *WHO Guidelines for malaria*. (2023).

5 Plantone, D. & Koudriavtseva, T. Current and Future Use of Chloroquine and Hydroxychloroquine in Infectious, Immune, Neoplastic, and Neurological Diseases: A Mini-Review. *Clinical Drug Investigation* **38**, 653-671 (2018).

6 Zhou, W. *et al.* Chloroquine against malaria, cancers and viral diseases. *Drug Discov Today* **25**, 2012-2022 (2020).

7 Fidock, D. A. *et al.* Mutations in the P. falciparum Digestive Vacuole Transmembrane Protein PfCRT and Evidence for Their Role in Chloroquine Resistance. *Molecular Cell* **6**, 861-871 (2000).

8 Wootton, J. C. *et al.* Genetic diversity and chloroquine selective sweeps in Plasmodium falciparum. *Nature* **418**, 320-323 (2002).

9 Manguin, S. *Biodiversity of malaria in the world : English version completely updated*. (John Libbey Eurotext, 2008).

10 Gutman, J., Kachur, S. P., Slutsker, L., Nzila, A. & Mutabingwa, T. Combination of probenecid-sulphadoxine-pyrimethamine for intermittent preventive treatment in pregnancy. *Malar J* **11**, 39 (2012).

11 Sibley, C. H. *et al.* Pyrimethamine–sulfadoxine resistance in Plasmodium falciparum: what next? *Trends in Parasitology* **17**, 582-588 (2001).

12 Roux, A. T. *et al.* Chloroquine and Sulfadoxine–Pyrimethamine Resistance in Sub-Saharan Africa—A Review. *Frontiers in Genetics* **12** (2021).

13 Diawara, H. *et al.* Cost-effectiveness of district-wide seasonal malaria chemoprevention when implemented through routine malaria control programme in Kita, Mali using fixed point distribution. *Malaria Journal* **20**, 128 (2021).

14 Palmer, K. J., Holliday, S. M. & Brogden, R. N. Mefloquine. *Drugs* **45**, 430-475 (1993).

15 Wong, W. *et al.* Mefloquine targets the Plasmodium falciparum 80S ribosome to inhibit protein synthesis. *Nat Microbiol* **2**, 17031 (2017).

16 Ringqvist, Å., Bech, P., Glenthøj, B. & Petersen, E. Acute and long-term psychiatric side effects of mefloquine: A follow-up on Danish adverse event reports. *Travel Medicine and Infectious Disease* **13**, 80-88 (2015).

17 Faurant, C. From bark to weed: the history of artemisinin. *Parasite* **18**, 215-218 (2011).

18 Meshnick, S. R. Artemisinin: mechanisms of action, resistance and toxicity. *International Journal for Parasitology* **32**, 1655-1660 (2002).

19 Noedl, H. *et al.* Evidence of Artemisinin-Resistant Malaria in Western Cambodia. *New England Journal of Medicine* **359**, 2619-2620 (2008).
20 Dondorp, A. M. *et al.* Artemisinin Resistance in Plasmodium falciparum Malaria. *New England Journal of Medicine* **361**, 455-467 (2009).
21 Ménard, D. *et al.* A Worldwide Map of Plasmodium falciparum K13-Propeller Polymorphisms. *New England Journal of Medicine* **374**, 2453-2464 (2016).
22 Ashley, E. A. *et al.* Spread of Artemisinin Resistance in Plasmodium falciparum Malaria. *New England Journal of Medicine* **371**, 411-423 (2014).
23 Klonis, N. *et al.* Altered temporal response of malaria parasites determines differential sensitivity to artemisinin. *Proceedings of the National Academy of Sciences* **110**, 5157-5162 (2013).
24 Ariey, F. *et al.* A molecular marker of artemisinin-resistant Plasmodium falciparum malaria. *Nature* **505**, 50-55 (2014).
25 Birnbaum, J. *et al.* A Kelch13-defined endocytosis pathway mediates artemisinin resistance in malaria parasites. *Science* **367**, 51-59 (2020).
26 World Health Organization. *Strategy to respond to antimalarial drug resistance in Africa.*, (2022).
27 Uwimana, A. *et al.* Emergence and clonal expansion of in vitro artemisinin-resistant Plasmodium falciparum kelch13 R561H mutant parasites in Rwanda. *Nature Medicine* **26**, 1602-1608 (2020).
28 Uwimana, A. *et al.* Association of Plasmodium falciparum kelch13 R561H genotypes with delayed parasite clearance in Rwanda: an open-label, single-arm, multicentre, therapeutic efficacy study. *The Lancet Infectious Diseases* **21**, 1120-1128 (2021).
29 Straimer, J., Gandhi, P., Renner, K. C. & Schmitt, E. K. High Prevalence of Plasmodium falciparum K13 Mutations in Rwanda Is Associated With Slow Parasite Clearance After Treatment With Artemether-Lumefantrine. *The Journal of Infectious Diseases* **225**, 1411-1414 (2021).
30 Balikagala, B. *et al.* Evidence of Artemisinin-Resistant Malaria in Africa. *New England Journal of Medicine* **385**, 1163-1171 (2021).
31 Burrows, J. N. *et al.* New developments in anti-malarial target candidate and product profiles. *Malar J* **16**, 26 (2017).
32 Novartis International AG. (2022).
33 White, N. J. *et al.* Antimalarial Activity of KAF156 in Falciparum and Vivax Malaria. *New England Journal of Medicine* **375**, 1152-1160 (2016).
34 Tse, E. G., Korsik, M. & Todd, M. H. The past, present and future of anti-malarial medicines. *Malaria Journal* **18**, 93 (2019).
35 Plouffe, D. *et al.* In silico activity profiling reveals the mechanism of action of antimalarials discovered in a high-throughput screen. *Proceedings of the National Academy of Sciences* **105**, 9059-9064 (2008).
36 Smilkstein, M., Sriwilaijaroen, N., Kelly, J. X., Wilairat, P. & Riscoe, M. Simple and inexpensive fluorescence-based technique for high-throughput antimalarial drug screening. *Antimicrob Agents Chemother* **48**, 1803-1806 (2004).
37 Baragaña, B. *et al.* A novel multiple-stage antimalarial agent that inhibits protein synthesis. *Nature* **522**, 315-320 (2015).

38 Hameed P, S. *et al.* Triaminopyrimidine is a fast-killing and long-acting antimalarial clinical candidate. *Nature Communications* **6**, 6715 (2015).
39 Taft, B. R. *et al.* Discovery and Preclinical Pharmacology of INE963, a Potent and Fast-Acting Blood-Stage Antimalarial with a High Barrier to Resistance and Potential for Single-Dose Cures in Uncomplicated Malaria. *Journal of Medicinal Chemistry* **65**, 3798-3813 (2022).
40 Murithi, J. M. *et al.* The antimalarial MMV688533 provides potential for single-dose cures with a high barrier to Plasmodium falciparum parasite resistance. *Sci Transl Med* **13** (2021).
41 Bopp, S. *et al.* Potent acyl-CoA synthetase 10 inhibitors kill Plasmodium falciparum by disrupting triglyceride formation. *Nature Communications* **14**, 1455 (2023).
42 Moffat, J. G., Vincent, F., Lee, J. A., Eder, J. & Prunotto, M. Opportunities and challenges in phenotypic drug discovery: an industry perspective. *Nature Reviews Drug Discovery* **16**, 531-543 (2017).
43 Forte, B. *et al.* Prioritization of Molecular Targets for Antimalarial Drug Discovery. *ACS Infectious Diseases* **7**, 2764-2776 (2021).
44 Hyman, A. A., Weber, C. A. & Jülicher, F. Liquid-liquid phase separation in biology. *Annu Rev Cell Dev Biol* **30**, 39-58 (2014).
45 Sabari, B. R. *et al.* Coactivator condensation at super-enhancers links phase separation and gene control. *Science* **361** (2018).
46 Du, M. & Chen, Z. J. DNA-induced liquid phase condensation of cGAS activates innate immune signaling. *Science* **361**, 704-709 (2018).
47 Molliex, A. *et al.* Phase separation by low complexity domains promotes stress granule assembly and drives pathological fibrillization. *Cell* **163**, 123-133 (2015).
48 Brangwynne, C. P. *et al.* Germline P granules are liquid droplets that localize by controlled dissolution/condensation. *Science* **324**, 1729-1732 (2009).
49 Strom, A. R. & Brangwynne, C. P. The liquid nucleome - phase transitions in the nucleus at a glance. *J Cell Sci* **132** (2019).
50 Li, P. *et al.* Phase transitions in the assembly of multivalent signalling proteins. *Nature* **483**, 336-340 (2012).
51 Kato, M. *et al.* Cell-free Formation of RNA Granules: Low Complexity Sequence Domains Form Dynamic Fibers within Hydrogels. *Cell* **149**, 753-767 (2012).
52 Banani, S. F., Lee, H. O., Hyman, A. A. & Rosen, M. K. Biomolecular condensates: organizers of cellular biochemistry. *Nat Rev Mol Cell Biol* **18**, 285-298 (2017).
53 Brangwynne, Clifford P., Tompa, P. & Pappu, Rohit V. Polymer physics of intracellular phase transitions. *Nature Physics* **11**, 899-904 (2015).
54 Wang, J. *et al.* A Molecular Grammar Governing the Driving Forces for Phase Separation of Prion-like RNA Binding Proteins. *Cell* **174**, 688-699.e616 (2018).
55 Brady, J. P. *et al.* Structural and hydrodynamic properties of an intrinsically disordered region of a germ cell-specific protein on phase separation. *Proc Natl Acad Sci U S A* **114**, E8194-E8203 (2017).
56 Babinchak, W. M. *et al.* The role of liquid-liquid phase separation in aggregation of the TDP-43 low-complexity domain. *J Biol Chem* **294**, 6306-6317 (2019).
57 Martin, E. W. *et al.* Interplay of folded domains and the disordered low-complexity domain in mediating hnRNPA1 phase separation. *Nucleic Acids Res* **49**, 2931-2945 (2021).
58 Shin, Y. & Brangwynne, C. P. Liquid phase condensation in cell physiology and disease. *Science* **357**, eaaf4382 (2017).

59 Feng, Z. P. *et al.* Abundance of intrinsically unstructured proteins in P. falciparum and other apicomplexan parasite proteomes. *Mol Biochem Parasitol* **150**, 256-267 (2006).
60 An, S., Kumar, R., Sheets, E. D. & Benkovic, S. J. Reversible compartmentalization of de novo purine biosynthetic complexes in living cells. *Science* **320**, 103-106 (2008).
61 Zhao, H. *et al.* Quantitative analysis of purine nucleotides indicates that purinosomes increase de novo purine biosynthesis. *J Biol Chem* **290**, 6705-6713 (2015).
62 Pedley, A. M., Pareek, V. & Benkovic, S. J. The Purinosome: A Case Study for a Mammalian Metabolon. *Annual Review of Biochemistry* **91**, 89-106 (2022).
63 Sheu-Gruttadauria, J. & MacRae, I. J. Phase Transitions in the Assembly and Function of Human miRISC. *Cell* **173**, 946-957.e916 (2018).
64 Zhang, J. Z. *et al.* Phase Separation of a PKA Regulatory Subunit Controls cAMP Compartmentation and Oncogenic Signaling. *Cell* **182**, 1531-1544.e1515 (2020).
65 Honeyman, J. N. *et al.* Detection of a recurrent DNAJB1-PRKACA chimeric transcript in fibrolamellar hepatocellular carcinoma. *Science* **343**, 1010-1014 (2014).
66 Feric, M. *et al.* Coexisting Liquid Phases Underlie Nucleolar Subcompartments. *Cell* **165**, 1686-1697 (2016).
67 Larson, A. G. *et al.* Liquid droplet formation by HP1α suggests a role for phase separation in heterochromatin. *Nature* **547**, 236-240 (2017).
68 Strom, A. R. *et al.* Phase separation drives heterochromatin domain formation. *Nature* **547**, 241-245 (2017).
69 Sun, L., Wu, J., Du, F., Chen, X. & Chen, Z. J. Cyclic GMP-AMP Synthase Is a Cytosolic DNA Sensor That Activates the Type I Interferon Pathway. *Science* **339**, 786-791 (2013).
70 Wang, H. *et al.* cGAS is essential for the antitumor effect of immune checkpoint blockade. *Proceedings of the National Academy of Sciences* **114**, 1637-1642 (2017).
71 Su, X. *et al.* Phase separation of signaling molecules promotes T cell receptor signal transduction. *Science* **352**, 595-599 (2016).
72 Chakraborty, A. K. & Weiss, A. Insights into the initiation of TCR signaling. *Nature Immunology* **15**, 798-807 (2014).
73 Mahboubi, H. & Stochaj, U. Cytoplasmic stress granules: Dynamic modulators of cell signaling and disease. *Biochimica et Biophysica Acta (BBA) - Molecular Basis of Disease* **1863**, 884-895 (2017).
74 Markmiller, S. *et al.* Context-Dependent and Disease-Specific Diversity in Protein Interactions within Stress Granules. *Cell* **172**, 590-604.e513 (2018).
75 Aulas, A. *et al.* Stress-specific differences in assembly and composition of stress granules and related foci. *J Cell Sci* **130**, 927-937 (2017).
76 Kedersha, N. *et al.* G3BP–Caprin1–USP10 complexes mediate stress granule condensation and associate with 40S subunits. *Journal of Cell Biology* **212** (2016).
77 Yang, P. *et al.* G3BP1 Is a Tunable Switch that Triggers Phase Separation to Assemble Stress Granules. *Cell* **181**, 325-345.e328 (2020).
78 Nakatogawa, H., Suzuki, K., Kamada, Y. & Ohsumi, Y. Dynamics and diversity in autophagy mechanisms: lessons from yeast. *Nature Reviews Molecular Cell Biology* **10**, 458-467 (2009).
79 Suzuki, K. *et al.* The pre-autophagosomal structure organized by concerted functions of APG genes is essential for autophagosome formation. *Embo j* **20**, 5971-5981 (2001).
80 Fujioka, Y. *et al.* Phase separation organizes the site of autophagosome formation. *Nature* **578**, 301-305 (2020).

81 Kamada, Y. *et al.* Tor-mediated induction of autophagy via an Apg1 protein kinase complex. *J Cell Biol* **150**, 1507-1513 (2000).
82 Glickman, M. H. & Ciechanover, A. The ubiquitin-proteasome proteolytic pathway: destruction for the sake of construction. *Physiol Rev* **82**, 373-428 (2002).
83 Yasuda, S. *et al.* Stress- and ubiquitylation-dependent phase separation of the proteasome. *Nature* **578**, 296-300 (2020).
84 Schmidt, H. B., Barreau, A. & Rohatgi, R. Phase separation-deficient TDP43 remains functional in splicing. *Nature Communications* **10**, 4890 (2019).
85 Ambadipudi, S., Biernat, J., Riedel, D., Mandelkow, E. & Zweckstetter, M. Liquid–liquid phase separation of the microtubule-binding repeats of the Alzheimer-related protein Tau. *Nature Communications* **8**, 275 (2017).
86 Ray, S. *et al.* α-Synuclein aggregation nucleates through liquid–liquid phase separation. *Nature Chemistry* **12**, 705-716 (2020).
87 Patel, A. *et al.* A Liquid-to-Solid Phase Transition of the ALS Protein FUS Accelerated by Disease Mutation. *Cell* **162**, 1066-1077 (2015).
88 Prasad, A., Bharathi, V., Sivalingam, V., Girdhar, A. & Patel, B. K. Molecular Mechanisms of TDP-43 Misfolding and Pathology in Amyotrophic Lateral Sclerosis. *Front Mol Neurosci* **12**, 25 (2019).
89 Neumann, M. *et al.* Ubiquitinated TDP-43 in frontotemporal lobar degeneration and amyotrophic lateral sclerosis. *Science* **314**, 130-133 (2006).
90 Arai, T. *et al.* TDP-43 is a component of ubiquitin-positive tau-negative inclusions in frontotemporal lobar degeneration and amyotrophic lateral sclerosis. *Biochem Biophys Res Commun* **351**, 602-611 (2006).
91 Mackenzie, I. R., Rademakers, R. & Neumann, M. TDP-43 and FUS in amyotrophic lateral sclerosis and frontotemporal dementia. *Lancet Neurol* **9**, 995-1007 (2010).
92 Buratti, E. in *Advances in Genetics* Vol. 91 (eds Theodore Friedmann, Jay C. Dunlap, & Stephen F. Goodwin) 1-53 (Academic Press, 2015).
93 Conicella, A. E., Zerze, G. H., Mittal, J. & Fawzi, N. L. ALS Mutations Disrupt Phase Separation Mediated by α-Helical Structure in the TDP-43 Low-Complexity C-Terminal Domain. *Structure* **24**, 1537-1549 (2016).
94 Maharana, S. *et al.* RNA buffers the phase separation behavior of prion-like RNA binding proteins. *Science* **360**, 918-921 (2018).
95 Pakravan, D., Orlando, G., Bercier, V. & Van Den Bosch, L. Role and therapeutic potential of liquid-liquid phase separation in amyotrophic lateral sclerosis. *J Mol Cell Biol* **13**, 15-28 (2021).
96 Hnisz, D. *et al.* Super-Enhancers in the Control of Cell Identity and Disease. *Cell* **155**, 934-947 (2013).
97 Zamudio, A. V. *et al.* Mediator Condensates Localize Signaling Factors to Key Cell Identity Genes. *Molecular Cell* **76**, 753-766.e756 (2019).
98 Nusse, R. & Clevers, H. Wnt/β-Catenin Signaling, Disease, and Emerging Therapeutic Modalities. *Cell* **169**, 985-999 (2017).
99 Békés, M., Langley, D. R. & Crews, C. M. PROTAC targeted protein degraders: the past is prologue. *Nature Reviews Drug Discovery* **21**, 181-200 (2022).
100 Liu, X. *et al.* PROTACs in Epigenetic Cancer Therapy: Current Status and Future Opportunities. *Molecules* **28** (2023).

101 Lu, J. *et al.* Hijacking the E3 Ubiquitin Ligase Cereblon to Efficiently Target BRD4. *Chemistry & Biology* **22**, 755-763 (2015).
102 Liao, X. *et al.* ARV-825 Demonstrates Antitumor Activity in Gastric Cancer via MYC-Targets and G2M-Checkpoint Signaling Pathways. *Frontiers in Oncology* **11** (2021).
103 Etibor, T. A., Yamauchi, Y. & Amorim, M. J. Liquid Biomolecular Condensates and Viral Lifecycles: Review and Perspectives. *Viruses* **13** (2021).
104 Chen, H. *et al.* Liquid-liquid phase separation by SARS-CoV-2 nucleocapsid protein and RNA. *Cell Res* **30**, 1143-1145 (2020).
105 Carlson, C. R. *et al.* Phosphoregulation of Phase Separation by the SARS-CoV-2 N Protein Suggests a Biophysical Basis for its Dual Functions. *Mol Cell* **80**, 1092-1103.e1094 (2020).
106 Iserman, C. *et al.* Genomic RNA Elements Drive Phase Separation of the SARS-CoV-2 Nucleocapsid. *Mol Cell* **80**, 1078-1091.e1076 (2020).
107 Wang, J., Shi, C., Xu, Q. & Yin, H. SARS-CoV-2 nucleocapsid protein undergoes liquid-liquid phase separation into stress granules through its N-terminal intrinsically disordered region. *Cell Discov* **7**, 5 (2021).
108 Wang, S. *et al.* Targeting liquid-liquid phase separation of SARS-CoV-2 nucleocapsid protein promotes innate antiviral immunity by elevating MAVS activity. *Nat Cell Biol* **23**, 718-732 (2021).
109 Seim, I., Roden, C. A. & Gladfelter, A. S. Role of spatial patterning of N-protein interactions in SARS-CoV-2 genome packaging. *Biophys J* **120**, 2771-2784 (2021).
110 Zheng, Z. Q., Wang, S. Y., Xu, Z. S., Fu, Y. Z. & Wang, Y. Y. SARS-CoV-2 nucleocapsid protein impairs stress granule formation to promote viral replication. *Cell Discov* **7**, 38 (2021).
111 Gordon, D. E. *et al.* A SARS-CoV-2 protein interaction map reveals targets for drug repurposing. *Nature* **583**, 459-468 (2020).
112 Hou, F. *et al.* MAVS forms functional prion-like aggregates to activate and propagate antiviral innate immune response. *Cell* **146**, 448-461 (2011).
113 O'Connell, J. D., Zhao, A., Ellington, A. D. & Marcotte, E. M. Dynamic reorganization of metabolic enzymes into intracellular bodies. *Annu Rev Cell Dev Biol* **28**, 89-111 (2012).
114 Giegé, P. *et al.* Enzymes of glycolysis are functionally associated with the mitochondrion in Arabidopsis cells. *Plant Cell* **15**, 2140-2151 (2003).
115 Sullivan, D. T. *et al.* Analysis of glycolytic enzyme co-localization in Drosophila flight muscle. *J Exp Biol* **206**, 2031-2038 (2003).
116 Mamczur, P., Dus, D. & Dzugaj, A. Colocalization of aldolase and FBPase in cytoplasm and nucleus of cardiomyocytes. *Cell Biol Int* **31**, 1122-1130 (2007).
117 Araiza-Olivera, D. *et al.* A glycolytic metabolon in Saccharomyces cerevisiae is stabilized by F-actin. *Febs j* **280**, 3887-3905 (2013).
118 Campanella, M. E., Chu, H. & Low, P. S. Assembly and regulation of a glycolytic enzyme complex on the human erythrocyte membrane. *Proceedings of the National Academy of Sciences* **102**, 2402-2407 (2005).
119 Agbor, T. A. *et al.* Small ubiquitin-related modifier (SUMO)-1 promotes glycolysis in hypoxia. *J Biol Chem* **286**, 4718-4726 (2011).
120 Miura, N. *et al.* Spatial reorganization of Saccharomyces cerevisiae enolase to alter carbon metabolism under hypoxia. *Eukaryot Cell* **12**, 1106-1119 (2013).
121 Jin, M. *et al.* Glycolytic Enzymes Coalesce in G Bodies under Hypoxic Stress. *Cell Reports* **20**, 895-908 (2017).

122 Fuller, G. G. *et al.* RNA promotes phase separation of glycolysis enzymes into yeast G bodies in hypoxia. *eLife* **9**, e48480 (2020).
123 Beckmann, B. M. *et al.* The RNA-binding proteomes from yeast to man harbour conserved enigmRBPs. *Nat Commun* **6**, 10127 (2015).
124 Jang, S. *et al.* Glycolytic Enzymes Localize to Synapses under Energy Stress to Support Synaptic Function. *Neuron* **90**, 278-291 (2016).
125 Jang, S. *et al.* Phosphofructokinase relocalizes into subcellular compartments with liquid-like properties in vivo. *Biophysical Journal* **120**, 1170-1186 (2021).
126 Quiñones, W. *et al.* Structure, Properties, and Function of Glycosomes in Trypanosoma cruzi. *Frontiers in Cellular and Infection Microbiology* **10** (2020).
127 Salcedo-Sora, J. E., Caamano-Gutierrez, E., Ward, S. A. & Biagini, G. A. The proliferating cell hypothesis: a metabolic framework for Plasmodium growth and development. *Trends Parasitol* **30**, 170-175 (2014).
128 Evers, F. *et al.* Composition and stage dynamics of mitochondrial complexes in Plasmodium falciparum. *Nat Commun* **12**, 3820 (2021).
129 Sturm, A., Mollard, V., Cozijnsen, A., Goodman, C. D. & McFadden, G. I. Mitochondrial ATP synthase is dispensable in blood-stage Plasmodium berghei rodent malaria but essential in the mosquito phase. *Proc Natl Acad Sci U S A* **112**, 10216-10223 (2015).
130 Slavic, K., Krishna, S., Derbyshire, E. T. & Staines, H. M. Plasmodial sugar transporters as anti-malarial drug targets and comparisons with other protozoa. *Malaria Journal* **10**, 165 (2011).
131 Jiang, X. *et al.* Structural Basis for Blocking Sugar Uptake into the Malaria Parasite Plasmodium falciparum. *Cell* **183**, 258-268.e212 (2020).
132 Shivapurkar, R. *et al.* Evaluating antimalarial efficacy by tracking glycolysis in Plasmodium falciparum using NMR spectroscopy. *Sci Rep* **8**, 18076 (2018).
133 Walliker, D. *et al.* Genetic analysis of the human malaria parasite Plasmodium falciparum. *Science* **236**, 1661-1666 (1987).
134 Tougan, T. *et al.* An automated haematology analyzer XN-30 distinguishes developmental stages of falciparum malaria parasite cultured in vitro. *Malar J* **17**, 59 (2018).
135 Ribaut, C. *et al.* Concentration and purification by magnetic separation of the erythrocytic stages of all human Plasmodium species. *Malaria Journal* **7**, 45 (2008).
136 Lambros, C. & Vanderberg, J. P. Synchronization of Plasmodium falciparum erythrocytic stages in culture. *J Parasitol* **65**, 418-420 (1979).
137 Spielmann, T. *et al.* Selection linked integration (SLI) for endogenous gene tagging and knock sideways in Plasmodium falciparum parasites. *Protocol Exchange* (2017).
138 Riglar, D. T. *et al.* Super-resolution dissection of coordinated events during malaria parasite invasion of the human erythrocyte. *Cell Host Microbe* **9**, 9-20 (2011).
139 Morita, M. *et al.* PV1, a novel Plasmodium falciparum merozoite dense granule protein, interacts with exported protein in infected erythrocytes. *Sci Rep* **8**, 3696 (2018).
140 Shaner, N. C. *et al.* A bright monomeric green fluorescent protein derived from Branchiostoma lanceolatum. *Nature Methods* **10**, 407-409 (2013).
141 Liu, Z. *et al.* Systematic comparison of 2A peptides for cloning multi-genes in a polycistronic vector. *Sci Rep* **7**, 2193 (2017).
142 Motohashi, K. A simple and efficient seamless DNA cloning method using SLiCE from Escherichia coli laboratory strains and its application to SLiP site-directed mutagenesis. *BMC Biotechnology* **15**, 47 (2015).

143 van den Hoff, M. J., Moorman, A. F. & Lamers, W. H. Electroporation in 'intracellular' buffer increases cell survival. *Nucleic Acids Res* **20**, 2902 (1992).
144 Schindelin, J. *et al.* Fiji: an open-source platform for biological-image analysis. *Nature Methods* **9**, 676-682 (2012).
145 Kanda, Y. Investigation of the freely available easy-to-use software 'EZR' for medical statistics. *Bone Marrow Transplant* **48**, 452-458 (2013).
146 Hwang, J., Gheber, L. A., Margolis, L. & Edidin, M. Domains in Cell Plasma Membranes Investigated by Near-Field Scanning Optical Microscopy. *Biophysical Journal* **74**, 2184-2190 (1998).
147 Su, W., Sun, J., Shimizu, K. & Kadota, K. TCC-GUI: a Shiny-based application for differential expression analysis of RNA-Seq count data. *BMC Research Notes* **12**, 133 (2019).
148 Mészáros, B., Erdős, G. & Dosztányi, Z. IUPred2A: context-dependent prediction of protein disorder as a function of redox state and protein binding. *Nucleic Acids Research* **46**, W329-W337 (2018).
149 Consortium, T. U. UniProt: the Universal Protein Knowledgebase in 2023. *Nucleic Acids Research* **51**, D523-D531 (2022).
150 Mi, H. *et al.* Protocol Update for large-scale genome and gene function analysis with the PANTHER classification system (v.14.0). *Nat Protoc* **14**, 703-721 (2019).
151 Benjamini, Y. & Hochberg, Y. Controlling the False Discovery Rate: A Practical and Powerful Approach to Multiple Testing. *Journal of the Royal Statistical Society: Series B (Methodological)* **57**, 289-300 (1995).
152 Monzon, A. M. *et al.* Experimentally Determined Long Intrinsically Disordered Protein Regions Are Now Abundant in the Protein Data Bank. *International Journal of Molecular Sciences* **21**, 4496 (2020).
153 López-Barragán, M. J. *et al.* Directional gene expression and antisense transcripts in sexual and asexual stages of Plasmodium falciparum. *BMC Genomics* **12**, 587 (2011).
154 Mony, B. M., Mehta, M., Jarori, G. K. & Sharma, S. Plant-like phosphofructokinase from Plasmodium falciparum belongs to a novel class of ATP-dependent enzymes. *International Journal for Parasitology* **39**, 1441-1453 (2009).
155 Jin, M. *et al.* Glycolytic Enzymes Coalesce in G Bodies under Hypoxic Stress. *Cell Rep* **20**, 895-908 (2017).
156 Jin, L., Millard, A. C., Wuskell, J. P., Clark, H. A. & Loew, L. M. Cholesterol-enriched lipid domains can be visualized by di-4-ANEPPDHQ with linear and nonlinear optics. *Biophys J* **89**, L04-06 (2005).
157 Jalihal, A. P. *et al.* Hyperosmotic phase separation: Condensates beyond inclusions, granules and organelles. *Journal of Biological Chemistry* **296** (2021).
158 Tokumasu, F. *et al.* Band 3 modifications in Plasmodium falciparum-infected AA and CC erythrocytes assayed by autocorrelation analysis using quantum dots. *Journal of Cell Science* **118**, 1091-1098 (2005).
159 Balaji, S., Babu, M. M., Iyer, L. M. & Aravind, L. Discovery of the principal specific transcription factors of Apicomplexa and their implication for the evolution of the AP2-integrase DNA binding domains. *Nucleic Acids Research* **33**, 3994-4006 (2005).
160 Martin, E. W. & Holehouse, A. S. Intrinsically disordered protein regions and phase separation: sequence determinants of assembly or lack thereof. *Emerg Top Life Sci* **4**, 307-329 (2020).

161 Branco, A., Francisco, D. & Hanscheid, T. Is There a 'Normal' Oxygen Concentration for in vitro Plasmodium Cultures? *Trends Parasitol* **34**, 811-812 (2018).
162 Pillai, A. D. *et al.* Solute restriction reveals an essential role for clag3-associated channels in malaria parasite nutrient acquisition. *Mol Pharmacol* **82**, 1104-1114 (2012).
163 Desai, S. A. Insights gained from P. falciparum cultivation in modified media. *ScientificWorldJournal* **2013**, 363505 (2013).
164 Kim, H., Certa, U., Döbeli, H., Jakob, P. & Hol, W. G. J. Crystal Structure of Fructose-1,6-bisphosphate Aldolase from the Human Malaria Parasite Plasmodium falciparum. *Biochemistry* **37**, 4388-4396 (1998).
165 Robien, M. A. *et al.* Crystal structure of glyceraldehyde-3-phosphate dehydrogenase from Plasmodium falciparum at 2.25 Å resolution reveals intriguing extra electron density in the active site. *Proteins: Structure, Function, and Bioinformatics* **62**, 570-577 (2006).
166 Pal-Bhowmick, I. *et al.* Cloning, over-expression, purification and characterization of Plasmodium falciparum enolase. *European Journal of Biochemistry* **271**, 4845-4854 (2004).
167 Smith, C. D., Chattopadhyay, D. & Pal, B. Crystal structure of Plasmodium falciparum phosphoglycerate kinase: Evidence for anion binding in the basic patch. *Biochemical and Biophysical Research Communications* **412**, 203-206 (2011).
168 Patel, A. *et al.* ATP as a biological hydrotrope. *Science* **356**, 753-756 (2017).
169 MacRae, J. I. *et al.* Mitochondrial metabolism of sexual and asexual blood stages of the malaria parasite Plasmodium falciparum. *BMC Biology* **11**, 67 (2013).
170 Takashima, E. *et al.* Isolation of mitochondria from Plasmodium falciparum showing dihydroorotate dependent respiration. *Parasitology International* **50**, 273-278 (2001).
171 Chappell, L. *et al.* Refining the transcriptome of the human malaria parasite Plasmodium falciparum using amplification-free RNA-seq. *BMC Genomics* **21**, 395 (2020).
172 Kucharski, M. *et al.* A comprehensive RNA handling and transcriptomics guide for high-throughput processing of Plasmodium blood-stage samples. *Malar J* **19**, 363 (2020).
173 Zhu, Y. *et al.* The long noncoding RNA glycoLINC assembles a lower glycolytic metabolon to promote glycolysis. *Molecular Cell* **82**, 542-554.e546 (2022).
174 Cho, W.-K. *et al.* Mediator and RNA polymerase II clusters associate in transcription-dependent condensates. *Science* **361**, 412-415 (2018).
175 Binh, T. Q. *et al.* Glucose metabolism in severe malaria: Minimal model analysis of the intravenous glucose tolerance test incorporating a stable glucose label. *Metabolism* **46**, 1435-1440 (1997).

Appendix

Name	Sequence
PfPGK	ACGTAACAGACTTAGGAGGGACCACTACTAGCCATTTTAGGTGGTGCTAAAGTATCAGATAAAATTCAGTTA ATCAAAAATTTATTAGATAAAGTTGATCGTATGATTATTGGAGGTGGTATGGCTTATACTTTTAAAAAAGTCT TAAACAATATGAAAATTGGTACCTCTCTTTTTGATGAAGCAGGTAGTAAAATTGTTGGAGAAATTATGGAAA AGGCAAAAGCTAAAAATGTTCAAATATTTTTACCTGTAGATTTTAAAATTGCAGATAATTTTGATAATAATGC TAATACCAAATTCGTTACTGATGAAGAAGGTATCCCAGATAATTGGATGGGTCTTGATGCTGGTCCAAAAAG TATTGAAAATTATAAAGATGTTATTTTAACATCAAAAACTGTTATTTGGAACGGACCACAAGGTGTTTTCGAA ATGCCAAACTTTGCAAAAGGTAGTATCGAATGTCTCAATTTAGTTGTTGAAGTTACCAAAAAAGGAGCTATC ACCATTGTTGGAGGTGGAGATACAGCTTCATTAGTTGAACAACAAAATAAGAAAAACGAAATTAGTCATGTA TCTACAGGTGGAGGAGCCTCACTTGAACTTTTAGAAGGAAAAGAATTACCAGGTGTATTAGCACTTTCAAAC AAAATGGTGAGTAAGGGAGAAG
PfTIM	ACGTAACAGACTTAGGAGGTAGGACGTTGTTGTTTTTCCTGTTTCCGTACATTATGATCATACAAGGAAATTA CTTCAGAGTAAGTTTTCTACTGGTATTCAGAATGTATCAAAATTCGGAAATGGATCATACACAGGTGAAGTA AGTGCAGAAATTGCCAAGGATTTAAATATTGAATATGTTATTATTGGTCATTTTGAAAGAAGAAAAATATTTCC ATGAAACCGATGAAGATGTTCGTGAAAAATTACAAGCTTCATTAAAAAATAATTTAAAAGCCGTTGTATGTT TTGGTGAATCTTTAGAACAAAGAGAACAAAATAAAACTATCGAAGTTATTACAAAACAAGTTAAAGCATTTG TTGATTTAATTGATAATTTTGATAATGTTATTTTGGCTTATGAACCTTTATGGGCTATTGGTACTGGTAAAACA GCTACACCTGAACAAGCTCAATTAGTACACAAAGAAATCAGAAAAATTGTAAAAGATACATGCGGAGAAAA ACAAGCTAACCAAATAAGAATATTATATGGAGGTAGTGTTAATACTGAAAACTGCTCTTCATTAATTCAACA AGAAGATATTGATGGTTTCTTAGTTGGAAATGCTTCCTTAAAAGAATCTTTTGTTGATATAATAAAAAGTGCT ATGATGGTGAGTAAGGGAGAAG
PfGPI	ACGTAACAGACTTAGGAGGTAGCAAAATTTATTAAAATTTTCAGCACATATTCAACAATTATCTATGGAAAG TAATGGAAAATCAGTAGATAGAAATAATCAACCAATCCATTATAATACTTGTCAAGTATATTTTGGTGAACCT GGTACAAATGGTCAGCATAGTTTTTATCAATTAATACATCAAGGACAAGTTATACCTGTTGAATTAATTGGAT TTAAACATTCTCATTTCCCAATTAAATTTGATAAAGAAGTAGTAAGTAATCATGATGAATTAATGACTAACTT TTTTGCACAAGCTGATGCATTAGCTATTGGGAAAACATACGAACAAGTAAAAGAAGAAAATGAAAAAAATA AAATGTCTCCAGAATTATTAACTCATAAAGTTTTTAACGGTAATAGACCATCAACCTTATTATTATTTGATGA ATTAAATTTCTATACATGTGGTTTATTATTATCCTTATATGAAAGTAGAATTGTCGCTGAAGGATTTCTATTAA ATATTAACAGCTTTGATCAATGGGGGGTAGAGTTGGGTAAGGTTCTAGCAAAAGAAGTAAGAAATTATTTTA ATGACACAAGAAATCAAAAGAAATCAGATAATACCTATAATTTTAATGAATCTACAAAAATTTTATTAAATT ATTACTTGTCCAAAATGGTGAGTAAGGGAGAAG
PfPyrK	ACGTAACAGACTTAGGAGGTAGCCTTCCATTTATAGATGCAATTTACAAGGTAAACCAATTATCACTGCCACT CAAATGTTAGAATCCATGACCAAGAACCCAAGACCAACAAGAGCAGAAGTTACAGATGTAGCTAATGCTGTT TTAGATGGTACTGATTGTGTTATGCTTTCAGGAGAAACTGCAGGTGGTAAATTTCCAGTGGAAGCTGTTACCA TTATGTCCAAAATCTGTTTAGAAGCAGAAGCATGCATTGATTATAAATTATTATATCAATCATTAGTAAATGC AATTGAAACACCAATTAGTGTTCAAGAAGCTGTGGCTAGATCAGCTGTAGAAACAGCAGAATCTATTCAAGC TTCTTTAATTATAGCTTTAACAGAAACAGGTTATACGGCTAGATTAATTGCCAAATATAAACCAAGTTGTACC ATCTTAGCCCTTAGTGCTTCTGATTCAACTGTTAAATGTTTGAACGTACACAGAGGTGTTACATGCATTAAAG TAGGTTCATTCCAAGGAACAGATATTGTTATTAGAAATGCTATTGAAATCGCAAAACAAAGAAATATGGCAA AAGTTGGTGATAGCGTTATTGCTATTCACGGAATTAAAGAAGAAGTATCTGGAGGTACCAACTTAATGAAAG TTGTACAAATTGAAATGGTGAGTAAGGGAGAAG

Table A.1 Synthesized DNAs used for plasmid construction.

ID	Compound name	Pathway Label	PubChem CID	glucose-5mM			glucose-10mM			glucose-5mM		glucose-10mM		glucose-5mM vs glucose-10mM	
				A1	A2	A3	B1	B2	B3	Mean	S.D.	Mean	S.D.	Ratio ¶	*p*-value ‖
A_0001	NAD^+	NAD+	5893	251	251	171	273	284	201	224	46	253	45	0.9	0.485
A_0002	cAMP	cAMP	6076	0.2	0.14	0.12	0.2	0.14	0.11	0.14	0.02	0.14	0.02	1.0	0.983
A_0003	cGMP	cGMP	24316	0.02	0.02	0.010	0.02	0.02	0.02	0.02	0.007	0.02	0.002	0.9	0.664
A_0004	NADH	NADH	439153	4.2	4.0	3.9	4.0	4.2	3.5	4.0	0.11	3.9	0.4	1.0	0.655
A_0005	Xanthine	Xanthine	1188	0.2	0.2	0.2	0.14	0.2	0.2	0.2	0.02	0.2	0.05	1.1	0.685
A_0006	ADP-ribose	ADP-Rib	445794	1.5	1.3	0.9	1.2	1.2	1.0	1.2	0.3	1.1	0.14	1.1	0.685
A_0007	Mevalonic acid	Mevalonic acid	134965	N.D.	N.D.	N.D.	N.D.	N.D.	N.D.	N.A.	N.A.	N.A.	N.A.	N.A.	N.A.
A_0008	UDP-glucose	UDP-Glc	8629	16	16	11	17	19	14	14	3.1	17	2.7	0.9	0.358
A_0009	Uric acid	Uric acid	1175	N.D.	N.D.	N.D.	N.D.	N.D.	N.D.	N.A.	N.A.	N.A.	N.A.	N.A.	N.A.
A_0010	$NADP^+$	NADP+	5886	27	23	17	27	28	19	22	5.1	25	4.9	0.9	0.597
A_0011	IMP	IMP	8582	57	72	33	79	111	65	54	20	85	24	0.6	0.160
A_0012	Sedoheptulose 7-phosphate	S7P	165007	N.D.	N.D.	N.D.	N.D.	N.D.	N.D.	N.A.	N.A.	N.A.	N.A.	N.A.	N.A.
A_0013	Glucose 6-phosphate	G6P	5958	56	56	40	53	51	41	51	9.5	48	6.4	1.0	0.760
A_0014	Fructose 6-phosphate	F6P	603	3.3	2.7	2.3	3.5	2.6	2.3	2.8	0.5	2.8	0.6	1.0	0.993
A_0015	Fructose 1-phosphate	D-F1P	439394	N.D.	N.D.	N.D.	N.D.	N.D.	N.D.	N.A.	N.A.	N.A.	N.A.	N.A.	N.A.
A_0016	Galactose 1-phosphate	Gal1P	123912	N.D.	N.D.	N.D.	N.D.	N.D.	N.D.	N.A.	N.A.	N.A.	N.A.	N.A.	N.A.
A_0017	Glucose 1-phosphate	G1P	65533	N.D.	N.D.	N.D.	N.D.	N.D.	N.D.	N.A.	N.A.	N.A.	N.A.	N.A.	N.A.
A_0018	Acetoacetyl CoA	AAcCoA	92153	N.D.	N.D.	N.D.	N.D.	N.D.	N.D.	N.A.	N.A.	N.A.	N.A.	N.A.	N.A.
A_0019	Acetyl CoA	AcCoA	444493	0.04	0.11	0.12	0.12	0.10	0.10	0.09	0.04	0.11	0.010	0.8	0.517
A_0020	Folic acid	Folic acid	6037	2.1	1.4	2.1	1.2	1.4	1.3	1.9	0.4	1.3	0.12	1.4	0.136
A_0021	Ribose 5-phosphate	R5P	439167	4.2	4.7	4.2	5.3	4.8	3.5	4.4	0.3	4.6	1.0	1.0	0.806
A_0022	CoA	CoA	87642	0.4	0.4	0.4	0.4	0.5	0.4	0.4	0.015	0.4	0.04	1.0	0.734
A_0023	Ribose 1-phosphate	R1P	439236	1.1	1.6	0.5	1.1	1.6	0.8	1.1	0.6	1.2	0.4	0.9	0.826
A_0024	Ribulose 5-phosphate	Ru5P	439184	4.7	4.3	4.4	4.6	3.6	3.5	4.4	0.2	3.9	0.6	1.1	0.257
A_0025	Xylulose 5-phosphate	X5P	439190	N.D.	N.D.	N.D.	1.5	N.D.	N.D.	N.A.	N.A.	1.5	N.A.	<1	N.A.
A_0026	Erythrose 4-phosphate	E4P	122357	N.D.	N.D.	N.D.	N.D.	N.D.	N.D.	N.A.	N.A.	N.A.	N.A.	N.A.	N.A.
A_0027	HMG CoA	HMG-CoA	445127	N.D.	N.D.	N.D.	N.D.	N.D.	N.D.	N.A.	N.A.	N.A.	N.A.	N.A.	N.A.
A_0028	Glyceraldehyde 3-phosphate	Glyceraldehyde 3-phosphate	729	2.0	2.4	5.5	5.5	4.4	2.5	3.3	1.9	4.1	1.5	0.8	0.595
A_0029	NADPH	NADPH	5884	2.7	2.7	2.8	2.6	3.0	2.6	2.7	0.04	2.8	0.2	1.0	0.863
A_0030	Malonyl CoA	Malonyl-CoA	644066	N.D.	N.D.	N.D.	N.D.	N.D.	N.D.	N.A.	N.A.	N.A.	N.A.	N.A.	N.A.
A_0031	Phosphocreatine	Phosphocreatine	9548602	N.D.	N.D.	N.D.	N.D.	N.D.	N.D.	N.A.	N.A.	N.A.	N.A.	N.A.	N.A.
A_0032	XMP	XMP	73323	0.2	0.2	0.15	0.2	0.3	0.2	0.2	0.04	0.2	0.06	0.8	0.217
A_0033	Dihydroxyacetone phosphate	DHAP	668	16	14	19	18	11	12	16	2.6	14	4.1	1.2	0.409
A_0034	Adenylosuccinic acid	Succinyl AMP	447145	5.1	4.7	2.9	6.8	7.4	4.7	4.2	1.2	6.3	1.4	0.7	0.132
A_0035	Fructose 1,6-diphosphate	F1,6P	172313	23	15	21	23	16	14	19	4.3	18	4.4	1.1	0.624
A_0036	6-Phosphogluconic acid	6-PG	91493	1.2	1.0	1.0	1.4	1.0	0.9	1.1	0.14	1.1	0.3	1.0	0.854
A_0037	*N*-Carbamoylaspartic acid	Carbamoyl-Asp	93072	15	12	11	15	16	12	13	1.7	14	2.3	0.9	0.359
A_0038	PRPP	PRPP	7339	1.6	1.7	2.3	1.1	2.1	1.1	1.9	0.4	1.5	0.6	1.3	0.371
A_0039	2-Phosphoglyceric acid	2-PG	439278	18	17	13	17	15	10	16	2.7	14	3.6	1.1	0.527
A_0040	2,3-Diphosphoglyceric acid	Diphosphoglycerate	186004	65	54	65	44	59	50	61	6.3	51	7.2	1.2	0.153
A_0041	3-Phosphoglyceric acid	3-PG	439183	92	97	71	83	78	60	87	14	74	12	1.2	0.278
A_0042	Phosphoenolpyruvic acid	PEP	1005	9.1	9.3	7.1	11	8.8	6.2	8.5	1.2	8.8	2.6	1.0	0.860
A_0043	GMP	GMP	6804	44	45	24	48	45	34	38	12	42	7.4	0.9	0.623
A_0044	AMP	AMP	6083	157	181	70	176	188	125	136	58	163	34	0.8	0.532
A_0045	2-Oxoisovaleric acid	2-KIV	49	N.D.	N.D.	N.D.	N.D.	N.D.	N.D.	N.A.	N.A.	N.A.	N.A.	N.A.	N.A.
A_0046	GDP	GDP	8977	8.9	7.8	6.6	8.4	8.5	7.5	7.8	1.2	8.1	0.6	1.0	0.680
A_0047	Lactic acid	Lactic acid	612	3,575	2,974	4,726	3,204	3,226	2,838	3,758	890	3,089	218	1.2	0.322
A_0048	ADP	ADP	6022	81	77	56	85	89	62	72	13	79	15	0.9	0.567
A_0049	GTP	GTP	6830	17	13	16	15	13	13	15	2.3	14	0.9	1.1	0.316
A_0050	Glyoxylic acid	Glyoxylic acid	760	N.D.	N.D.	N.D.	N.D.	N.D.	N.D.	N.A.	N.A.	N.A.	N.A.	N.A.	N.A.
A_0051	ATP	ATP	5957	88	69	96	81	74	72	84	14	76	4.3	1.1	0.398
A_0052	Glycerol 3-phosphate	Glycerol 3-phosphate	439162	55	51	47	64	55	47	51	4.0	55	8.6	0.9	0.517
A_0053	Glycolic acid	Glycolic acid	757	N.D.	N.D.	N.D.	N.D.	N.D.	N.D.	N.A.	N.A.	N.A.	N.A.	N.A.	N.A.
A_0054	Pyruvic acid	Pyruvic acid	1060	17	53	74	46	46	35	48	29	42	6.5	1.1	0.773
A_0055	*N*-Acetylglutamic acid	N-AcGlu	70914	0.9	N.D.	N.D.	N.D.	0.9	N.D.	0.9	N.A.	0.9	N.A.	0.9	N.A.
A_0056	2-Hydroxyglutaric acid	2-Hydroxyglutaric acid	43	1.0	1.6	0.9	1.2	1.6	1.1	1.2	0.3	1.3	0.3	0.9	0.689
A_0057	Carbamoylphosphate	Carbamoyl-P	278	N.D.	1.6	N.D.	2.0	N.D.	N.D.	1.6	N.A.	2.0	N.A.	0.8	N.A.
A_0058	Succinic acid	Succinic acid	1110	33	34	22	35	39	26	29	6.5	33	6.8	0.9	0.528
A_0059	Malic acid	Malic acid	525	65	60	47	92	99	67	57	9.3	86	17	0.7	0.076
A_0060	2-Oxoglutaric acid	2-OG	51	29	41	22	31	42	25	31	9.6	33	8.5	0.9	0.799
A_0061	Fumaric acid	Fumaric acid	444972	6.1	3.5	2.6	13	11	9.3	4.1	1.8	11	1.6	0.4	0.008 **
A_0062	Citric acid	Citric acid	311	62	41	73	37	41	41	58	16	40	2.1	1.5	0.188
A_0063	*cis*-Aconitic acid	cis-Aconitic acid	643757	0.4	0.4	0.6	0.3	0.3	0.2	0.5	0.13	0.3	0.04	1.7	0.118
A_0064	Isocitric acid	Isocitric acid	1198	N.D.	N.D.	N.D.	N.D.	N.D.	N.D.	N.A.	N.A.	N.A.	N.A.	N.A.	N.A.
C_0001	Urea	Urea	1176	N.D.	N.D.	N.D.	4.2	N.D.	N.D.	N.A.	N.A.	4.2	N.A.	<1	N.A.
C_0002	Gly	Gly	750	246	196	284	188	190	189	242	44	189	1.1	1.3	0.170
C_0003	Putrescine	Putrescine	1045	69	69	66	66	76	62	68	1.9	68	7.2	1.0	0.903
C_0004	Sarcosine	Sarcosine	1088	N.D.	N.D.	N.D.	N.D.	N.D.	N.D.	N.A.	N.A.	N.A.	N.A.	N.A.	N.A.
C_0005	Ala	Ala	602	71	68	64	69	67	54	67	3.6	64	8.2	1.1	0.526
C_0006	β-Ala	b-Ala	239	N.D.	N.D.	N.D.	N.D.	N.D.	N.D.	N.A.	N.A.	N.A.	N.A.	N.A.	N.A.
C_0007	*N,N*-Dimethylglycine	DMG	673	N.D.	N.D.	N.D.	N.D.	N.D.	N.D.	N.A.	N.A.	N.A.	N.A.	N.A.	N.A.
C_0008	γ-Aminobutyric acid	g-Aminobutyric acid	119	33	39	27	53	67	46	33	6.3	55	11	0.6	0.048 *
C_0009	Choline	Choline	305	49	45	57	46	49	45	50	6.1	47	2.1	1.1	0.432

Table A.2.1 The results of metabolome analysis (page1)

ID	Compound name	Pathway Label	PubChem CID	glucose-5mM			glucose-10mM			glucose-5mM		glucose-10mM		glucose-5mM vs glucose-10mM	
				A1	A2	A3	B1	B2	B3	Mean	S.D.	Mean	S.D.	Ratio	*p*-value
C_0010	Ser	Ser	617	423	322	508	316	321	334	418	93	323	9.3	1.3	0.219
C_0011	Carnosine	Carnosine	439224	N.D.	N.D.	N.D.	N.D.	N.D.	N.D.	N.A.	N.A.	N.A.	N.A.	N.A.	N.A.
C_0012	Creatinine	Creatinine	588	N.D.	N.D.	N.D.	N.D.	N.D.	N.D.	N.A.	N.A.	N.A.	N.A.	N.A.	N.A.
C_0013	Pro	Pro	614	259	204	263	201	209	206	242	33	205	3.7	1.2	0.197
C_0014	Val	Val	1182	291	223	331	231	224	223	282	54	226	4.8	1.2	0.216
C_0015	Betaine	Betaine	247	N.D.	N.D.	N.D.	N.D.	N.D.	N.D.	N.A.	N.A.	N.A.	N.A.	N.A.	N.A.
C_0016	Thr	Thr	6288	229	173	297	173	187	193	233	62	184	10	1.3	0.303
C_0017	Homoserine	Homoserine	12647	N.D.	0.2	N.D.	0.3	N.D.	0.4	0.2	N.A.	0.3	0.08	0.8	N.A.
C_0018	Betaine aldehyde	BTL	249	N.D.	N.D.	N.D.	N.D.	N.D.	N.D.	N.A.	N.A.	N.A.	N.A.	N.A.	N.A.
C_0019	Cys	Cys	594	1.2	3.6	9.0	1.1	1.2	1.5	4.6	4.0	1.3	0.2	3.5	0.291
C_0020	Hydroxyproline	Hydroxyproline	5810	207	159	275	152	159	168	214	58	160	8.1	1.3	0.246
C_0021	Creatine	Creatine	586	9.3	10	12	9.2	11	10	10	1.3	10	0.8	1.0	0.735
C_0022	Ile	Ile	791	479	366	550	337	353	392	465	93	361	28	1.3	0.185
C_0023	Leu	Leu	857	523	425	616	392	404	413	521	96	403	11	1.3	0.164
C_0024	Asn	Asn	236	525	416	662	365	412	428	534	123	402	33	1.3	0.199
C_0025	Ornithine	Ornithine	389	99	103	136	84	94	92	113	21	90	5.2	1.2	0.195
C_0026	Asp	Asp	424	317	280	323	277	293	259	307	23	276	17	1.1	0.149
C_0027	Homocysteine	Homocysteine	778	N.D.	N.D.	N.D.	N.D.	N.D.	N.D.	N.A.	N.A.	N.A.	N.A.	N.A.	N.A.
C_0028	Adenine	Adenine	190	1.1	0.9	1.0	1.1	1.3	1.1	1.0	0.10	1.2	0.10	0.9	0.150
C_0029	Hypoxanthine	Hypoxanthine	790	535	423	596	410	390	431	518	87	410	20	1.3	0.161
C_0030	Spermidine	Spermidine	1102	120	120	109	108	118	106	116	5.9	111	6.5	1.1	0.330
C_0031	Gln	Gln	738	1,915	1,516	2,388	1,477	1,521	1,591	1,940	436	1,530	57	1.3	0.244
C_0032	Lys	Lys	866	377	291	425	272	288	291	365	68	284	10	1.3	0.174
C_0033	Glu	Glu	611	625	600	599	648	684	601	608	15	644	42	0.9	0.266
C_0034	Met	Met	876	103	81	136	81	79	84	107	28	81	2.1	1.3	0.252
C_0035	Guanine	Guanine	764	9.9	11	6.1	11	12	9.0	9.0	2.6	11	1.5	0.8	0.399
C_0036	His	His	773	166	131	190	132	134	133	162	30	133	1.0	1.2	0.225
C_0037	Carnitine	Carnitine	85	N.D.	N.D.	N.D.	N.D.	N.D.	N.D.	N.A.	N.A.	N.A.	N.A.	N.A.	N.A.
C_0038	Phe	Phe	994	136	112	168	111	111	110	139	28	111	0.6	1.3	0.226
C_0039	Arg	Arg	6322	1,017	775	1,307	786	789	904	1,033	266	826	67	1.3	0.309
C_0040	Citrulline	Citrulline	9750	429	321	420	234	211	227	390	60	224	12	1.7	0.036
C_0041	Tyr	Tyr	1153	136	110	170	104	112	110	139	30	109	3.8	1.3	0.222
C_0042	*S*-Adenosylhomocysteine	SAH	439155	4.4	5.1	3.4	4.5	5.1	3.8	4.3	0.9	4.4	0.7	1.0	0.827
C_0043	Spermine	Spermine	1103	0.8	0.7	0.7	0.6	0.6	0.6	0.7	0.07	0.6	0.02	1.3	0.058
C_0044	Trp	Trp	1148	32	26	40	25	25	26	33	6.7	25	0.5	1.3	0.194
C_0045	Cystathionine	Cystathionine	834	N.D.	N.D.	N.D.	N.D.	N.D.	N.D.	N.A.	N.A.	N.A.	N.A.	N.A.	N.A.
C_0046	Adenosine	Adenosine	60961	0.4	0.4	0.3	0.5	0.4	0.3	0.4	0.08	0.4	0.06	0.9	0.747
C_0047	Inosine	Inosine	6021	10	10	11	11	11	8.7	11	0.3	10	1.5	1.0	0.863
C_0048	Guanosine	Guanosine	6802	1.1	1.3	0.5	1.5	1.7	1.2	1.0	0.4	1.4	0.3	0.7	0.216
C_0049	Argininosuccinic acid	ArgSuccinate	16950	0.7	N.D.	0.7	N.D.	0.7	0.6	0.7	0.007	0.7	0.06	1.0	0.956
C_0050	Glutathione (GSSG)	GSSG	65359	123	138	69	131	164	113	110	36	136	26	0.8	0.373
C_0051	Glutathione (GSH)	GSH	124886	4.2	7.7	5.8	4.1	5.1	4.5	5.9	1.7	4.6	0.5	1.3	0.304
C_0052	*S*-Adenosylmethionine	SAM	34755	12	13	8.1	14	13	11	11	2.5	13	1.7	0.9	0.364
-	Adenylate Energy Charge	No Label		0.4	0.3	0.6	0.4	0.3	0.4	0.4	0.12	0.4	0.03	1.2	0.465
-	Total Adenylate	No Label		326	327	223	342	352	259	292	60	317	51	0.9	0.603
-	Guanylate Energy Charge	No Label		0.3	0.3	0.4	0.3	0.3	0.3	0.3	0.08	0.3	0.03	1.2	0.436
-	Total Guanylate	No Label		70	66	47	71	66	54	61	12	64	8.5	1.0	0.751
-	GSH/GSSG	No Label		0.03	0.06	0.08	0.03	0.03	0.04	0.06	0.03	0.03	0.005	1.7	0.235
-	Total Glutathione	No Label		251	284	143	266	333	231	226	73	277	52	0.8	0.386
-	NADPH/NADP+	No Label		0.10	0.12	0.2	0.10	0.11	0.14	0.13	0.03	0.11	0.02	1.1	0.605
-	NADH/NAD+	No Label		0.02	0.02	0.02	0.015	0.015	0.02	0.02	0.004	0.02	0.002	1.2	0.348
-	Lactate/Pyruvate	No Label		213	56	64	70	69	81	111	89	73	6.6	1.5	0.540
-	Glycerol 3-phosphate/DHAP	No Label		3.4	3.7	2.5	3.5	5.0	4.0	3.2	0.6	4.2	0.8	0.8	0.179
-	Total Amino Acids	No Label		7,872	6,320	9,330	6,186	6,405	6,543	7,841	1,505	6,378	180	1.2	0.233
-	Total Essential Amino Acids	No Label		2,338	1,829	2,753	1,754	1,807	1,865	2,307	463	1,808	55	1.3	0.202
-	Total Non-essential Amino Acids	No Label		5,534	4,492	6,577	4,433	4,598	4,678	5,534	1,042	4,570	125	1.2	0.249
-	Total Glucogenic Amino Acids	No Label		6,972	5,605	8,288	5,522	5,712	5,838	6,955	1,342	5,691	159	1.2	0.243
-	Total Ketogenic Amino Acids	No Label		1,913	1,504	2,266	1,414	1,481	1,536	1,895	382	1,477	61	1.3	0.196
-	Total BCAA	No Label		1,294	1,014	1,497	961	981	1,028	1,268	243	990	35	1.3	0.183
-	Total Aromatic Amino Acids	No Label		304	249	378	240	248	246	310	65	245	4.2	1.3	0.221
-	Fischer's Ratio	No Label		4.3	4.1	4.0	4.0	4.0	4.2	4.1	0.15	4.0	0.12	1.0	0.664 **
-	Total Glu-related Amino Acids	No Label		3,981	3,226	4,746	3,244	3,336	3,435	3,985	760	3,338	96	1.2	0.278
-	Total Pyr-related Amino Acids	No Label		1,003	790	1,201	772	792	797	998	205	787	14	1.3	0.217
-	Total Acetyl CoA-related Amino Acids	No Label		1,412	1,108	1,631	1,026	1,071	1,123	1,384	263	1,073	48	1.3	0.174
-	Total Fumarate-related Amino Acids	No Label		272	223	338	215	223	220	278	58	220	3.8	1.3	0.225
-	Total Succinyl CoA-related Amino Acids	No Label		874	670	1,017	649	656	698	854	175	668	27	1.3	0.205
-	Total Oxaloacetate-related Amino Acids	No Label		842	696	985	642	705	687	841	145	678	33	1.2	0.186
-	Malate/Asp	No Label		0.2	0.2	0.15	0.3	0.3	0.3	0.2	0.04	0.3	0.04	0.6	0.022
-	Citrulline/Ornithine	No Label		4.3	3.1	3.1	2.8	2.2	2.5	3.5	0.7	2.5	0.3	1.4	0.120
-	Glu/2-Oxoglutarate	No Label		21	15	28	21	16	24	21	6.4	20	3.9	1.0	0.867
-	G6P/R5P	No Label		13	12	9.4	9.9	11	12	12	2.0	11	0.9	1.1	0.604
-	SAM/SAH	No Label		2.6	2.5	2.4	3.1	2.7	2.9	2.5	0.11	2.9	0.2	0.9	0.091 *
-	Putrescine/Spermidine	No Label		0.6	0.6	0.6	0.6	0.6	0.6	0.6	0.014	0.6	0.03	0.9	0.170

Table A.2.2 The results of metabolome analysis (page2)

```
import requests
import pandas as pd

gene_list = pd.read_csv("uniprot-proteome_UP000001450.tab", sep='¥t')

fraction = []

iupred_type = "long"

for accession in gene_list["Entry"]:
    response = requests.get("http://iupred2a.elte.hu/iupred2a/" + iupred_type + "/" + accession + ".json")
    result = pd.read_json(response.text)
    score = result["iupred2"]
    fraction.append(len(score[score>=0.5])/len(score))

df = pd.DataFrame(fraction, columns=["fraction score>0.5"])
df["Entry"] = gene_list["Entry"]
df["Protein names"] = gene_list["Protein names"]

df.to_csv("IUPred_analysis.csv", index=False)
```

Table A.3 The Python script used for IUPred2A analysis of all the *Pf* 3D7proteins on the database.

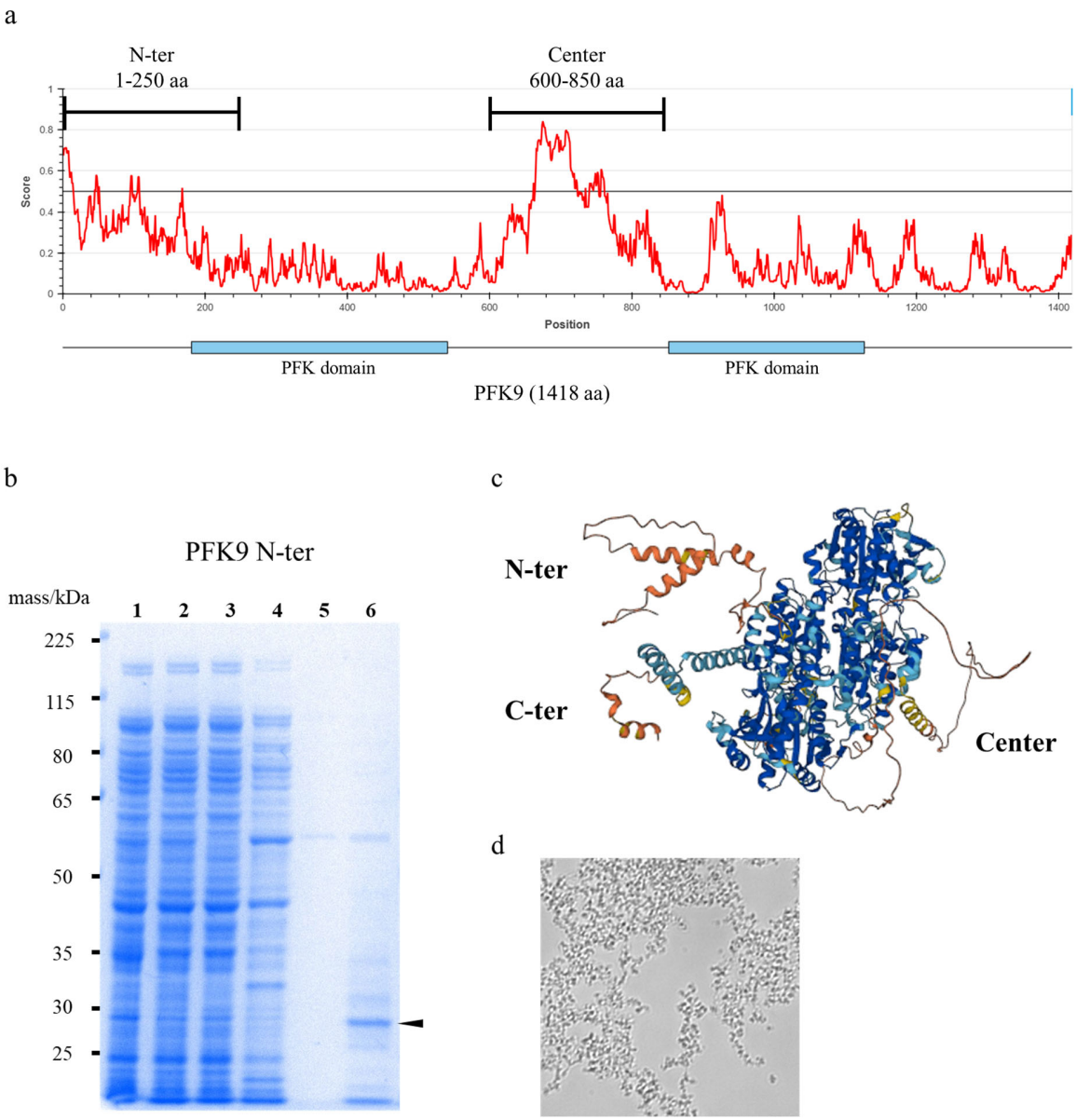

Figure A.1 Purification of PFK9 IDRs. a, The result of PFK9 disordered region prediction with IUPred2A and designs of PFK N-ter and PFK9 Center proteins. **b,** The results of SDS-PAGE for PFK9 N-ter purification. The arrowheads show the purified target proteins. Lane 1: cell lysate, Lane 2: cytosol, Lane 3: flow through, Lane 4: wash with imidazole containing buffer, Lane 5 wash with cleavage buffer, Lane 6: Purified protein after cleavage. **c,** Alphafold2 structure prediction of PFK9. **d,** Representative BF picture of purified PFK9 N-ter protein aggregates.

Gene No.	Gene ID	Name
1	PF3D7_0214300	conserved Plasmodium protein, unknown function
2	PF3D7_1252800	Plasmodium exported protein (PHISTb), unknown function
3	PF3D7_1413200	conserved Plasmodium protein, unknown function
4	PF3D7_1428400	WD and tetratricopeptide repeats protein 1, putative
5	PF3D7_1473300	CKK domain-containing protein, putative

Table A.4 The list of five possible G-body-related genes. The gene IDs and names of the five possible G-body-related genes identified in transcriptome analysis are summarized in the table.

Name	Sequence
PF3D7_1252800_recodonized	TCCCACATTTCGAATAAACTCGAGATGAATTATTCTCTTGTTTGGAAGTATTTGGAGAGAGAGATGAAGAGATACAATAGATCTGTGTGGTGCACCCTTTTA TACGGAAGAAATAACATATTAATTGTTTTAATTTTAAATATTATACTTTGGAACGTGTGTATTACAAATAACGGTATTACTTTGGACAGTAAATACATATCTA CAAGGTACATACGTATTCTTTGCACCCCAGATATTATTGATAACGTGGTAAATGTGAAGATTGAAGAGGAAGAAAACATAAACAAAGAAAATGATAATGTT ATTAAGTCAATTAAGAGTATAAAGTATCCAGACAATGTGAATTTGTACAACGCCCTTAGGAAAAAGATAAGAAAAACATGGAGCAGAACAAATACGGAT TTGTGCCATACTCAAATGAGCATCTTATACCATTCTATAACGAAAAAGACAATAGTATTAACAATGACATAGATTCACTTGATGGTAGAGACAACCTTATTA GGTTAAAAATGTATAATATATGGTTGGAGTTGATGCAAAACGAGCAAATGAAATATTATGGTATAAGACACTCACTTAATAAATTTTACAAAAACCTTAATC AGAAATATAACATAAAGATAGAATCTAATGACAAAGCTCTTAAAGAATGTAACGAGATAATTTGTTTATCAGCTCATTATCTTCAACGTCATCTTAACAACA TGTTCAATGAATGGTTCAAAAAGGGATTCGTGAGTATAGGAGAATTTCAGAACATAATTAACGCAACCAGGCATGGTTGGAAAGTATTAACAACAAACGTG AAGAAGAAGTACAAGGACATATTAACAGACAACTTAATAGAGAAGATGAATAAACCTTATTTTATAGGTGACAATATATTCAACTCATATTTGGACCACAT TAACGTTAAAGACAATACTCAGCAATACAATGAGAATATGAAAAAGATGTCTTGCATTGAAAAGATGCCTATAACTGAAAAGGAAGGTAATATGGAGATG AATTACAATAACAATTTAAATGTTAAGGACAAGAAGTTACTTTACGATAATATAGTTAAAAATAACTCAACCATAAAGAACTATACAGAATGCTTAAAGAT GGCAGAGTATGTGGATGTGGATACCTCTGGTGTGAGAGTAAAAGAAGAAAACAACATGATGAAAAGGAACATTAGAAGGAATAACAATATTTACAAGATT AACAACGAAGAAATATCTAACAACGTGGAAAAGTCTAATAATATAGAAAAAGAGGACAACCAAAATATTAACTATAATGACGGTGAGGAATTAAACGAAA CAGACAAGAACGAAATATACAACAATAATATAGAAAAGGAAGATAACCAAAATATTAATTACAACGATGGAAAGGAGTTAAATGAGACCGATAAGAATGA AATATACAACAACAACATAGAGAAGGGTGATAATCAAAACATAAACTATAATGACGATGAGGAGTTAAATGAGACCGACAAAAACGAATTTTACAACAAT GACGAAGAAAACGAGAACGATGATATAGAAATATCTTTGGAAGACATTTTCGACAAGTCAACTAACATTATTAAGGAGGCAGAAGAAATTATAAATAAGA GGGAGAATGGAACATCAATAGACAGTTGTGTGTTTATTGACAAGCCAGAAGATTATGATAAACAGATTGAATGCATGAATAATAATAGTACAAACGGTTAT CTTGATTACTGTAATAAAAAATTTTGTAATGAGAATAATAGTAACCCTACCTATCTTCAGAGGAAGTGGAAGTCTTTAACACACATTTCTGATAAAGATAAA TCATCAAACAATATAATATCTTCTATTTGGAAATATGTGTCTAACAAGAACAACCTTCTTTACTGGCGTAAGTTTAATACATACGGTACCTACCCATATGATG TACCGGATTACGCAGGTTATCCGTATGACGTTCCGGACTATGCTGGCTCGTATCCATACGATGTACCGGATTACGCGTAACCTGCAGGTCGACTTAATT
PF3D7_1253200_recodonized	TCCCACATTTCGAATAAACTCGAGATGAGTAAGGTGTCTGATAACATTAAGAATGTTGATGACCAGAGAAAGCATTTCGATGAGAAAGAGAAGAAGAAGTT GTTCCTTTACGGTTATGAACAACAATTGTTGTATGGAAGAATTAATTGGAAGTTGGCCGAGAAAAAGAAGATAACTAAACATTCTATTACAACAATGAAAA ATTACTGGAACAATAGTATAGCAAACTGTCTTCCTCAATTTATAGAAAATTACTCACGTGATGTAGAGCGTTTGAATGAGATGAAAAAACAAAATAAAATG AAGAATATAAAAAAGGGAAAGATAAAGAAAAATGACAAAACAAAGAAAACTGCTACTCCAAAAGTACAGTTCACTAAGCAACGTAGTAACATAAGTATGA ACAGAGTGATAAAAGGTGCAAGTTTGGACTACAAGAAGTTATCTACTAACACTTTTCGTAACAAACAGATTGTAGTGAACTCAATTTTGAAGAAAAAGAAA ACAATGAACAAAATTATAGACAAGAAAAATAAGTTAGTGTCATTAAAGACTAAGAATGTTCACTTGAAGAAAGATATACACAAGCCAAATAAGACTAAATT AGTGCAGGGATTGCCTAAGAAAGATAAGAAAAAGGATAATACATATACAACAAAGGGATTACTTAAGGAAGACAACAAAAAGGCCATAAATAAGGGAAA GAAGGAGGATAAAGGTAAGAAGGATGACAAGAAAGACGATAAATTGAAGAATAAAATTAATAAAAAAGATTTGAAGTACGACAACAAATCACAAAAATT AGATAAACACAAGAAAGAAGAAAAGTACGAAAAGTTAAAGACCGATAAGTTTAAAAATGATAAAGGTAAAAACGACAAAGGAGAAGACAAGAACGTAGA CAAAACCAAGAAAGACGCCGACAAGAAGAAAGAAAAAAACGAGGAGAAAATTAAATTAGATGATAAAAATAAAAAGGATAAGATAAAGAAAGACAAAA AGGATGAGAAGAAGGACGAAAAAAAAGATGAAAAGAAAGATGAAAAAAAAGATGAGAAGAAGGATGAAAAAAGGGACGAAAAAAAGGATGAAAAGAG GGACGAAAAAAAAGACGAAAAAAAGGACGAGAAAAAAGGACGAGAAAAAAGACGAAAAAAAGGATGACAAGAAGGATAAAATAAAGAAGGATAAAAAA GAGGATAAGAAGGACAAAAAAAGTGAAAAGAAGGATGATAAGAAGACCAAGAAAAATATAATTAAAAATAGTAAGGGAAAGAAAGGTACCTACCCATAT GATGTACCGGATTACGCAGGTTATCCGTATGACGTTCCGGACTATGCTGGCTCGTATCCATACGATGTACCGGATTACGCGTAACCTGCAGGTCGACTTAATT
PF3D7_1253300_recodonized	TCCCACATTTCGAATAAACTCGAGATGATGCGTAAGAAAAAGAAGGGTCACATTAACGTACACATTAATGACAAGAACACATACGATGAGGGTGAGTTTCT TAATAGAAAAATGGTTGATGGACTTAAGCAGAACGCCTTTTGTCCTTTGAGGAAGAGTATAAACAAGGATATACCTTTTTTTATAAATTACGATATATTGTT AAAGAATTGTAAGCAAGACAAGAACTACTTGGACCTTAATCTTGAAATTAATTATAACTTAGAAGAGATAATGGAAAATAAGGAAAACCTTATGAGGTGTT TACACAGGAAAAACTTAATGGAAGACGAGAAATCATACCAGATGGAAATACCTCACGACAATATGAAGAATAAAAAGTATTACTACGATAACAATATATA CCAAAATAAGAACGATGAGTACGACAACATTTACGAGCAAAGGGACGACATTTATGACCGTAACAATTACTGTAACAATTTCAAGAAAGGTTTCATAAATA TATTGGAACACAAAAAGAACAAGGGTAAAAATATATACGCTGACATTAGTTACTCTGAGGACGAGAGTAGTTATTCTGACAATAATTATTACTCTGGATCA AGTGTGTACAGTTATCAGAAGGATGATAACAAGTCTTTCAACTTCAGTCAAAGAATAACCTACGACACTAACTTATTGGACAAGATTAATATTTATGATAAT ATAACCAATTATATATATAACAACAATAATAACAACAACAATGAAAAAAATAACGAGAAGAACAATGAGAAGAACAACGAGAACAATAACGAAAACAAC AACGAAAAGAACAATGAGAAAAACAATGAAAAAAATAATTGTTACTACAAGAATATGGATAAGCAGAACAAAGATTGTCACAATTATAAAAACGACGTGC CATATATTAATCATCGTAACTACGTTCACAATCAAAATAAATATATAGACGACAAGAATAGGCGTACAGACATTATACAATTTATTAACCACACTGATAAAG ATAATATATCAAATCAGAGGTCTCACACCTCAAATATACAGAACGTAAAACATAACAACCATGAAAAAGGTAAGAGAGAGCACTCTAATTTCTCTGAGTAC ATACAACACAATATGGAAAAGGACTATAGAAGAAACTTAACTGACCGTAGTATAATTCTTAACAACCACATGGAAGAAAACGACTCTCCTTCTATTAATTTA GAATTCTTAAAAAGTTCAAACCCTAGTAATTGCAAGAAGATGGAGAAAGACATATTAAACAAGTACGAAAAGATAATGAAAATTATGAAATACTTGAGGA AAGTGAAGTCAAAATATCCAGAAATAGAGTCTACTGTATCAATTCTTTCTAATCATATAAAAAATGTGACATTCAATTGCGAAAAGATGTTCGAGTCAAGGT ACATGCTTAACGAGTTCCTTAAGAAGCTTTACATATACCAGATATACATTTTAAAAAAAATAGTATTTAACAAGTCTGATATTTTGAAGAACGATGATACCC TTGAGCACTATAATAAACACTTTCATACAACCAAGATGAGGTTCATTTCAAACGATAGGATAAATAATAGTAATGACACTACAATATTTGAAAATATAAAA GAGAACAGTTCATACTCTATGAAGAAGCTTAACGGACAGAAAGAGAACATATTCTCTCACAAAAAATATAACCAAAGGCACAAATCTAAAGAGTATACTAA AGACAAAAAGTATAACGACGTGGGAGTTAATAAAGAGAAATTATCAATACACCAATGAATATATTGGAATGGAAAATAAAAACGATATTAAGAACAAGTAC ATGAATCACCACAATAATAATGTGATACCTTATGATAATAAATGCATGCATATATGGAACGATGATATAAATAAAGAGTCAGAGTACAGTAACCAAATGAA AAATAAGTATAAAGAGAAGTATATTAACAATATTTCTAACTTTGAAGAGATTAATAAACACGAGAATAAGAATAATTTAGAGGATATACACCAGATTAACA AAAACATTTCTAAAGAGAAGAAGGAGATTTCATTGATACAAATGAGAAGAATTTGAGTTATAAGAAGTTATTAATTTCAGAAAACATAGAGACTAACAAT AACAATTGCCATCACAAGAGAGACAAGTCTTTCTCAAAGAACAACTTGAATAATAATTATACCTTTAAGGACAAGTCATTTCTTAACAAAGTGGATAACGTA GAAAACAAAAAACCTTTTAAAAATGAGCCATTAAAAAACGACAAGATATTTTATGATCATATTAAGAAAAAGGACTATTTGAACGTGATTGACGAGAAGAA GAAGGAGGAGAAGAACCCATTGTTGGAACACGAGTTAAACTTGAAAGCCTTAAACTTAGAGTCTAAGGACGAAGCCTTAAAGACTAATATTATAAAAGAG GAGATGCATAAGACATCATACGTGAATAAAAACGGAAATAAAAAGACTCATGTGTTATATAATGACCTTAACAAAGAGTTGTCAGCCATATCAAATAGAGA TAGTGTTATACATGCCTTAAAATACACCCTTTTAAACAAGCCTCAGAATTTTACAACATTACAGAACTTTTTATTTAAAATAGATGTGGAGTTCGTTGAATAT AAAAATTTTGTATTATTAATAACTAAATCTGTGAGGAAATTGCAGCTTGAAGCTCTTTATGGATTAAATGACTTCTCAATATTCGAGAAGGTATACGGAAAA AAGGTTGCCCCTCGTTTTCTTATATCTAAAAAAGTTAAGATGTTTTATAAGTATGATAAATTCTATCAAAAATTTCGTGAATTGGTGAATGTGAGAGAATTCT CTGGTATAACTGACGCCGTAGAATTGATTGGTACCTACCCATATGATGTACCGGATTACGCAGGTTATCCGTATGACGTTCCGGACTATGCTGGCTCGTATCC ATACGATGTACCGGATTACGCGTAACCTGCAGGTCGACTTAATT

Table A.5 Sequences of synthesized DNA for overexpression experiments.

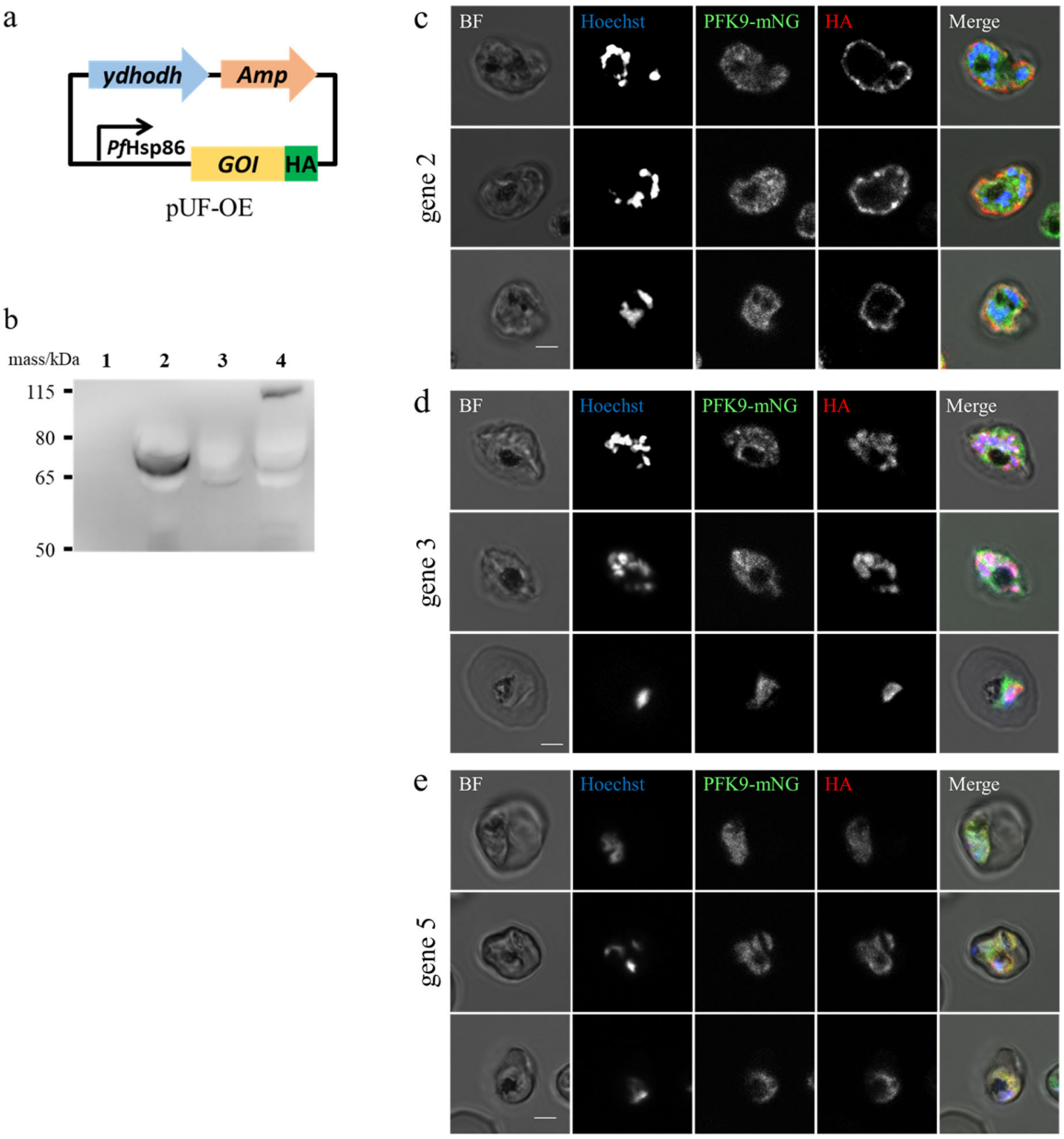

Figure A.2 Overexpression of G-body-related genes in the parasite. a, The gene of interest with 3x HA tag is expressed in the pUF-OE episome with the parasite's regulatory element. **b,** The anti-HA western blotting detected the expression of G-body-related genes. Lane 1: parental line. Lane 2: parental line with gene 2 overexpression (78.3 kDa). Lane 3: parental line with gene 3 overexpression (53.5 kDa). Lane 4: parental line with gene 5 overexpression (117.8 kDa). **c-e,** IFA showed expression of G-body-related genes in the parasite. Cells were fixed and stained with anti-HA antibody. Scale bars represent 2 µm.

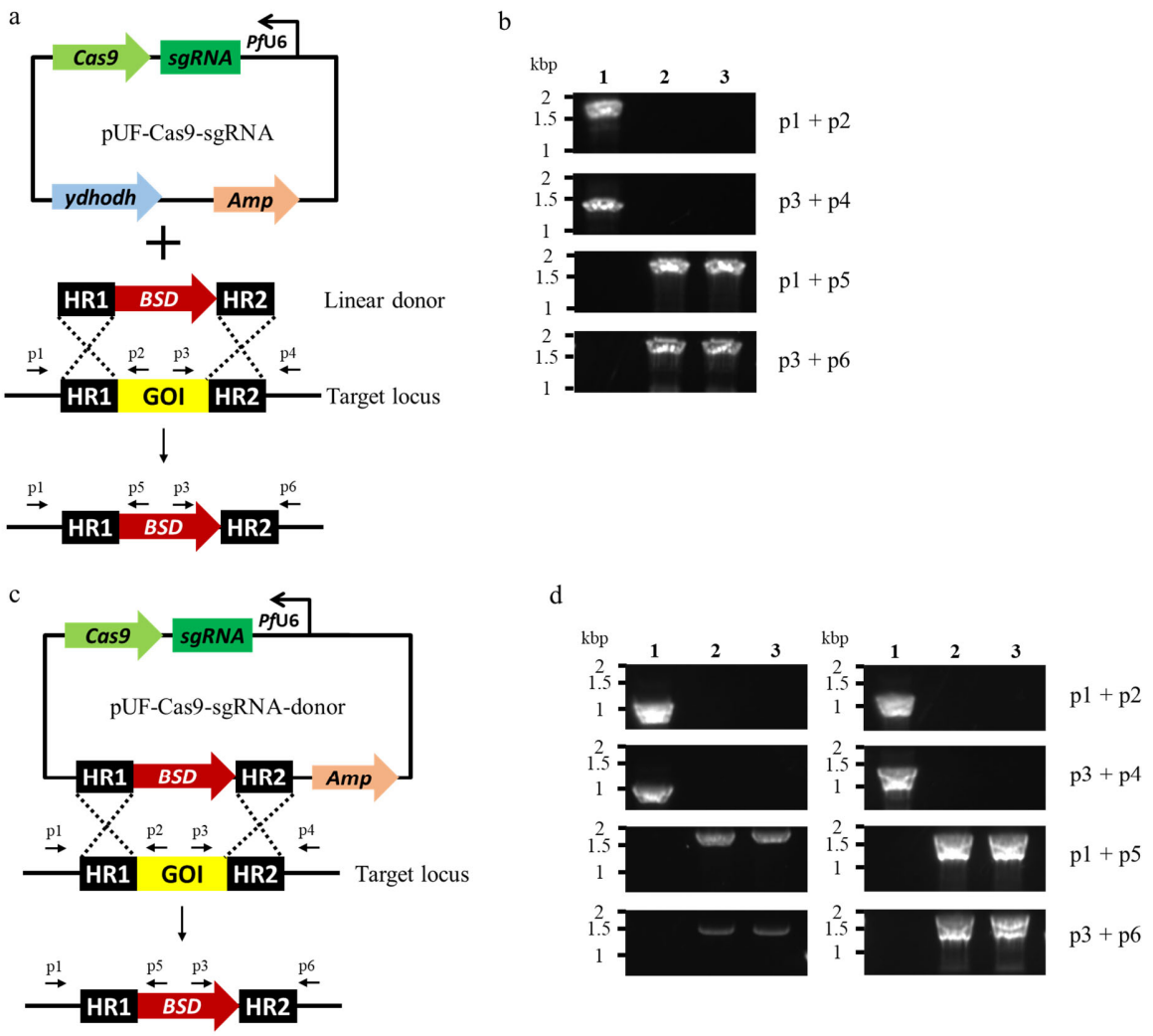

Figure A.3 Knockout of G-body-related genes. a, Cas9 and sgRNA were expressed in the pUF-Cas9-sgRNA episome with the parasite's regulatory element. The linear donor DNA contains homologous regions and BSD expression cassette replaced with the target locus. **b,** Insertion of donor DNA into the parasite genome was confirmed by PCR. Lane 1: parental line. Lane 2: Gene 3 KO clone B3. Lane 3: Gene 3 KO clone D6. **c,** The donor sequence insertion to pUF-Cas9-sgRNA obtained all-in-one plasmid. BSD expression cassette on the plasmid is replaced with the target locus. **d,** Insertion of donor DNA into the parasite genome was confirmed by PCR. Left, Lane 1: parental line. Lane 2: Gene 2 KO clone A8. Lane 3: Gene 2 KO clone F6. Right, Lane 1: parental line. Lane 2: Gene 4 KO clone B8. Lane 3: Gene 4 KO clone C6.

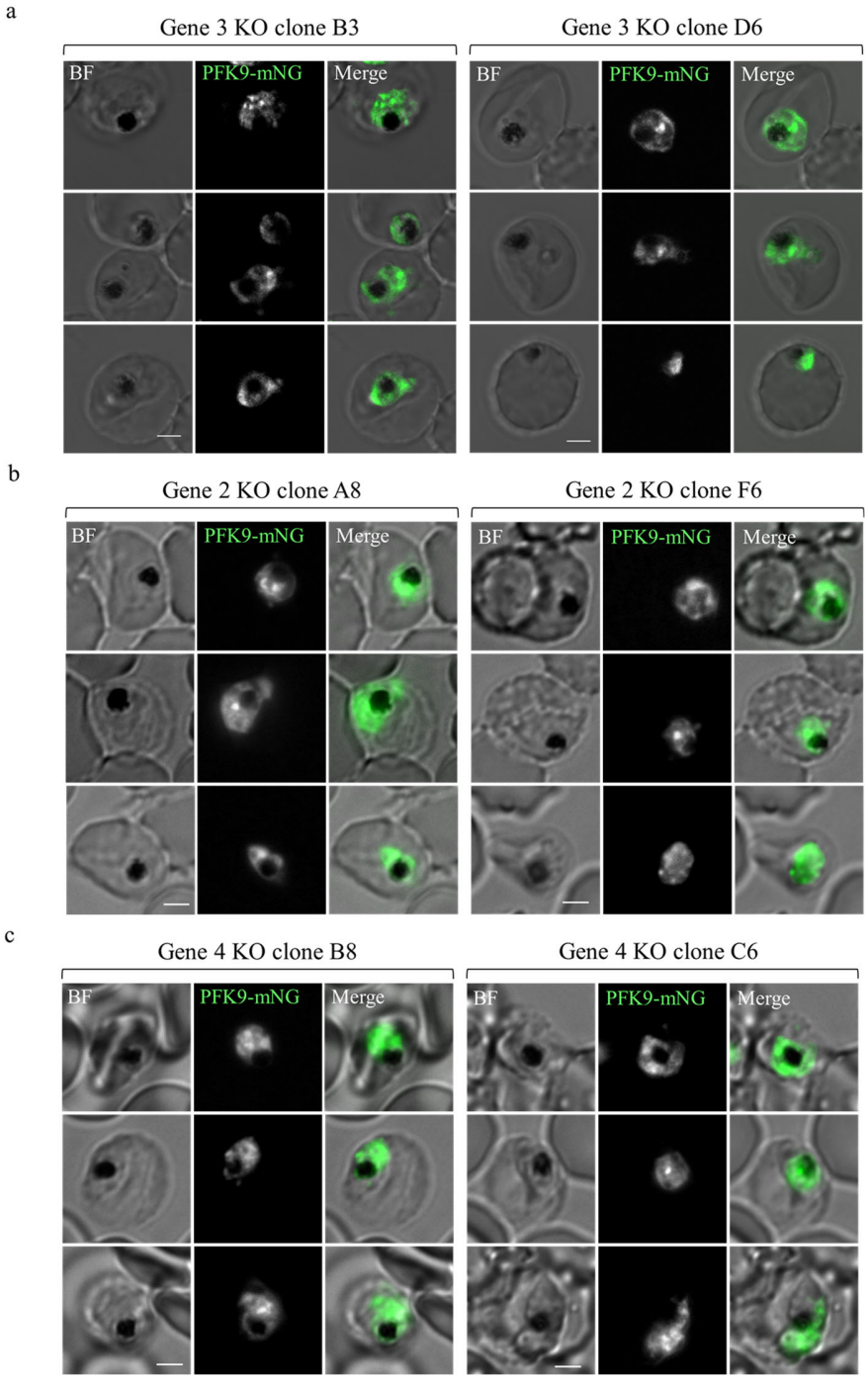

Figure A.4 Knockout of G-body-related genes did not influence the G-body-like structure formation. a, b, c, Live imaging of gene 3, gene 2, and gene 4 knockout clones after 72-hour culture in 5 mM glucose medium. The formations of G-body-like structures were observed in all the strains, suggested these genes were dispensable for PFK9 condensate formation. Scale bars represent 2 µm.